Department of Precision and Microsystems Engineering

Modelling and Design of a 2D Whiffletree Based Large Deforming Hydrostatic Bearing

V. A. van Parijs

Report no : 2020.042
Coach : ir. J. P. A. Nijssen
Professor : dr. ir. R. A. J. van Ostayen
Specialisation : Mechatronic System Design
Type of report : Master of Science Thesis
Date : 19 October 2020

Modeling and Design of a 2D Whiffletree Based Large Deforming Hydrostatic Bearing

by

V. A. van Parijs

to obtain the degree of Master of Science
at the Delft University of Technology,
to be defended publicly on Monday October 19, 2020 at 10:45 AM.

Student number:	4454022	
Project duration:	September 1, 2019 – October 19, 2020	
Thesis committee:	Dr. ir. R. A. J. van Ostayen,	TU Delft
	Ir. J. P. A. Nijssen,	TU Delft, supervisor
	Dr. A. Hunt,	TU Delft

An electronic version of this thesis is available at `http://repository.tudelft.nl/`.

TU Delft

Acknowledgments

The research done during my graduation period would not have been possible without the help of my surroundings. I would also like to extend my deepest gratitude to my parents, Edwin van Zanten and Marjan van Parijs. They have helped me not only through my graduation, but throughout my whole life. They never left my side and always listened to me giving the feedback I needed at the right times.

Many thanks to Jan Groenhuis, Mike de Kuiper and Yannick van Til. Since our final bachelor project, we continued to meet and discuss the different topics of our masters. This helped me a lot in finding the solutions to minor and some great obstacles during my research. The game nights were a very nice attribution for keeping a fresh mind during stressful periods. I am happy to say that the name of our groupchat can now be changed.

Special thanks to Igor Scheepens and Dorus de Boer. Not only during our time at the bachelor of mechanical engineering but also our time on Proteus has been one I would not want to forget. We have been in commissions together, we have played games together, we went on a very nice road trip together and many more. Thanks guys for the continuous support.

I would also like to thank Floor van der Schaft. We have met during our first week in Delft and became close friends for the rest of our study. With the fact that you now study in Eindhoven, we continue to meet and talk about many different subjects. I wish you the best of luck with the final years of your study over there.

Special thanks to Barbara de Groot. You stood by me throughout my masters in hard and easy times and helped me a lot with the graphical images in this research. Thank you.

I would like to express my deepest appreciation to my supervisors Joep Nijssen and Ron van Ostayen. Thank you for the many hours of time you had to meet with me, discuss problems and find solutions for this research. This could not have been finished without your help.

Finally, I would like to thank everyone who has contributed to this research. I can not name all of you, but you know I am thankful.

Vincent van Parijs
Delft, October 2020

Abstract

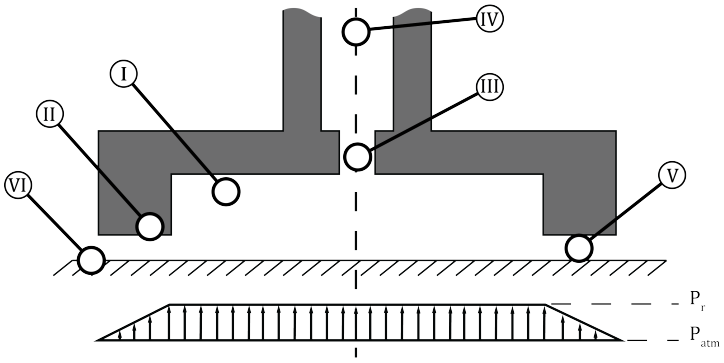

Figure 1: Schematic overview of an hydrostatic thrust bearing. (I) Recess area, (II) Bearing land, (III) Flow restrictor, (IV) Fluid supply, (V) Fluid film gap and (VI) Counter surface (Track)

Hydrostatic bearings, as shown in figure 1, are superior in terms of performance to contact based bearings. They work on the principle of a small film layer between the bearing and the counter surface which is supplied by an external pressure supply. The load capacity of the hydrostatic bearing is dependent on the height of this film layer and the effective surface area of the hydrostatic bearing where a small film layer results in a high load capacity. To maintain high load capacities, the orientation between bearing and counter surface should remain parallel. This results in the need of a deformable hydrostatic bearing when moving over non-constant curvature counter surfaces. Generally, hydrostatic bearing are made very stiff to maintain load bearing capacity. This means that the bearing is not able to deform and maintain a parallel position with the counter surface. This results in a dilemma, a high stiffness is desired to maintain large loading capacities while a low stiffness is required to allow for deformations to maintain a parallel position with the track. Since conventional hydrostatic bearings are made very stiff, they are not considered an option for the use on non-constant curvature counter surfaces, thus limiting the applicational use of hydrostatic bearings.

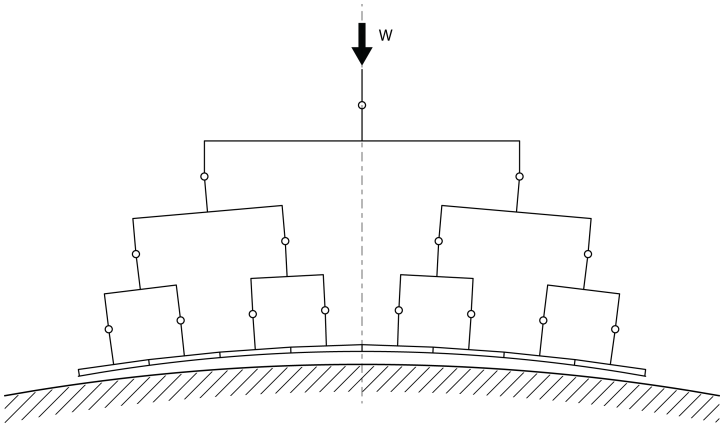

Figure 2: Schematic overview of a whiffletree support system.

The objective of this thesis is to allow deformability for hydrostatic bearings. This is achieved by coupling multiple hydrostatic bearing pads, also called slippers, together with a so-called whiffletree support system as shown in figure 2. The whiffletree allows for rotations of the slippers maintaining a parallel orientation

with the track. Furthermore, the whiffletree allows for smaller slipper lengths where a quadratic relation is found between the slipper length and slipper required compression. Meaning that the decrease in slipper size results in a quadratic decrease of required compression of the slipper and thus the bearing.

The whiffletree support consists of multiple linkages connected by joints. The joints used can not be common contact joints since this would re-introduce the negative properties of wear, friction and stick-slip into the system. Compliant joints could solve these drawbacks, providing the same motion as conventional contact joints without the negative properties. The main requirements for the compliant joints are a high axial stiffness to maintain load bearing capacity while having a low rotational stiffness with a large range of motion to allow for the rotations in the support. Conventional compliant joints do not possess all of these properties [1]. So to design a new joint the range of motion of each joint, the normal and shear forces acting on each joint and the rotational stiffness of each joint is required. In other words, the systems kinematics and kinetostatics should be obtained.

The range of motion is obtained by using a rigid body model of a 2D whiffletree support and finding the corresponding kinematics. The normal forces, shear forces and moments acting on the joints are obtained by decomposing the force acting on each individual slipper and adding the corresponding forces of each slipper acting on each joint. With the forces and moments known, the normal, shear and rotational stiffness is determined of each joint in the system.

Overall, the objective of this thesis has been successfully achieved by the addition of a whiffletree support system. The whiffletree support allows for the slippers to rotate maintaining a parallel position with the track. Furthermore, the slipper length can be decrease without the loss of load capacity which results in a smaller required deformation of each slipper. Thus allowing the hydrostatic bearing to follow non-constant curvature counter surfaces.

Contents

1

Introduction

1.1. Background

Humans are in a continuous pursuit to design and improve machines to exceed the limitations of their human strength. Instead of improving each machine on its own, one could look into a key part that is used in almost every machine. One of these key components are bearings. Bearings are used to constraint a certain motion, while allowing motion in the desired direction. Furthermore, bearings tend to decrease the friction between the moving parts, allowing easier movement of the load in the desired direction. A great example of this principle dates back to the ancient Romans. A ball bearing was found that was used in a rotating table on one of their two Nemi ships [2]. A more recent bearing applications is the use of bearings by Leonardo da Vinci around the year 1500. Drawings where found using ball bearings in his design of a helicopter [3]. As of today, bearings can be found in almost every machine that has moving parts. They can be found in transportation devices, medical equipment, factory robots and many more. The most commonly used bearings are plain, ball or roller bearings. These bearings are subjected to stick slip and wear down after each iteration reducing the lifetime of the bearing. For applications that require high accuracy and precision, stick slip is a huge drawback. So, a different type of bearing is needed that eliminates stick slip while maintaining high load capacities. If a lubricant is allowed in the system, hydrostatic bearings could provide a solution.
Hydrostatic bearings work on the principle of a small fluid layer between bearing and counter surface preventing solid to solid contact. Due to the prevention of solid to solid contact, little to no wear occurs during operation. This increases the lifetime of the bearing significantly. A second advantage of hydrostatic bearings is the fluid layer between the bearing and counter surface. Due to this fluid layer, viscose friction occurs instead of dry friction, which lowers the friction coefficient by approximately two orders of magnitude [4]. Finally, hydrostatic bearings are able to maintain high load capacities making them great to use in applications that are subjected to large forces like lock gates, milling machines and large telescopes [5–7]. Conventional hydrostatic bearings are modelled infinitely stiff to prevent failure under these high loads. This prevents hydrostatic bearings for the use in applications where the bearing is required to deform during operation. In other words, conventional hydrostatic bearings can not be used in applications that have a non-constant curvature counter surface.

1.2. Hydrostatic Bearing

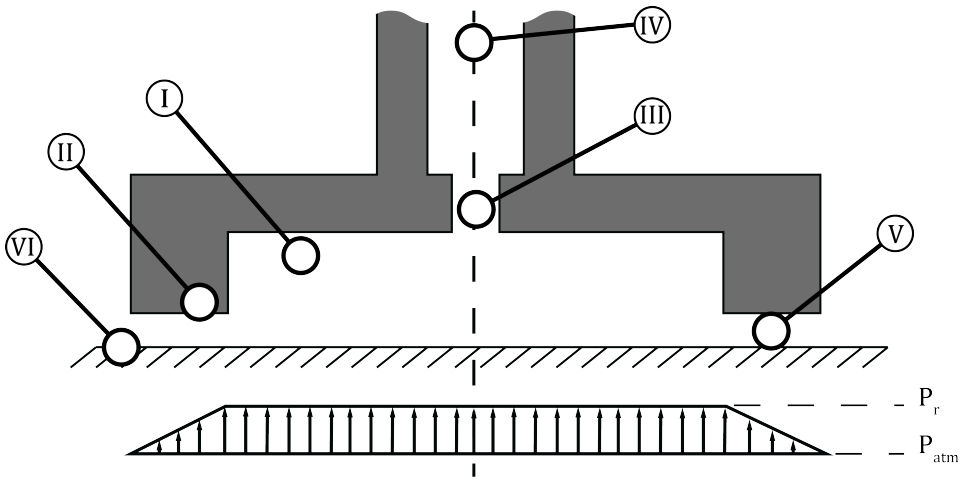

Figure 1.1: Schematic overview of an hydrostatic thrust bearing. (I) Recess area, (II) Bearing land, (III) Flow restrictor, (IV) Fluid supply, (V) Fluid film gap and (VI) Counter surface (Track)

A conventional hydrostatic thrust bearing, figure 1.1, consists of a recess area (I), bearing land (II), flow restrictor (III) and fluid supply (IV). Fluid is pumped from the fluid supply into the recess area to create a uniform pressure profile. The pressure in the recess area is used to lift the bearing from the counter surface (VI) creating small fluid film gaps (V) for the fluid to escape. This creates a small fluid layer between the bearing and counter surface preventing solid to solid contact, also called full film lubrication.

1.3. Problem Definition

To maintain full film lubrication, the bearing and counter surface should remain parallel to each other at all times. For traditional hydrostatic bearings the counter surface must consist of a constant curvature to maintain a parallel orientation between bearing and counter surface. This is required since traditional hydrostatic bearings are modelled infinitely stiff to maintain high load capacity without failure. For a hydrostatic bearing to follow non-constant curvatures, the bearing must be modelled with a definite stiffness to allow for deformations required to maintain a parallel position between bearing and counter surface. The stiffness is reversely proportional to the deformation required. Meaning a larger required deformation results in a lower required stiffness. However, a lower stiffness results in a lower maximum load capacity which is undesired. Therefore, the problem definition of this thesis is stated as followed:

"To design a large deformable hydrostatic bearing able to follow non-constant curvatures."

1.4. Thesis Layout

In this thesis, the model fundamentals of a large deforming hydrostatic bearing are shown in chapter 2. The body of this thesis is build around the paper *"Kinematics of a 2D Whiffletree Based Large Deforming Hydrostatic Bearing"* presented in chapter 3 and can be read as an independent work. The paper gives a design model to obtain the kinematics and kinetostatics of a whiffletree based large deforming hydrostatic bearing where the scripts used in the model are shown in appendix A.4. In chapter 4, a further explanation is given on the moments required to rotate the joints. Chapter 5 provides extra insight on the use of a coupled multi-slipper hydrostatic bearing. Following, the FEM analysis is further explained in chapter 6. In chapter 7 a discussion is given regarding the research in this work. To conclude, a conclusion and recommendations for further research are given in chapter 8 and chapter 9 respectively where some elaboration on further research and the design of a rapid demonstrator is given in appendix B and C respectively.

1.5. State of the Art

To find the state of the art, a look in literature on the subject of deformable hydrostatic bearings is given. Three researches where found that used an elastic support structure to counter for surface waviness or to maintain load capacity.

The Hydro Support: R.A.J. van Ostayen et al. [8][6] introduced a new type of navigation lock-gate support as seen in figure 1.2, the hydro support. The hydro support consists of a hydrostatic bearing that slides over an elastic polymer track and is elastically supported to the lock gate by a rubber hinge to compensate for tilting of the gate lock with respect to the guiding surface.

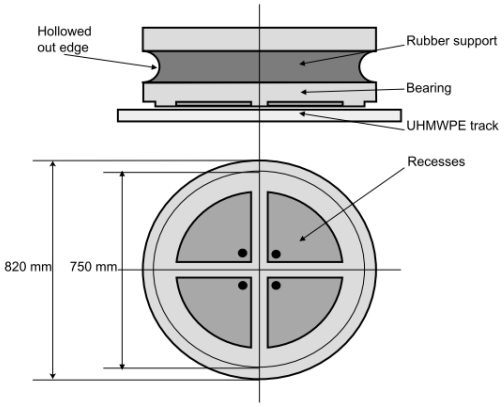

Figure 1.2: Hydrostatic pad with rubber support structure used in the prince Willem-Alexander lock gates. Adopted from [6]

Elastic Support Surface: A. van Beek and L. Lepic [9] introduced an analytical and numerical solution for the calculation of an elastic support surface shown in figure 1.3. The bearing also consists of two rigid plates with a rubber body in between. Calculations show that the bearing surface will converge to a convex surface due to the difference in hydrostatic pressure and pressure of the bearing generated by the mass.

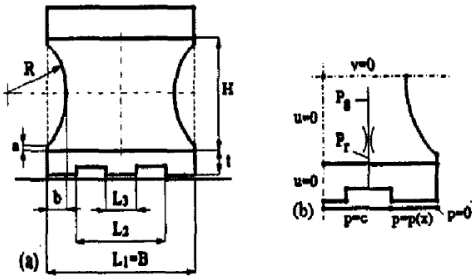

Figure 1.3: Cross section of bearing system (left) and boundary conditions with concentric loading (right). Adopted from [9]

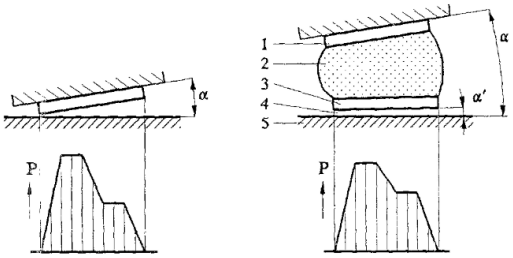

Figure 1.4: Rigid bearing system (left) and elastic bearing support (right). Adopted from [10]

Rubber Supported Hydrostatic Pad: A. van Beek and A. Segal [10] introduced rubber supported hydrostatic thrust bearings with rigid bearing surface. Due to the addition of a rubber body, an elastic bearing support is realized which creates a more parallel hydrostatic film shown in figure 1.4. This increases the pressure distribution under the bearing and therefore results in a higher load capacity.

One can conclude that a gap in literature is found on the subject of large deformable hydrostatic bearings. Furthermore, from the research that has been conducted the conclusion can be drawn that most elasto-hydrostatic research is conducted to compensate tilt instead of to follow non-constant curvatures.

2

Background

To improve the deformability of the hydrostatic bearing, the stiffness of the bearing should decrease. However, a decrease in bearing stiffness could lead to failure of the bearing when it is subjected to high loads. So, it would be beneficial if a high stiffness is maintained and a solution is found to decrease the required deformation. It is expected that the required deformation of the hydrostatic bearing is reduced if the hydrostatic bearing is placed parallel with the counter surface at the center of the hydrostatic bearing. Furthermore, it is expected that the required deformation scales with the length of the hydrostatic bearing. If the scaling is non-linear, a decrease in hydrostatic bearing length could result in a relative larger decrease in required deformation. However, a decrease in hydrostatic bearing length also results in a decrease in load capacity. A solution could be to couple multiple hydrostatic bearings, from now on called slippers, together by the use of a support structure. This will decrease the deformation required of each slipper while maintaining load capacity. To design the new hydrostatic bearing, a look is given in three different sections, the track, the slipper and the support as shown in figure 2.1. The track is defined as the counter surface of the hydrostatic bearing and is used to obtain the required deformation of the hydrostatic bearing. The slipper is used as a bridge between the counter surface and the support and provides the pressure profile and load capacity of the bearing using EHL and the Reynolds equation. The support is used to couple multiple slippers together to maintain load capacity while allowing the slippers to rotate. A rigid body model will be made to find the maximum rotational angles in the joints of the system and their corresponding stiffness's.

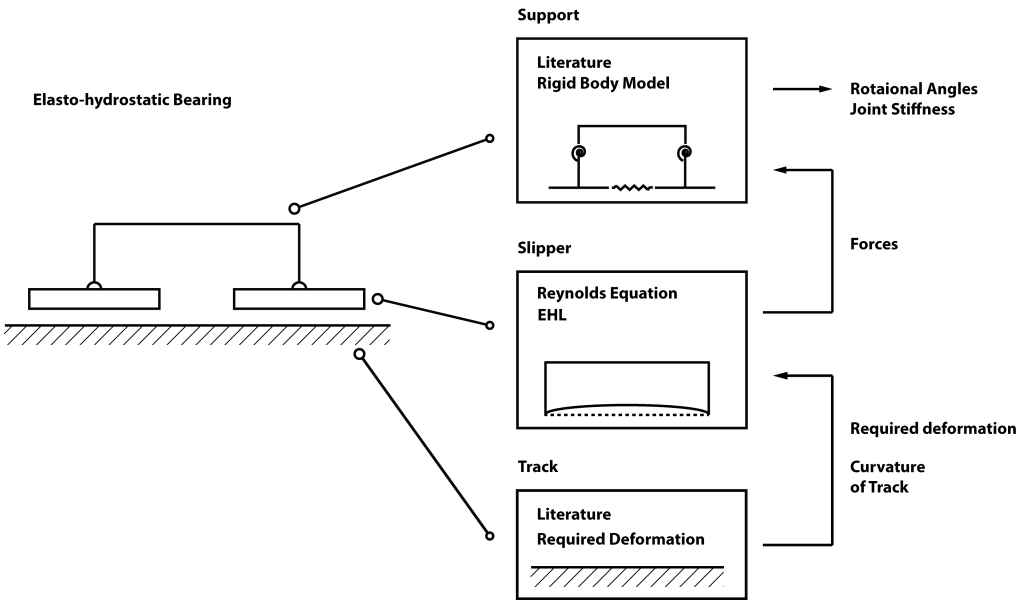

Figure 2.1: Three important sections of the hydrostatic bearing, the track, the slipper and the support.

2.1. Track

The track is defined as the counter surface of the large deforming hydrostatic bearing. In literature, two statements can be found that define large deformable hydrostatic bearings [11]. These are that, large deformable hydrostatic bearings are able to deform to ≥ 10% of the height of the bearing in its undeformed configuration and large deformable hydrostatic bearings are able to deform ≥ 100 times the average film height of the fluid film.

With the definition of a large deforming hydrostatic bearing given, a counter surface needs to be chosen. Since all surfaces are different, a generalized surface is needed to give a good representation of most surfaces. This way, the results obtained for this specific surface are more generalized and could be applied for many different counter surfaces.

2.1.1. Surface

When looking at literature, many surfaces have been modelled as a single or double sine wave [12][13][14][6]. Sine waves have the characteristic of containing all three Gaussian curvatures and could, therefore, represent most surfaces [15]. Furthermore, sine waves are relatively easy to use in mathematical expressions compared to high order polynomials. Therefore, a sine wave is chosen to represent the surface over which the hydrostatic bearing moves. A representation of the surface can be seen in figure 2.2.

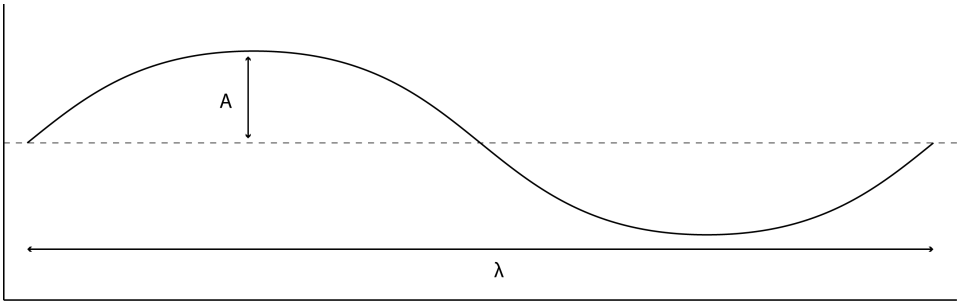

Figure 2.2: Single sine wave used as a model to represent the counter surface (track) with amplitude A and wavelength λ.

2.1.2. Surface decomposition

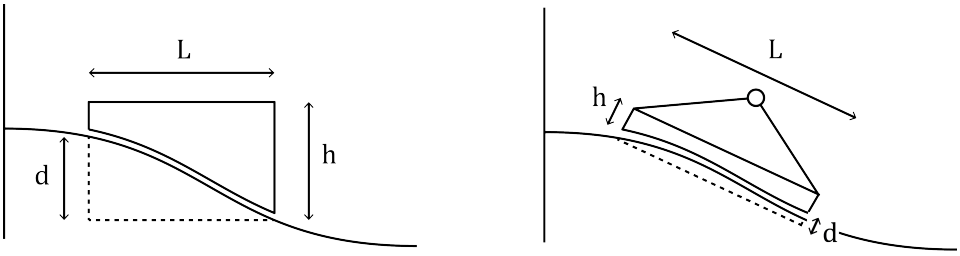

Figure 2.3: Single deforming slipper (left) and single tilted deforming slipper (right). L is the length of the slipper, h is the height of the slipper and d is the maximum axial deformation.

When looking at a sine wave, it is expected that the compression needed for a rectangular shaped object to follow the wave is smaller when the object is placed under an angle (tilted) compared to a horizontal orientation, see figure 2.3. If this is true, the height of the object can decrease if it is allowed to tilt while maintaining equal compression relatively. To validate this expectation a toy model is made shown in figure 2.4. In the figure, a horizontal and tilted line, starting at $y = 2.25$ are plotted against half a sine wave with an amplitude A and wavelength λ of 1m shifted by a quarter wavelength. The average and maximum perpendicular distance from both lines to the sine wave are given in table 2.1.2.

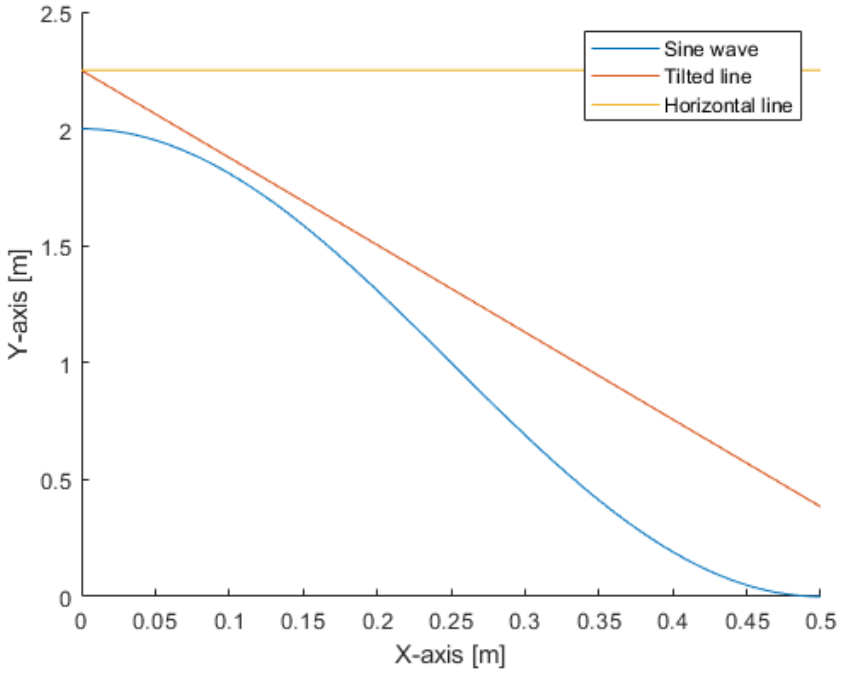

Figure 2.4: Mathematical model result of a tilted (angle at 75 degrees) and horizontal pad and their counter surface.

	Tilted [m]	Horizontal [m]
Average distance	0.0820	1.250
Maximum distance	0.1465	2.250

The results show a large decrease in distance from the line to the sine wave if the line is allowed to tilt. So, it can be concluded that the expectation that the required deformation of the bearing decreases if the bearing is able to rotate is indeed true. Meaning that the deformation required of the slipper can be reduced by adding a joint on the slipper which allows for rotations of the slipper.

2.2. Slipper

The slipper is the bridge between the track and the support structure. It is provided with a certain curvature of the track and a desired flight height and gives a force exerted on the support. The curvature of the track and the Reynolds equation provide the total pressure profile under the slipper. In this section, a small elaboration is given into the Reynolds equations and into the principle of elasto-hydrostatic lubrication. Figure 2.5 gives a small representation of the slipper and shows the mechanics used on each part of the slipper.

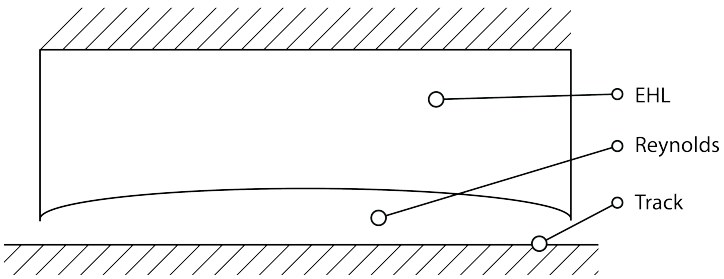

Figure 2.5: Elasto-hydrostatic bearing which is compressed due to a pressure profile generated by the Reynolds equation running over a specific track.

2.2.1. Reynolds Equation

The Reynolds equation is an expression of the conservation of mass in a fluid continuum [16]. The pressure in the fluid film can be described using basic flow equations like the conservation of mass, energy or impulse. The computing power required to solve these equations numerically is very large. So, a variety of assumptions is used to obtain the Reynolds equation to describe the pressure in a fluid film. The Reynolds equations is derived, in this work, with the use of the conservation of mass. The two-dimensional conservation of mass is defined by:

$$\frac{\partial q_x}{\partial x} + \frac{\partial q_y}{\partial y} = 0 \tag{2.1}$$

where (q_x) and (q_y) are the mass flows in, respectively, x and y direction through a medium. With the use of the thin film assumptions, the mass flows can be derived. The five main thin film assumptions are stated as followed:

1. The flow is laminar
2. The flow is stationary
3. The viscosity and density are constant
4. The pressure is constant
5. There are no body forces acting on the fluid

Using all assumptions regarding the Reynolds equation, the mass flow in a film can be defined by:

$$q_x = -\frac{h^3}{12\eta}\frac{\partial p_h}{\partial x} + \frac{\rho(U_a + U_b)h}{2} \qquad q_y = -\frac{h^3}{12\eta}\frac{\partial p_h}{\partial y} + \frac{\rho(U_c + U_d)h}{2} \tag{2.2}$$

where (p_h) is the fluid pressure, (h) the film height, (η) the fluid viscosity, (ρ) the density and (U_a, U_b, U_c and U_d) the surface velocities of the surface in x- and y-direction. Substituting equation (2.2) in equation (2.1) and holding the basic assumptions, the full Reynolds equation is defined by:

$$\frac{\partial}{\partial x}\left(-\frac{h^3}{12\eta}\frac{\partial p_h}{\partial x} + \frac{\rho(U_a + U_b)h}{2}\right) + \frac{\partial}{\partial y}\left(-\frac{h^3}{12\eta}\frac{\partial p_h}{\partial y} + \frac{\rho(U_c + U_d)h}{2}\right) = 0 \tag{2.3}$$

For hydrostatic bearings, it can be assumed that the velocities of the wall remain zero. Applying this in equation (2.3) gives the following equation:

$$\frac{\partial}{\partial x}\left(-\frac{h^3}{12\eta}\frac{\partial p_h}{\partial x}\right) + \frac{\partial}{\partial y}\left(-\frac{h^3}{12\eta}\frac{\partial p_h}{\partial y}\right) = 0 \tag{2.4}$$

To conclude, the Reynolds equation describes the flow between two surfaces by means of pressure, viscosity, velocity and geometry and is valid for both rough and smooth surfaces. Bear in mind that surface roughness could disturb the flow in the fluid film. Nonetheless, the surface roughness is not included in the design of this hydrostatic bearing and the assumption of a smooth surface is made.

2.2.2. Elasto-hydrostatic Lubrication

Elasto-hydrostatic lubrication works on the principle of elasto-hydrodynamic lubrication. Elasto-hydrodynamic lubrication mostly occurs in a rolling motion between two elements. Since the roller and inner race have an opposite curvature, the contact is seen as a point contact. Due to this point contact, a very high-contact pressure occurs which slightly deforms the roller. This deformation is necessary to maintain a continuous hydrodynamic film. When looking at this principle in hydrostatic lubrication, the pressure generated by the pomp in the bearing results in deformation of the bearing. This is, in most cases, not the problem, since most hydrostatic bearings are modelled infinitely stiff and a huge pressure is needed to make a small deformation. However, since the hydrostatic bearing in this research should deform, it is not modelled as infinitely stiff but has a certain stiffness. This means that the hydrostatic bearing can deform due to the pressure generated by the full film lubrication. This deformation has two resulting behaviors. Firstly, due to the deformation of the bearing, the pressure profile will change as shown in figure 2.6.
Since the gradient under the bearing changes, the pressure profile shapes into a parabolic form compared to the triangular form for a hydrostatic bearing with no recess area. This has a profitable effect in increasing the

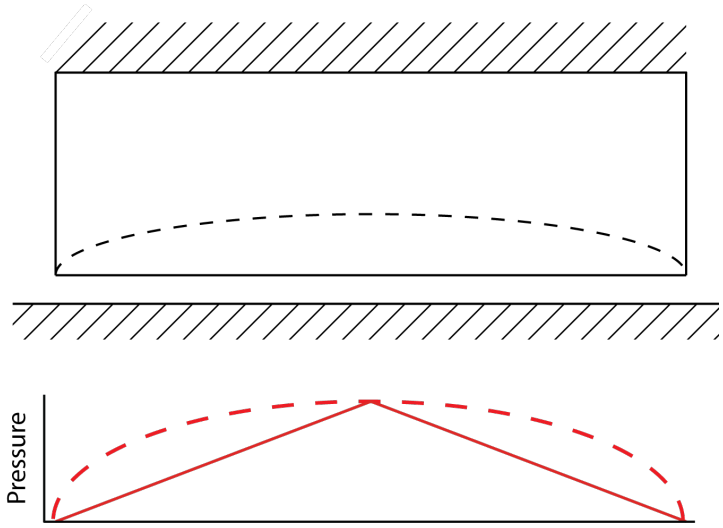

Figure 2.6: Pressure profile change due to the effects of elasto-hydrostatic lubrication.

total pressure under the bearing, and thus the load capacity. This shows a coupling effect between the elasto-hydrostatic lubrication and the Reynolds equation on the slipper. Secondly, due to the change in pressure profile, larger stresses will be present in the bearing which could result to failure of the system. A design approach for such deformable slippers is given in [11].

2.3. Support

The support is one of the key parts of the system. It allows the slippers to rotate to maintain a more profitable position with the gradient of the track reducing the required compression of each slipper as shown in section 2.1.2. Furthermore, load capacity can be maintained by coupling multiple slippers together allowing each slipper to be smaller in length. So, the system needs a suitable support structure that allows the end effector to rotate while being able to transfer the load capacity through the support without any complications.

2.3.1. State of the art

To see which support structure suits this design best, a literature search is conducted on the subject of support structures. The main criteria are: the allowance of rotation in the end effector and the ability to easily transfer the load capacity. In this section, a brief summary of the 5 most promising support systems found in literature is given which is concluded by the choice of the support for this design.

Rocker Bogie: The rocker bogie was developed for NASA in 1988 [17] and has since been NASA's favorite suspension design for rovers [18]. An example of the use of a rocker bogie is the Mars Exploration Rover [19]. The rocker bogie consists of a bogie, which can also be found in trains and crane supports, and a rocker. The rocker is the fundamental part of the rocker bogie and is an additional arm on which the body and a third wheel is connected as shown in figure 2.7. Due to this design, the rocker bogie can stabilize its center of gravity while following a rough surface [20][21].

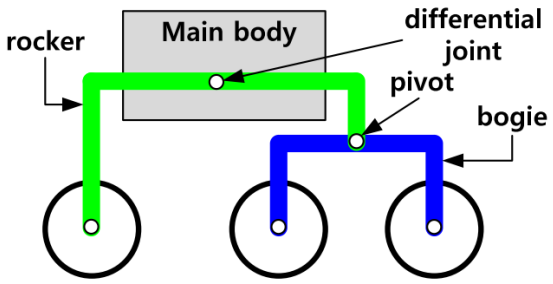

Figure 2.7: Rocker bogie mechanism used as suspension for the Mars Explorer Rover. Adapted from [20]

Zero Potential Energy System: Zero potential energy systems use the theory of zero potential energy to remain stationary in every configuration [22]. Figure 2.8 shows a zero potential energy system. Here cylinders are wrapped in an elastic cord which is pre-stressed. Since the length of the cable remains the same in each orientation of the cylinders, the total potential energy in the system remains the same [23]. The drawback of the system is the requirement of zero friction between the rollers and a fixed external load.

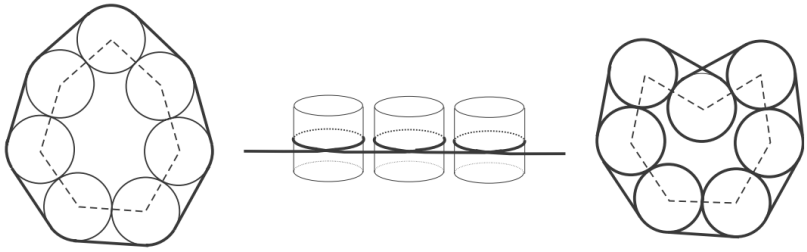

Figure 2.8: Zero potential energy system in 3 configurations. A convex ring wit a stressing cable touching the discs from outside (left), a stressing cable around each coil (middle) and a concave ring with a stressing cable around each coil (right). Adapted from [23]

Parallel Manipulator: Parallel manipulators, shown in figure 2.9, are active systems that compensate for the roughness of the track by actuators and a controller making it an active system [24]. The mechanisms mostly consist of 6 linkages divided in three groups of two which are allowed to rotate and translate up and down. This way, the end effector can be placed in each orientation in the allowable operation box of the system. Some examples of systems that use parallel manipulators are pick and place robots, 3D printers, gangways for ships and many more.

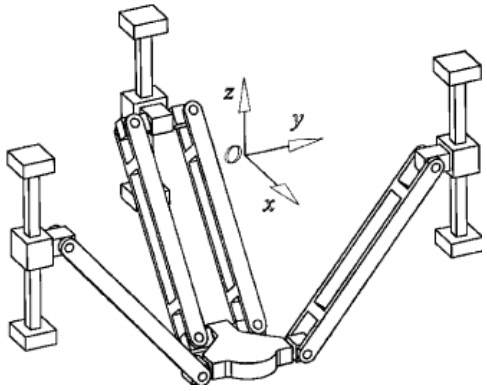

Figure 2.9: Representation fo a parallel manipulator. Adapted from [25]

Body Guidance System: Body guidance synthesis is the task of seeking a mechanism which simultaneously generates a desired path of a fixed point to a link and a desired orientation variation of the link. This is one of the most complicated synthesis available. A good example is the four bar linkage mechanism [26]. However, as explained before, this synthesis is quite complicated and provides a single motion which could limit the applicational use of the system to that single motion.

Whiffletree: The whiffletree, as seen in figure 2.10, has been used for many years in agriculture. It was used to divide the load of a plow between two draught animals using the concept of a lever. The draught animals where attached to the end of the whiffletree beam and the plow was placed in between the draught animals. This shows that the whiffletree can be used as a force distributor. A nice fundamental concept of the whiffletree is that multiple beams can be connected together creating a whole system of whiffletrees to divide the load over multiple end points. Besides the use in agriculture, whiffletree's are also found in windshield wipers, the support of telescopes and other high precision applications. Some examples are a test setup for wind turbine blades [27], the Thirty Meter telescope (TMT) [28] and the E-ELT optical telescope [29] [30].

The whiffletree is a simple solution to provide a force distribution support system in either two- or three-dimensions.

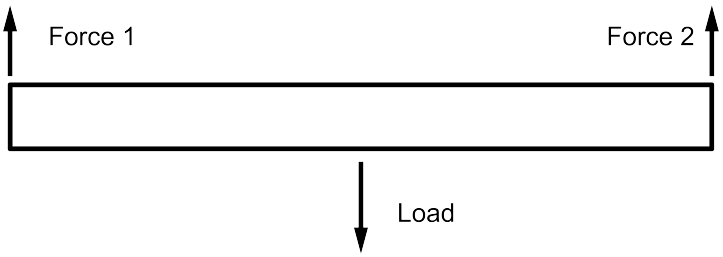

Figure 2.10: Equal distribution of forces by a simple whiffletree system.

2.3.2. Support Selection

As stated before, a suitable support has the ability to rotate the end effector and could easily transfer the load capacity through the system. Furthermore, it is desired if the support system is simplistic in design. Suitable systems could be the rocker bogie, parallel manipulator and the whiffletree. The parallel manipulator is a good choice but has the drawback of being an active system. For this design a passive system is desired to prevent the use of complicated controllers. Thus leaving the choice between the rocker bogie and the whiffletree. In essence, the rocker bogie and whiffletree work on the same fundamental principals. They both work as a force distributing system which allows the end effectors to rotate. The main difference is the deviation in distance between the end effectors during operations. Looking at the rocker bogie, the distance between the end effectors deviates largely during motion. This means that, if the slippers are coupled together by an elastic material, this piece will be subjected to large stresses due to deformations. These large stresses are a critical part in the system and must be reduced to a minimum. Looking at the whiffletree, the change in distance of the end effectors during operation is significantly smaller. Thus the stresses on the coupling parts will be reduced. Therefore, a whiffletree is chosen as a suitable support to connect the slippers together in the hydrostatic bearing.

2.4. Summary

This section provides a summary of chapter 2. The large deforming hydrostatic bearing consists of multiple slippers and joints connected by a whiffletree support system to follow a counter surface as shown in figure 2.2. The whiffletree support is used to reduce the required deformation of each slipper by allowing the slippers to rotate to obtain a parallel orientation with the counter surface. The counter surface is represented by a sine wave with amplitude A and wavelength λ. And can be used to model multiple different counter surfaces. The pressure profile and load capacity of the bearing is obtained by using the principle of EHL and the Reynolds equation. The model is used to find the maximum angular rotation of each joint and their corresponding stiffness's.

3

Paper: Design Considerations for 2D Deforming Hydrostatic Bearings Utilizing Whiffletree Suspensions

Design Considerations for 2D Deforming Hydrostatic Bearings Utilizing Whiffletree Suspensions

Vincent A. van Parijs, Joep P. A. Nijssen, Ron A. J. van Ostayen
Department of Precision and Microsystem Engineering
Delft University of Technology
Delft, The Netherlands
Email: vincent.van.parijs@gmail.com

October 6, 2020

Hydrostatic bearings are superior in terms of performance to contact based bearings, but non-usable in applications with non-constant curvature counter surfaces. A solution to this would be the introduction of deformable hydrostatic bearings components to cope with these required deformations. To reduce the required deformation of a bearing pad, multiple pads are connected through a so-called whiffletree support system. In this work, the design approach for such a whiffletree based hydrostatic bearing system is introduced. The approach includes determining the load capacity of all individual slippers. Design considerations are given regarding the joint rotational-, normal- and shear stiffness of each individual joint.

1 Introduction

Hydrostatic bearings have the properties of obtaining a high load capacity while maintaining low friction. This is due to the small fluid film between bearing and counter surface. Compared to conventional slider and roller bearings in terms of friction, wear and load capacity, hydrostatic bearings remain the preferred option. However, conventional hydrostatic bearings are limited to applications that have an external pressure source and constant or zero curvature counter surfaces [1]. To eliminate the second limitation, compliant hydrostatic bearings could provide a solution. Compliant hydrostatic bearings offer the ability to deform, following the counter surface while maintaining its film height. One approach to design compliant hydrostatic bearings, is to design the support to be elastic. This has been used to counter waviness of the counter surface [2, 3], to maintain load capacity when the bearing is tilted [4] or to function as an elastic pivot [5]. However, these type of supports are limited to small deformations in the order of the bearing film height [2, 6]. This results in an absence of hydrostatic slider bearings used in applications with non-constant curvature counter surfaces. Examples of such potential applications can be found in motors and pumps, in civil structures like lock gates and in sliding rooftops of stadiums [3, 7, 8]. Thus, a wide variety of potential applications could benefit from the improved functionality. This work will focus on the design of a large deforming hydrostatic bearing able to follow a non-constant curvature counter surface. Two statements can be found in [1] that define large deformable hydrostatic bearings. These are as follows: Large deformable hydrostatic bearings are able to deform $\geq 10\%$ of the height of the bearing in its undeformed configuration, and large deformable hydrostatic bearings are able to deform ≥ 100 times the average film height of the fluid film.

For hydrostatic bearings it is fundamental that the bearing and the counter surface remain close to parallel [9]. This means that, for a non-constant curvature counter surface, the bearing needs to deform to maintain a parallel orientation with respect to the counter surface. It is expected that the required deformation of the bearing, in order to maintain a parallel orientation to the counter surface, decreases as the length decreases. This is expected, as the curvature of the counter surface becomes close to linear if the length of the curvature decreases. However, a decrease in bearing length results in a decrease in load capacity which is undesirable. A solution could be to connect multiple smaller bearing pads, also called slipper, together by the use of a support structure [10]. This way, the deformation required from each slipper to maintain a close to parallel orientation with the counter surface, is reduced while load capacity is maintained. A suitable support system is the whiffletree [11]. Examples of applications that use a whiffletree as support are testing setups for wind turbines and telescopes [11–14]. It is important that conventional joints are not used in the support system of the hydrostatic bearing since they would re-introduce wear, friction and backlash into the system. Compliant joints could solve these drawbacks, providing the same motion as conventional contact joints without the negative properties, in general at the cost of load bearing capacity [15]. The main requirements for the compliant joints are a high axial stiffness to maintain load capacity while having a low rotation stiffness with a large range of motion to allow for the rota-

tions in the support and decrease the tilt of each individual slipper. Conventional compliant joints do not possess all of these properties. They generally have either a high normal stiffness with a high rotation stiffness or a low rotation stiffness with a low normal stiffness [16]. So, a new type of compliant joint is required which possess these properties. To design such joints and systems, knowledge is needed about the kinematics and kinetostatics of the system.

In this paper, a general method to obtain the kinematics and kinetostatics of a 2D whiffletree based large deformable hydrostatic bearing system are provided. First, the relation between the required slipper compression and slipper length is determined. Following, a model is presented to determine the footprint of the bearing system. Then, rigid body mechanics are used to determine the kinematics, used to determine the angular rotation of the individual joints. Next, design steps are provided to determine load capacity and pressure profiles of such whiffletree based bearing systems. Finally, an elaboration on the joint normal-, rotational- and shear stiffness desired for such systems is provided. It should be noted that certain aspects regarding the kinematics and kinetostatics of a 2D whiffletree based large deformable hydrostatic bearing system can be modelled in different ways. The models provided in this work are used to give a general solution while other modelling approaches could be used to find more detailed results.

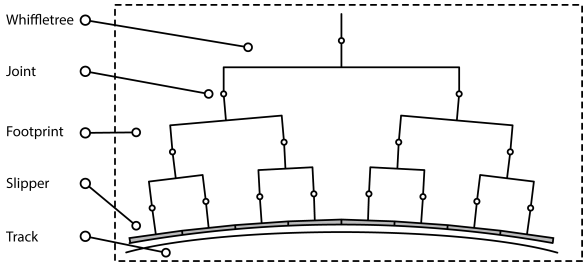

Figure 1: Schematic overview of the whiffletree based large deforming hydrostatic bearing.

2 Methods

The 2D whiffletree based large deforming hydrostatic bearing consists of multiple hydrostatic slippers connected by a whiffletree support system where the whiffletree is made of multiple rigid linkages connected by joints as shown in Fig 1. The whiffletree support is used to reduce the required slipper deformation by allowing each slipper to rotate to obtain a better orientation with the counter surface. In this work, the counter surface or track of the system will be represented by a sine wave with wavelength λ and amplitude A [3, 17–19]. The focus of this section is to obtain the kinematics and kinetostatics of such a whiffletree support system.

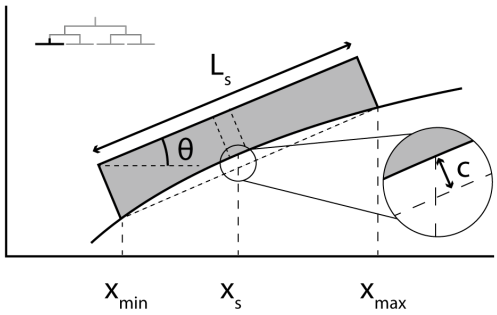

Figure 2: Single slipper compressed to remain parallel to the track with the corresponding parameters.

2.1 Bearing Topology

2.1.1 Bearing Deformation

The bearing deformation, as function of its length, can be expressed as the slipper compression required to maintain a parallel orientation with the track. Figure 2 shows a slipper in its deformed configuration while maintaining a parallel position with the gradient of the track. To obtain the slipper compression, the minimum and maximum y positions of the part of the track under the slipper, further called specific track section, in the slippers reference frame, are required. The specific track section is obtained by finding the x position of each edge of the slipper $x_{\min/\max}$ described by:

$$x_{\min/\max} = x_s \pm \frac{1}{2} L_s \cos(\theta) \tag{1}$$

where x_s is the x position of the slipper center, L_s is the slipper length and θ is the angle of the slipper center point with respect to the horizontal. The specific track section U is now defined by:

$$U = \begin{bmatrix} x \\ y \end{bmatrix} = \begin{bmatrix} x \\ A\sin(\frac{2\pi x}{\lambda}) \end{bmatrix} \text{ for } x_{\min} \leq x \leq x_{\max} \tag{2}$$

where A is the amplitude of the track and λ is the wavelength of the track. The specific track section is placed at the origin defined by:

$$U_{\text{translated}} = U - T \tag{3}$$

where T is the translation matrix defined by:

$$T = \begin{bmatrix} x_s \\ A\sin(\frac{2\pi x_s}{\lambda}) \end{bmatrix} \tag{4}$$

Following, the specific track section is rotated such that the gradient of the track at position x_s is orientated parallel to the horizontal defined by:

$$U_{\text{final}} = R \cdot U_{\text{translated}} = \begin{bmatrix} x' \\ y' \end{bmatrix} \tag{5}$$

where R is the rotation matrix described by:

$$R = \begin{bmatrix} cos(\theta) & sin(\theta) \\ -sin(\theta) & cos(\theta) \end{bmatrix} \tag{6}$$

Finally, the compression c of the slipper to remain parallel with its track is described by:

$$c = y'_{\max} - y'_{\min} \tag{7}$$

where $y'_{\min}$ and $y'_{\max}$ are respectively the minimum and maximum y values of the rotated specific track section. The slippers maximum required compression over the whole track is obtained by following the previous steps for each x_s position on the track. Figure 3 shows the maximum compression required as a function of the slipper length for a track amplitude of 5%, 10% and 15% of the wavelength respectively. It can be seen that the relation between the compression and slipper length is approximately quadratic. This means that a decrease in slipper length of factor s will result in a decrease in compression of factor s^2.

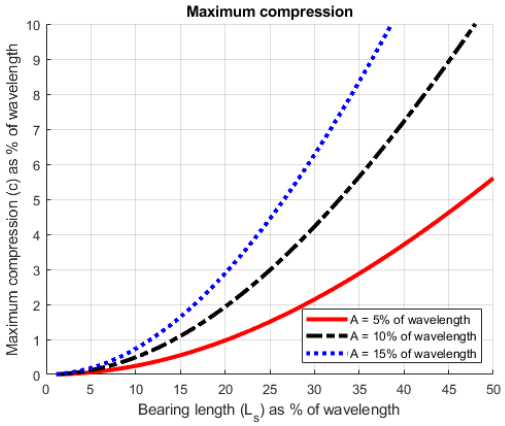

Figure 3: Compression required of a single slipper, as function of the slipper length for a counter track with an amplitude of 5%, 10% and 15% of the wavelength respectively.

2.1.2 Bearing Footprint

With the compression as function of the slipper length defined, the total footprint of the bearing is obtained. The total footprint of the bearing consists of the bearing height and length. The bearing height is built up out of the slipper height and the total joint height in the system as shown in Fig. 4. Assuming that the height of the joint on the slipper is equal to half the slipper length and assuming that the height of each joint in a layer is twice the length of the joint one layer below, the length of each joint L_j is defined by:

$$L_j = \frac{2^{n-k+1}}{2} L_s \tag{8}$$

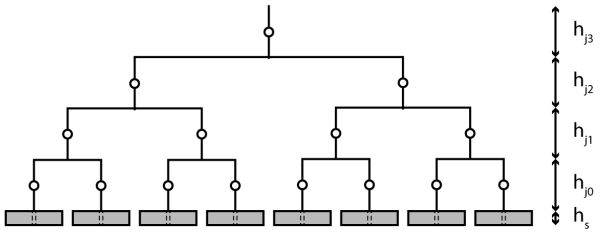

Figure 4: Total baring height of a triple layer whiffletree consisting of the slipper height and the joint height of each individual layer.

where L_s is the slipper length and k is the layer in which the joint is located counted from top to bottom, n being the total number of whiffletree layers and k being $n+1$ for the layer containing the slippers. The total height of the joints h_{jtotal} is defined by:

$$h_{jtotal} = \sum_{k=0}^{k} u L_{j(k)} \tag{9}$$

where n is the number of layers in the whiffletree and u is the joint height to length ratio. The total slipper height is dependent on the maximum allowed compression. The total slipper height h_s is defined by:

$$h_s = \frac{1}{e} c_{\max} \tag{10}$$

where $c_{\max}$ is the maximum required compression and e is the maximum allowable compression of the slippers material. The total height of the bearing h_b is defined by:

$$h_b = h_s + h_{jtotal} \tag{11}$$

Substituting Eqn. (9) and (10) in (11) results in the total bearing height defined by:

$$h_b = \frac{1}{e} c_{\max} + \sum_{k=0}^{n} u L_{j(k)} \tag{12}$$

2.2 Bearing Kinematics

A whiffletree based support fundamentally consists of multiple layers. Each layer contains a number of cells, equal to the layer number where the layer number is shown in Fig. 5a. Each cell, except for the bottom layer, has 3 joints connected by a rigid link as shown in Fig. 5b. The cells of the lowest layer consist of a slipper connected with a rigid link to a joint which is shown in Fig. 5c. In this paper, the indexation is used as shown in Fig. 5a. As shown, parts in the top

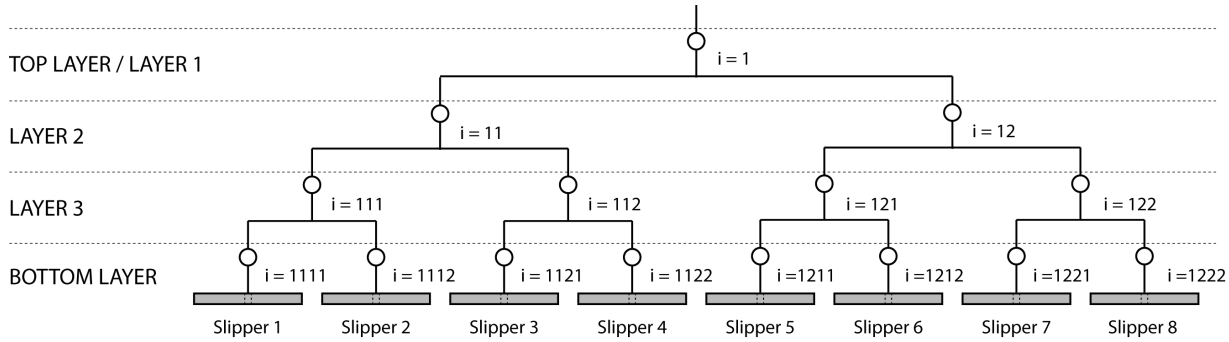

(a) Layout of a triple layer whiffletree support system with the corresponding layer and joint numbers.

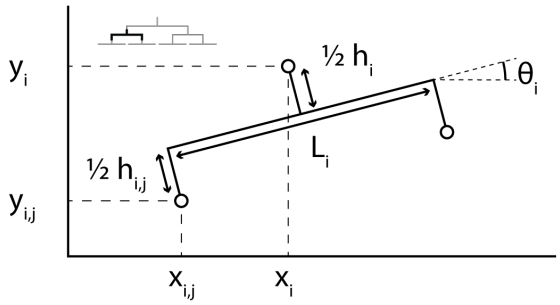

(b) Whiffletree layer cell configuration consisting of 3 joints connected by a rigid linkage.

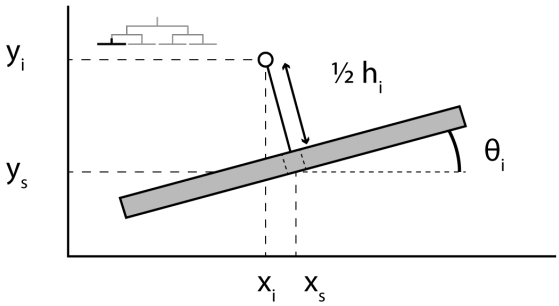

(c) Bottom layer cell configuration consisting of a slipper connected to a single joint by a rigid linkage.

Figure 5: Layout of a 2D whiffletree support system.

layer of the cell are noted with an i, and parts in the bottom layer of the cell are noted with $(i,1)$ for the left part and $(i,2)$ for the right part or (i,j) if both parts are defined. The whiffletree kinematics are described by the linkage dimensions, the joint angles with respect to the horizontal and the joints x and y positions. In this work, all angles with respect to the horizontal are described by θ and all pivot angles of the joints are described by ϕ as shown in Fig. 6. The x and y position of each joint $x_{i,j}$ and $y_{i,j}$, as shown in Fig. 5b, are defined by:

$$x_{i,j} = x_i \pm \frac{1}{2} L_i \cos(\theta_i) + \frac{1}{2}(h_i + h_{i,j}) \sin(\theta_i) \tag{13}$$

$$y_{i,j} = y_i \pm \frac{1}{2} L_i \sin(\theta_i) - \frac{1}{2}(h_i + h_{i,j}) \cos(\theta_i) \tag{14}$$

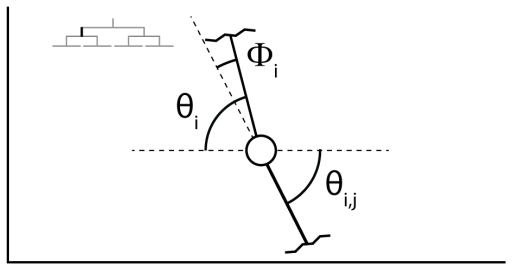

Figure 6: The angle of each linkage with the horizontal θ and the angle with respect to the linkage one layer above ϕ.

where L_i is the length of the linkage, h_i and $h_{i,j}$ are the joint heights, θ_i is the joint angle and x_i and y_i are the respective joint x and y position, one layer above. As seen in Eqn. (13) and (14), the position of each joint in a layer is described by the joints position in the ascending layer. The x and y position of the joint connected to a slipper x_i and y_i, as shown in Fig. 5c, are defined by:

$$x_i = x_s - \frac{1}{2} h_i \sin(\theta_i) \tag{15}$$

$$y_i = y_s + \frac{1}{2} h_i \cos(\theta_i) \tag{16}$$

where x_s and y_s are respectively the x and y position of the center of the slipper, h_i is the joint height and θ_i is the joint angle. This gives the x and y position of the slipper as function of the slipper angle with respect to the horizontal. Assuming that the slipper remains parallel with the gradient of the track at position x_s, the angle θ_i is defined by:

$$\theta_i = \arctan\left(2\pi A \cos(2\pi x_s)\right) \tag{17}$$

where A is the amplitude of the track. Furthermore, the y position of the center of the slipper is described by:

$$y_s = A \sin(2\pi x_s) \tag{18}$$

When setting Eqn. (17) and (18) equal to zero, so that they can be solved, the following set of equations is obtained:

$$\arctan\left(2\pi A\cos(2\pi x_\mathrm{s})\right)-\theta_\mathrm{m}=0 \tag{19}$$
$$A\sin(2\pi x_\mathrm{s})-y_\mathrm{s}=0 \tag{20}$$

If the joint in the top layer is assumed to have a prescribed x position and a variable y position, the set of equations consisting of Eqn. (19) and (20) can be obtained for each slipper. If the assumption holds that the slippers remain parallel with the gradient of the track, the system is fully constrained following Greubler's Equation resulting in a solvable system of equations [20]. If the system of equations is solved, the pivot angle ϕ of each individual joint is then defined by:

$$\phi_{i,j}=\theta_{i,j}-\theta_i \tag{21}$$

where $\theta_{\mathrm{i,j}}$ is the corresponding joint angle with respect to the vertical and θ_i is the joint angle with respect to the vertical one layer above.

2.3 Bearing Kinetostatics

With the bearing topology and kinematics known, the bearing kinetostatics are obtained in terms of load capacity and joint stiffness. In this section, the load capacity is obtained by the pressure profile under each slipper. Furthermore, the rotational, normal and shear stiffness of each joint is defined.

2.3.1 Load Capacity

The load capacity of the bearing is defined by the pressure profile and surface area under the slipper. For a single inlet slipper without a recess area and equal film height, the pressure profile, used in this work, is shown in Fig. 7a. Note that different types of pressure profiles can be used depending on the type of hydrostatic bearing pad. The pressure profile comprises a triangular shape with its peak in line with the inlet of the slipper. The load capacity of a bearing consisting of a single slipper and that of a bearing consisting of multiple slippers with the same total length and inlet pressure are equal. The pressure profile under a slipper is directly related to the flow of the lubricant film under the slipper. The flow Q in any part of the lubricant film is defined by:

$$Q=\int q_x \mathrm{d}x \tag{22}$$

where q_x is the volumetric flux given by the Reynolds equation defined by:

$$q_x=-\frac{h^3}{12\eta}\frac{\mathrm{d}P}{\mathrm{d}x} \tag{23}$$

where h is the film height, $\frac{\mathrm{d}P}{\mathrm{d}x}$ is the gradient in x-direction of the pressure distribution and η is the fluids dynamic viscosity. If an incompressible fluid is used, the volumetric flow

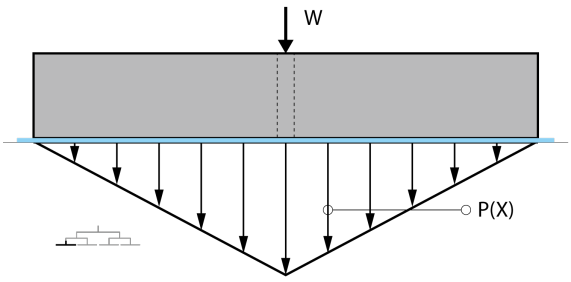

(a) Slipper with a single inlet and its corresponding pressure profile.

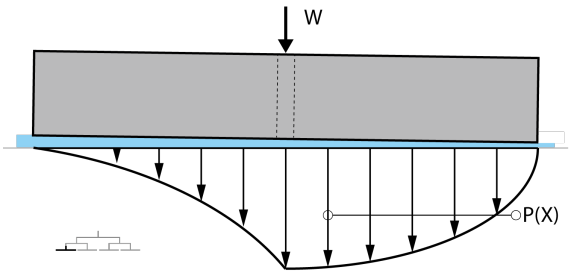

(b) Tilted slipper with a single inlet and its corresponding pressure profile.

Figure 7: Single slipper hydrostatic bearing with their corresponding pressure profiles.

in any point of the lubricant film is constant. The total flow under the slipper must be equal to the flow through the inlet Q_s and is defined by:

$$Q_\mathrm{s}=Q_\mathrm{R}-Q_\mathrm{L} \tag{24}$$

where Q_R and Q_L are the flows through the right and left section of the slipper respectively. The flow of the inlet is determined by a linear restrictor and is defined by:

$$Q_\mathrm{s}=G_\mathrm{s}(P_\mathrm{s}-P_\mathrm{r}) \tag{25}$$

where G_s is the hydraulic resistance of the restrictor, P_s the supply pressure and P_r the pressure under the bearing at the inlet. Note that this is the definition of a linear restrictor while other restrictors can also be used. In this work, the linear capillary restrictor is used and defined by:

$$G_\mathrm{s}=\frac{\pi d_\mathrm{r}^4}{128\eta l_\mathrm{r}} \tag{26}$$

where d_r is the restrictor diameter, η the dynamic viscosity of the fluid and l_r the restrictor length. The load capacity per unit length W of each slipper is then defined by:

$$W=\int P dx \tag{27}$$

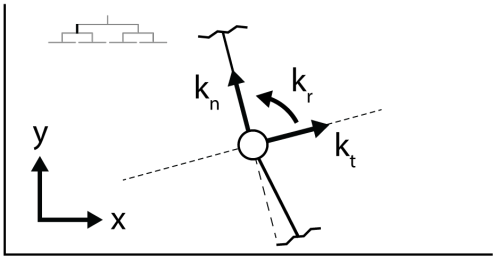

Figure 8: Normal-, shear- and rotational stiffness acting on each individual joint in the whiffletree.

where P is the pressure profile. Finally, the total load capacity of the bearing W_{tot} is obtained by taking the sum of the load capacity of each slipper defined by:

$$W_{\text{tot}} = \sum_{k=1}^{n} W_k \tag{28}$$

where n is the total number of slippers in the system.

If the slipper is placed under an angle, the pressure profile from Fig. 7a changes into an asymmetrical shape as shown in Fig. 7b. This means that a deviation in load capacity under the left and right side of the slipper occurs, creating a moment acting on the slipper. This moment is defined by:

$$M = \int xPdx \tag{29}$$

2.3.2 Joint Stiffness

The performance of the bearing is directly related to the stiffness of each individual joint. The requirements of the joints are a high normal- and shear stiffness to maintain load bearing capacity while having a low rotational stiffness to allow for the rotations in the system. The directions of the rotational-, normal- and shear stiffness of each joint are shown in Fig. 8. The rotational stiffness of the joint k_{r} is defined by:

$$k_{\text{r}} = \frac{M}{\phi} \tag{30}$$

where M is the moment acting on the joint and ϕ is the pivot angle of the joint. The normal stiffness of the joint k_{n} is defined by:

$$k_{\text{n}} = \frac{F_{\text{n}}}{\delta_{\text{n}}} \tag{31}$$

where F_{n} is the normal component of the force acting on the joint and δ_{n} is the normal displacement of the joint. Finally, the shear stiffness of the joint k_{t} is defined by:

$$k_{\text{t}} = \frac{F_{\text{t}}}{\delta_{\text{t}}} \tag{32}$$

where F_{t} is the tangential component of the force acting on the joint and δ_{t} is the tangential displacement of the joint.

As shown, the stiffness is dependent on the moments and forces acting on each joint. The forces acting on each slipper are decomposed to correspond to the fixed x and y frame connected to the upper section of the whiffletree. The forces in x and y direction acting on each slipper F_{x} and F_{y} are defined by:

$$F_{\text{x}} = -W\sin(\theta) \tag{33}$$
$$F_{\text{y}} = W\cos(\theta) \tag{34}$$

where W is the load capacity of the slipper and θ is the angle of the slipper with respect to the horizontal. The forces acting on each joint $F_{\text{x}(i)}$ and $F_{\text{y}(i)}$ are then defined by:

$$F_{\text{x}(i)} = F_{\text{x}(i,1)} + F_{\text{x}(i,2)} \tag{35}$$
$$F_{\text{y}(i)} = F_{\text{y}(i,1)} + F_{\text{y}(i,2)} \tag{36}$$

To obtain the normal- and shear force acting on each joint, a second decomposition is used. The normal force F_{n} acting on each joint is defined by:

$$F_{\text{n}} = F_{\text{y}}\cos(\theta) - F_{\text{x}}\sin(\theta) \tag{37}$$

where θ is the angle of the joint with respect to the horizontal. The shear force F_{t} acting on each joint is defined by:

$$F_{\text{t}} = F_{\text{y}}\sin(\theta) + F_{\text{x}}\cos(\theta) \tag{38}$$

The moment M_i acting on each joint, except for the joints connected to a slipper, is defined by:

$$M_i = F_{\text{a}(i)}\frac{L_i}{2} + F_{\text{b}(i)}\frac{(h_i + h_{i,j})}{2} + M_{i,1} + M_{i,2} \tag{39}$$

where h_i and $h_{i,j}$ are the joint heights and L_i is the linkage length as shown in Fig. 5b and $F_{\text{a}(i)}$ and $F_{\text{b}(i)}$ are defined by:

$$F_{\text{a}(i)} = F_{\text{y}(i,1)}\cos(\theta_i) - F_{\text{x}(i,2)}\sin(\theta_i) \tag{40}$$
$$F_{\text{b}(i)} = F_{\text{y}(i,1)}\sin(\theta_i) - F_{\text{x}(i,2)}\cos(\theta_i) \tag{41}$$

where θ_i is the angle of the joint with the horizontal. The moment acting on the joints connected to the slipper is defined by Eqn. (29). The rotational stiffness of each individual joint can now be obtained. Furthermore, the normal- and shear stiffness of each individual joint is given as a function of the maximum allowable displacement in the normal and tangential direction.

With the rotational stiffness of each individual joint known, the relation between the tilt stiffness of each slipper and their corresponding bottom layer joint is found. The

tilt stiffness of the slipper k_{rs} is defined by:

$$k_{rs} = \frac{M_s}{\phi_s} \tag{42}$$

where M_s is the moment acting on the slipper and θ_s is the slipper angle with respect to the gradient of the track at position x_s. The tilt stiffness of the slipper is modelled as a hinge joint between the slipper and the bottom layer joint as seen in Fig. 9. The maximum tilt stiffness of the slipper is related to the maximum pivot angle of the slipper ϕ_{smax} which is defined by:

$$\phi_{smax} = \arcsin(\frac{2h_{max}}{L_s}) \tag{43}$$

where h_{max} is the maximum allowable deviation in the film height and L_s is the slipper length. The maximum allowable angle of the slipper prevents solid to solid contact between the slipper and track due to tilting of the slipper. However, it is desired that the influence of the tilt stiffness of the slipper into the system is negligibly small. Meaning the hinge joint between the slipper and bottom layer joint in Fig. 9 can be seen as a rigid connection. To assure this, a high tilt stiffness of the slipper is required with respect to the rotational stiffness of the bottom layer joint. This relation is dependent on the angle of the slipper and the angle of the bottom layer joint which is defined by:

$$k_{rs} = \frac{k_{rj}\phi_j}{\phi_s} \tag{44}$$

where ϕ_j is the bottom layer joint pivot angle and k_{rj} is the bottom layer joint rotational stiffness.

To position the whiffletree in each configuration required to follow the track, a difference in load capacity on each slipper is required. The difference in load capacity on the slippers generates a moment acting on each joint, resulting in a rotation of the joint. The difference in load capacity is obtained by changing the film height under each slipper.

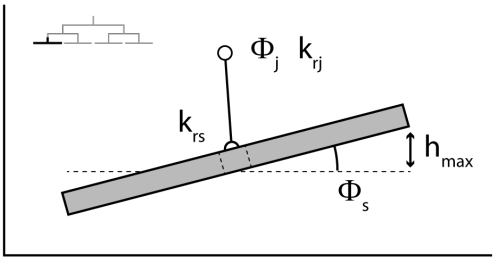

Figure 9: Representation of a slipper with a hinge joint connecting the slipper and bottom layer joint together and the corresponding parameters.

The relation between the load capacity and film height can be found with Eqn. (23) and is defined by:

$$W \propto \frac{1}{h^3} \tag{45}$$

The relations show that a decrease in film height results in a cubic increase in load capacity. The total change in film height of each slipper is dependent on the joints that are related to the slipper and the rotational direction of these joints. For a joint to rotate counter clockwise (ccw), the corresponding slippers right of the joint should have a higher load capacity compared to the corresponding slippers left of the joint. For a joint to rotate clockwise (cw), the corresponding slippers left of the joint should have a higher load capacity compared to the corresponding slippers right of the joint. As an example, looking at Fig. 5a, for joint 11 to make a ccw rotation, slipper 3 and 4 need a decrease in film height while slipper 1 and 2 remain an equal or have an increase in film height. It is important that the total change in film height should not exceed the minimum film height under each slipper in the undeformed configuration, since this would re-introduce solid to solid contact.

2.4 Design Rules

To design such a whiffletree supported large deforming hydrostatic bearing, the following rules of thumb, based on the previous models, should be followed:

1. Minimize the slipper length given the maximum slipper compression, number of whiffletree layers and bearing length.
2. Increase the number of whiffletree layers given an increase in bearing length.
3. Minimize the joint rotational stiffness.
4. Maximize the joint normal- and shear stiffness.
5. Maximize the ratio between slipper tilt stiffness and bottom layer joint rotational stiffness.

3 Model Validation

To validate the design, obtain the difference between a single, double and triple layer whiffletree and find the relation between the translation of the top joint with respect to the track, a case study is presented where the parametric values used are shown in Tab. 1. A typical application for this case study could be a hydraulic motor or pump that has four followers on a rotating cam which comprises a sinusoidal track. First, the footprint of the bearing is determined using a maximum allowable compression of 10% and a joint height to length ratio of two over five [2, 16, 21]. The amplitude of the wave is chosen to be 10% of the wavelength where the wavelength is set at 1m. The resulting bearing height of a single slipper, single layer whiffletree, double layer whiffletree and triple layer whiffletree are shown in Fig. 10. The results show that a single layer whiffletree has the lowest height for a bearing length up to 5.4% of the wavelength. Between a

Description	Parameter	Value	Unit
wavelength	λ	1	m
amplitude	A	0.1	m
bearing length	L_b	0.25	m
joint height factor	u	0.4	-
maximum compression	e	0.1	-
load capacity slipper	W	200	N
slipper length (single)	L_s	0.125	m
slipper length (double)	L_s	0.0625	m
slipper length (triple)	L_s	0.3125	m
film height factor (layer 1)	h_{f1}	0.2	-
film height factor (layer 2)	h_{f2}	0.1	-
film height factor (layer 3)	h_{f3}	0.05	-
film height factor (bottom)	h_{fB}	0.025	-

Table 1: Parametric values used in the case study.

Description	Parameter	Layer	Value	Unit
rotational stiffness	k_r	Top	105.6	Nm/rad
		1	20.19	
		2	3.810	
		3	1.928	
normal force	F_n	Top	2689	N
		1	1718	
		2	958.3	
		3	506.0	
shear force	F_s	Top	174.9	N
		1	26.54	
		2	4.033	
		3	0	

Table 2: Minimum rotational stiffness and maximum normal and shear force acting on each individual joint in their corresponding layer.

bearing length of 5.4% and 10.9% of the wavelength, a double layer whiffletree performs best. For a bearing length of 10.9% of the wavelength or higher, a triple layer whiffletree is the preferred option in regards to the total bearing height. The total bearing length is set at 25% of the wavelength, resulting in a triple layer whiffletree as the desired configuration regarding the total bearing footprint.

To analyze the rigid body model from Sec. 2.2, it is compared with a Finite Element Model (FEM) using Comsol Multiphysics. In the FEM, the multibody dynamics toolbox is used to model the bearing. The linkages are modelled as rigid beams, using the rigid domain function and the joints are modelled as hinge joints. The top joint has a prescribed x position, a variable y position and is constrained in rotation. The slippers have a prescribed y_s position and angle θ as function of its x_s position, which are given by Eqn. (17) and (18). In the simulation, the top joint travels for a full wavelength. Figure 11a shows the results of the simulation run with FEM and run with the analytical model for a triple layer whiffletree. Only the leftmost joint angle of each layer is shown since the remaining joints in the same layer show equal behavior with the difference of a phase shift.

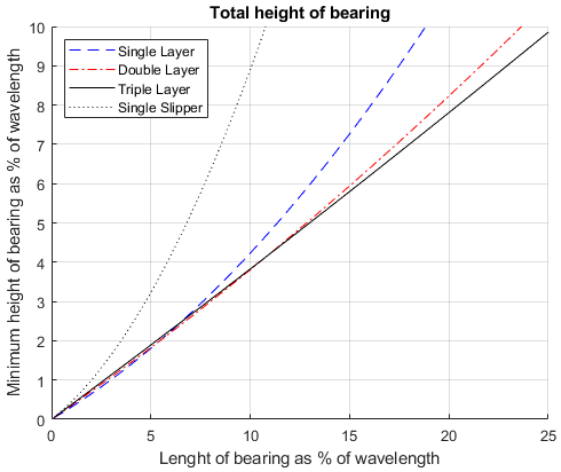

Figure 10: Total bearing height as function of bearing length for a single, double and triple whiffletree and a single slipper bearing.

The obtained kinematics are used to find the rotational stiffness, maximum normal force and maximum shear force acting on each individual joint. The load capacity acting on each slipper in the undeformed configuration for this case study is set at 200N. The difference in load capacity is obtained by defining the total flight height for each slipper to facilitate the correct rotational directions for their corresponding joints. For each layer a maximum percentage of change in film height is allowed as shown in Tab. 1. For each slipper it is determined if the film height should decrease to supply the required force difference to rotate the corresponding joint for each layer. The total change in film height for each individual layer is then obtained by taking the sum of the defined change in film height for each layer. This is done for each whiffletree position on the track and the maximum normal- and shear force acting on the joint and the minimum rotational stiffness required for each joint in the corresponding layer is given in Tab. 2.

The slipper angle, as shown in Fig. 9, of the first slipper is obtained using a relation between slipper tilt stiffness and bottom joint rotational stiffness of one, two and three orders of magnitude where the results are shown in Fig. 11b.

To find the influence of the number of whiffletree layers on the joint maximum pivot angles, the joint pivot angles of a

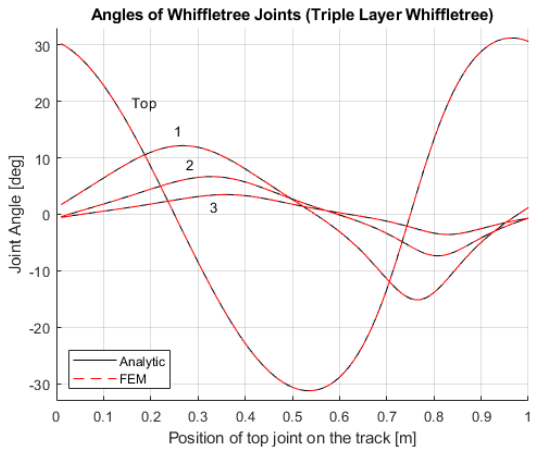

(a) Joint pivot angles of the FEM and analytical model compared for a triple layer whiffletree.

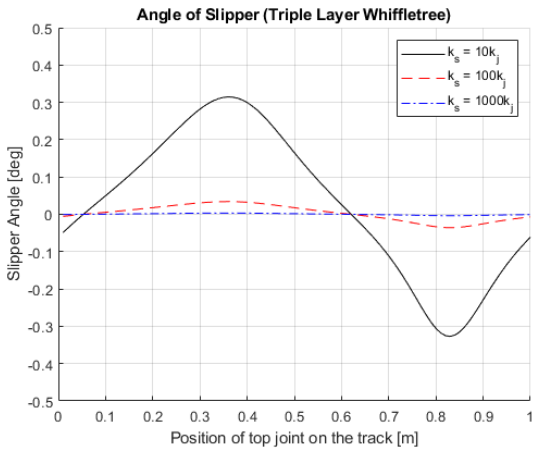

(b) Slipper pivot angle of a triple layer whiffletree with a rotational stiffness ratio of 10, 100 and 1000.

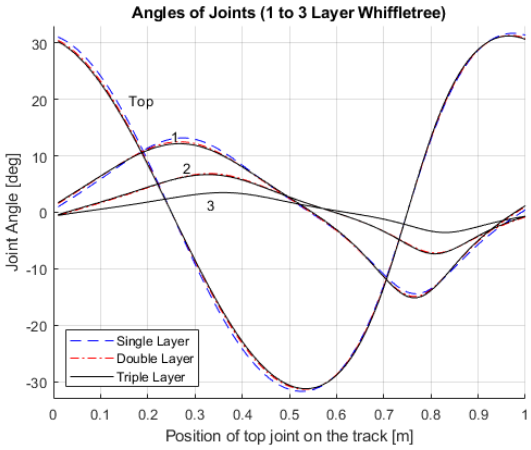

(c) Joint pivot angles of a single, double and triple layer whiffletree compared.

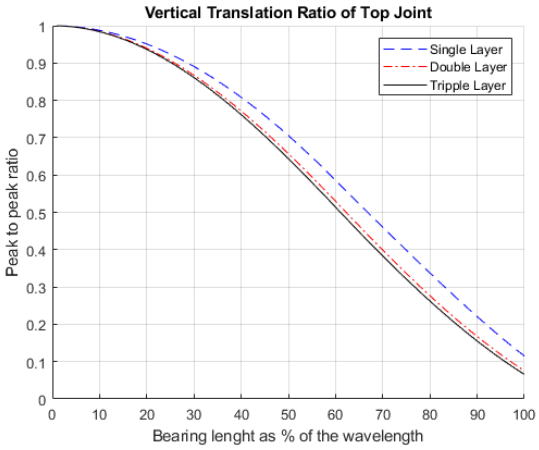

(d) Peak to peak ratio between the vertical translation of the top joint with respect to the amplitude of the track.

Figure 11: Results obtained using the use case presented in Sec. 3. Showing the comparison between the joint angles of a triple layer whiffletree using the FEM and analytical model (a), the first slipper angle (b), joint angles for a single, double and triple layer whiffletree (c) and the peak to peak ratio between top joint vertical displacement and the track (d).

single, double and triple layer whiffletree are compared using the parametric values from Tab. 1. The results are presented in Fig. 11c.

Finally, the ratio between the vertical translation of the top joint with respect to the amplitude of the track as function of the total bearing length is given in Fig. 11d for a single, double and triple layer whiffletree configuration. This ratio is determined by dividing the peak to peak value of the top joint with the peak to peak value of the track.

4 Discussion

4.1 Design Model

The design model provides a method to design a 2D whiffletree supported large deforming hydrostatic bearing. There are a few limitations to this design. Firstly, conventional hinge joints are used to model the joints in the system compared to the preferred compliant joints. This is done since rigid body mechanics can be used in combination with the conventional hinge joints. Since the scope of this project is to find a general solution regarding the kinematics and kinetostatics, this simplification is valid. Secondly, the total perimeter of the bearing increases when multiple smaller slippers are connected together compared to a single slipper of equal length and width. The increase in bearing perimeter results in an increase in fluid losses of the bearing. Thirdly, the total joint length is restricted by the total linkage length. This is shown in the assumption that the bottom layer joint has a length of half the slipper length and each ascending joint is twice the length of the joint one layer below, resulting in the maximum allowable bearing length on each linkage. Finally, the slippers are placed directly next to each other. When the bearing moves into a concave configuration, the slippers need to pass through each other which results in

jamming. This can be solved by adding a small gap between the slippers large enough such that the slipper can pass without contact.

4.2 Model Validation

A case study is given in the model validation. Looking at the total bearing height shown in Fig. 10 it can be seen that an increase in whiffletree layers is advantageous if the total bearing length increases. It is also noted that the total bearing height of the use case is within 10% of the amplitude of the wavelength. Furthermore, the amplitude of the wavelength is approximately 1000 times the average film height of the fluid film. Thus, considering the statements given in [1], the bearing and counter surface used in the use case are defined as large deforming. Figure 11a shows the joint pivot angles for the FEM and analytical model. The obtained results for the FEM and analytical model have no noticeable difference, thus validating the design model presented in Sec. 2.2. Furthermore, an asymmetry in the joint angles while moving over the track is noted. This means that the whiffletree behaves differently when moving through the concave and convex configurations of the track. Looking at the joint pivot angles shown in Fig. 11c, it is shown that the addition of whiffletree layers has a negligible small impact of the joint pivot angles of the ascending layers. This can be explained by looking at the angle of the corresponding linkage with the horizontal. The angle of the linkage with the horizontal is almost equal to the angle of the gradient of the track at the same position. An increase in whiffletree layers does not change this orientation. Thus, no significant change in joint pivot angle is noted due to an increase in whiffletree angles. Looking at the top joint pivot angle, it can be seen that the maximum required angle is equal to the maximum angle of the gradient of the track. Meaning that the top joint is required to rotate the total system so it remains on average parallel to the track. Furthermore, it is shown that an increase in whiffletree layers results in a decrease in slipper length, and thus a decrease in required compression of each slipper. The slipper pivot angle is shown in Fig. 11b for a rotational stiffness ratio between slipper and bottom layer joint of one, two and three orders of magnitude. It is shown that for a ratio of three orders of magnitude, no noticeable change in slipper pivot angle is noted. Meaning that a rotational stiffness ratio between slipper and bottom layer joint of at least three orders of magnitude is desired. The vertical translation ratio of the top joint with respect to the track is given in Fig. 11d. It is shown that this ratio decreases when the bearing length increases as a percentage of the wavelength. Thus, a small bearing length as a percentage of the wavelength is required if an identical path should be followed between the top joint and the track. Finally, looking at the resulting stiffness and forces acting on each individual joint shown in Tab. 2, it is shown that the normal force acting on each joint is significantly larger compared to the shear force. This means that the shear stiffness of the joint could be lower compared to the normal stiffness of the joint if the same displacement is allowed. Looking at the ratio's of the rotational stiffness, normal force and shear force between each ascending layer, a pattern is found for the normal and shear force ratio of approximately 1.7 and 6.65 respectively. However, looking at the rotational stiffness of each joint, no real pattern is obtained.

5 Conclusion

This work showed the potential of a whiffletree support system to increase the deformability of 2D compliant hydrostatic bearings to follow non-constant curvature counter surfaces. The whiffletree support is used to connect multiple slippers together allowing each slipper to maintain a parallel position with the counter surface. A quadratic relation is found between the slipper compression and length resulting in a desired decrease in slipper length to reduce the required slipper compression. It is shown that an increase in whiffletree layers does not affect the joint pivot angles of the ascending layers. However, the addition of extra layers in the whiffletree does lower each individual slipper length, reducing the required compression of the slipper. It is shown that a ratio of at least three orders of magnitude between the slipper tilt stiffness and bottom layer joint is required to show no noticeable influence caused by tilting of the slipper. To conclude, the whiffletree can be used to rotate smaller slippers reducing its required compression while maintaining load capacity. This can be used to transfer applications that require high loading capacities over counter surfaces that have a non-constant surface like a sine wave while eliminating the effect of stick-slip and reducing the effect of friction and wear compared to conventional slider bearings.

References

[1] Nijssen, J. P. A., and van Ostayen, R. A. J., 2020. "Compliant Hydrostatic Bearings Utilizing Functionally Graded Materials". *Journal of Tribology,* **142**(11), 06. 111801.

[2] van Beek, A., and Segal, A., 1997. "Rubber supported hydrostatic thrust bearings with rigid bearing surfaces". *Tribology International,* **30**(1), pp. 47–52.

[3] van Ostayen, R. A. J., 2014. *The Hydro–Support: An Elasto–Hydrostatic Thrust Bearing with Mixed Lubrication*.

[4] van Beek, A., and Lepic, L., 1996. "Rubber supported hydrostatic thrust bearings with elastic bearing surfaces of infinite length". pp. 45–50.

[5] Liang, X., Yan, X., Ouyang, W., Wood, R. K. K., and Liu, Z., 2019. "Tribology International Thermo-Elasto-Hydrodynamic analysis and optimization of rubber-supported water-lubricated thrust bearings with polymer coated pads". *Tribiology International,* **138**(May), pp. 365–379.

[6] Hooke, C. J., 1997. "Elastohydrodynamic lubrication of soft solids". *Tribology Series,* **32**, pp. 185–197.

[7] Nijssen, J. P. A., Kempenaar, A., and Diepeveen, N., 2018. "Development of an interface between a plunger

and an eccentric running track for a low-speed seawater pump".

[8] Belyi, A., Osadchy, G., Efanov, D., and Shestovitskiy, D., 2018. "Implementation of the Continuous Monitoring System for Technical Condition of the St. Petersburg Arena Stadium Sliding Roof". *Proceedings of 2018 IEEE East-West Design and Test Symposium, EWDTS 2018*.

[9] Stachowiak, G. W., and Batchelor, A. W., 2008. "Engineerng Tribology". p. 769.

[10] Liu, Z., Wang, Y., Cai, L., Zhao, Y., Cheng, Q., and Dong, X., 2017. "A review of hydrostatic bearing system: Researches and applications". *Advances in Mechanical Engineering,* **9**(10), pp. 1–27.

[11] Yeniceli, S. C., 2014. "Design Optimization of Whiffletree Systems for Wind Turbine". p. 123.

[12] Dierickx, P., 2007. "The European extremely large telescope (E-ELT)". *Highlights of Spanish Astrophysics IV - Proceedings of the 7th Scientific Meeting of the Spanish Astronomical Society, SEA 2006*(March), pp. 15–28.

[13] Baffes, C., Mast, T., Nelson, J., Ponslet, E., Stephens, V., Stepp, L., and Williams., E. C., 2008. "Primary mirror segmentation studies for the Thirty Meter Telescope". *Advanced Optical and Mechanical Technologies in Telescopes and Instrumentation,* **7018**(70180), p. 70180S.

[14] Nijenhuis, J., Hamelinck, R., Braam, B., and Cayrel, M., 2010. "Meeting highest performance requirements for lowest price and mass for the M1 segment support unit for E-ELT". *Ground-based and Airborne Telescopes III,* **7733**(August 2010), p. 77332H.

[15] Tian, Y., Shirinzadeh, B., Zhang, D., and Zhong, Y., 2010. "Three flexure hinges for compliant mechanism designs based on dimensionless graph analysis". pp. 92–100.

[16] Gomez, R. F. P., Nijssen, J. P. A., and van Ostayen, R. A. J., 2010. "Design of a Compliant Hinge based on Closed Form Pressure Balancing". pp. 1–12.

[17] Yastrebov, V. A., Anciaux, G., and Molinari, J. F., 2014. "The contact of elastic regular wavy surfaces revisited". *Tribology Letters,* **56**(1), pp. 171–183.

[18] Gao, Y. F., Bower, A. F., Kim, K. S., Lev, L., and Cheng, Y. T., 2006. "The behavior of an elastic-perfectly plastic sinusoidal surface under contact loading". *Wear,* **261**(2), pp. 145–154.

[19] Y. Jia, 2018. "Gaussian and Mean Curvatures". pp. 1–7.

[20] Zhang, Y., Finger, S., and Behrens, S., 2010. *Introduction to Mechanisms*. Carnegie Mellon University.

[21] Castelli, V., Rightmire, G. K., and Fuller, D. D., 1967. "On the Analytical and Experimental Investigation of a Hydrostatic, Axisymmetric Compliant-Surface Thrust Bearing".

4

Joint Moment

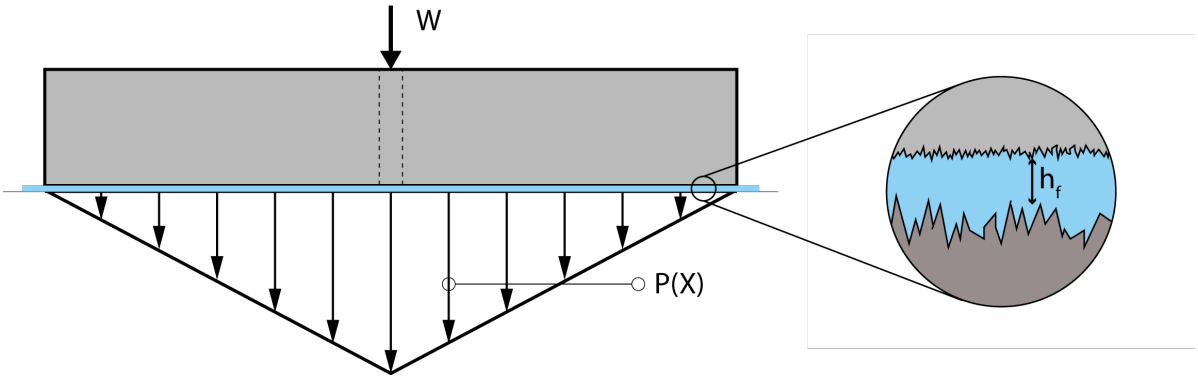

Figure 4.1: Fluid film layer between hydrostatic bearing and counter surface and the influence of surface roughness.

In this chapter, further explanation regarding the moments required to rotate the joints is given. The moments acting on the joints are obtained by a change in load capacity of each individual slipper. This change in load capacity can be achieved by a difference in the height of the fluid film layer between slipper and counter surface. The relation between fluid film height and load capacity is defined by:

$$W \propto \frac{1}{h^3} \tag{4.1}$$

where W is the load capacity and h is the fluid film height under each slipper. To prevent solid-to-solid contact between the slipper and its counter surface, the total change in fluid film height can not exceed the fluid film height present under the bearing in its undeformed configuration. Taking into account surface roughness, as shown in figure 4.1, and other unexpected perturbations in the fluid film height, the total change in film height used to generate the moments acting on each joint should be large enough to supply the required moment, but small enough to prevent solid to solid contact.
The change in fluid film height under each layer is dependent on the required moment of each joint that is dependent on that specific slipper. To specify, a joint is dependent on a slipper if a line can be drawn through linkages from the slipper to the joint where the line can not go downwards.
Figure 4.2 shows an example of the dependency of each individual slipper on the joints in the system. In the top half of the figure, a whiffletree is shown where the rotational directions of each joint is given to follow a concave counter surface. The bottom half of the figure provides a scheme which shows if the flight height of the corresponding part of the slipper should be changed to supply the required moment for the dependent joint in that specific layer. Note that for each slipper the right and left part are shown in the scheme. This is to show which part of the slipper should have an increased load capacity to rotate the joint directly connected to the slipper.
Looking at the relation between the rotational stiffness of the joints between layers, it is desired if the maximum required rotational stiffness increases for ascending layers. This would result in an equal ratio between

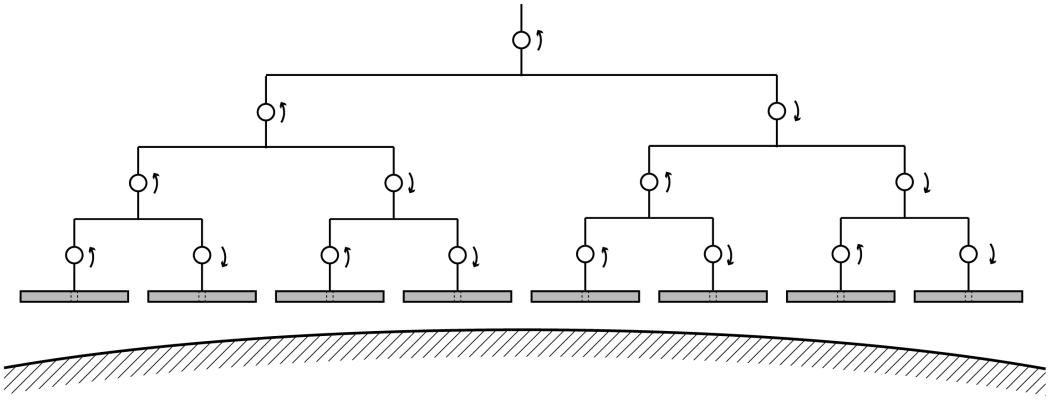

LAYER 1									X	X	X	X	X	X	X	X
LAYER 2					X	X	X	X	X	X	X	X				
LAYER 3			X	X	X	X					X	X	X	X		
BOTTOM LAYER		X	X			X	X			X	X			X	X	

Figure 4.2: (Top) Rotational directions of the joints in a triple layer whiffletree that moves over a concave track. (Bottom) Influence scheme which shows for each slipper if load capacity should be increased to rotate the corresponding joint in each layer. To rotate the joint connected to each slipper it is shown which side of the slipper should have an increased load capacity.

normal and rotational stiffness for each joint since the normal force, and thus normal stiffness, of the joints in ascending layers increases. To obtain a larger rotational stiffness for joints in ascending layers, an increase in moment is required.

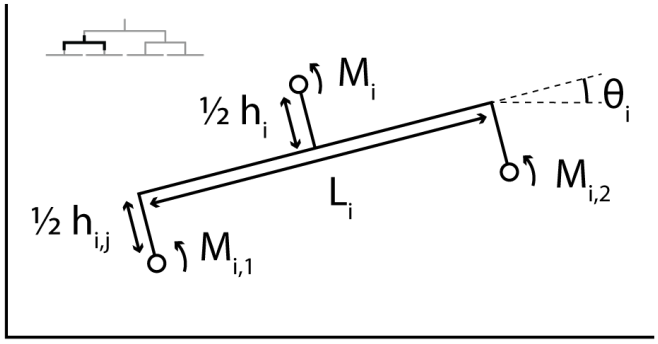

Figure 4.3: Linkage of a whiffletree with the corresponding parameters.

The moment acting on each joint M_i, as shown in figure 4.3, is defined by:

$$M_i = F_{\mathrm{a}(i)} \frac{L_i}{2} + F_{\mathrm{b}(i)} \frac{(h_i + h_{i,j})}{2} + M_{i,1} + M_{i,2} \tag{4.2}$$

where h_i and $h_{i,j}$ are the joint heights of the previous and current layer respectively, L_i is the linkage length and $F_{\mathrm{a}(i)}$ and $F_{\mathrm{b}(i)}$ are defined by:

$$F_{\mathrm{a}(i)} = F_{\mathrm{y}(i,1)} \cos(\theta_i) - F_{\mathrm{x}(i,2)} \sin(\theta_i) \tag{4.3}$$

$$F_{\mathrm{b}(i)} = F_{\mathrm{y}(i,1)} \sin(\theta_i) - F_{\mathrm{x}(i,2)} \cos(\theta_i) \tag{4.4}$$

where θ_i is the angle of the joint with the horizontal and $F_{\mathrm{x}(i,j)}$ and $F_{\mathrm{y}(i,j)}$ are the forces acting on the joint one layer below in x and y direction respectively. In equation (4.2) it is shown that the moment acting on a

joint is dependent on the moment acting on the joints one layer below. This could result in a reduction in total moment for a joint in an ascending layer if the sum of the moments of the two joints one layer below is in the opposite direction. To prevent this, the percentage of allowed change in total fluid film height to obtain a change in load capacity is unequally divided for each layer where this number should increase for each ascending layer. In example, the total change in film height to rotate the top layer joint should be larger compared to the change in film height to rotate a joint in one of the descending layers.
With the percentage of change in film height known for each layer, the total moment acting on each joint can be obtained. The rotational stiffness is then defined by:

$$k_{\mathrm{r}} = \frac{M}{\phi} \tag{4.5}$$

where M is the moment acting on the joint and ϕ the rotational angle of the joint. Te rotational stiffness is then obtained for each joint in the system for each configuration of the whiffletree on the counter surface. The maximum rotational stiffness of each joint in a layer is then defined as the minimum required rotational stiffness for the joints in the same layer.

5

Coupled Multi-Slipper Hydrostatic Bearing

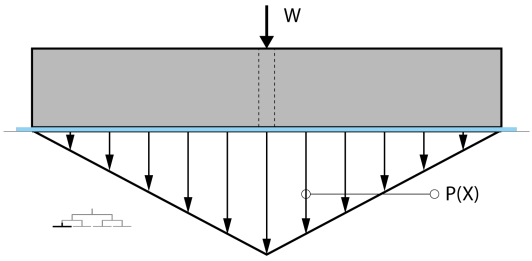

(a) Pressure profile of a single slipper and inlet bearing.

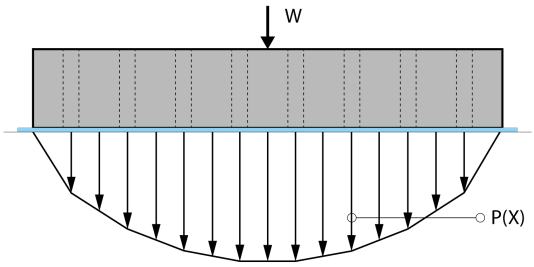

(b) Pressure profile of a multi-slipper and inlet bearing.

Figure 5.1: Pressure profile of a single and multi-slipper bearing.

In the paper, multiple slippers are connected by the use of a whiffletree support system. This allowed for an increase in deformability of the bearing at the cost of an increase in fluid losses. To prevent the increase of fluid losses in the bearing, the slippers could be made out of one continues elastic material which is discretely supported. Since the perimeter of the coupled multi-slipper bearing is equal to the perimeter of a single slipper with equal length and width, the fluid losses remain equal. Furthermore, the pressure profile also changes due to the coupling of the slipper. Figure 5.1a shows the pressure profile of a single slipper bearing with one inlet and no recess area and figure 5.1b shows the pressure profile of a coupled multi-slipper bearing with multiple inlets and no recess area. It is shown that the coupled multi-slipper bearing pressure profile area is larger compared to the single slipper bearing pressure profile area of equal dimensions which results in an increase in load capacity of the bearing. To obtain the pressure profile of a coupled multi-slipper bearing, a design model is given. The design model is used to determine the slipper length and momentary rotation point of each slipper to assure a zero moment and equal load capacity on each slipper in the bearing. This is desired since this allows for equal joint requirements in each layer of the whiffletree support. Then, a case study is presented to show an example of the model given in this section.

5.1. Design Model

To obtain the pressure profile of the coupled multi-slipper bearing, multiple additions are made to the design model given in section 2 of the paper. Figure 5.2 represents a pressure profile obtained while using the method described in this section where, due to symmetry in the pressure profile, only the left part of the profile is shown. The slipper lengths and the corresponding pressure profile is located in the top of the figure. The fluid flow chart and their connecting points, also called nodes, are given in the bottom, with the flow going from node to node. The flow Q in any part of the lubricant film is defined by:

$$Q = \int q_x dx \tag{5.1}$$

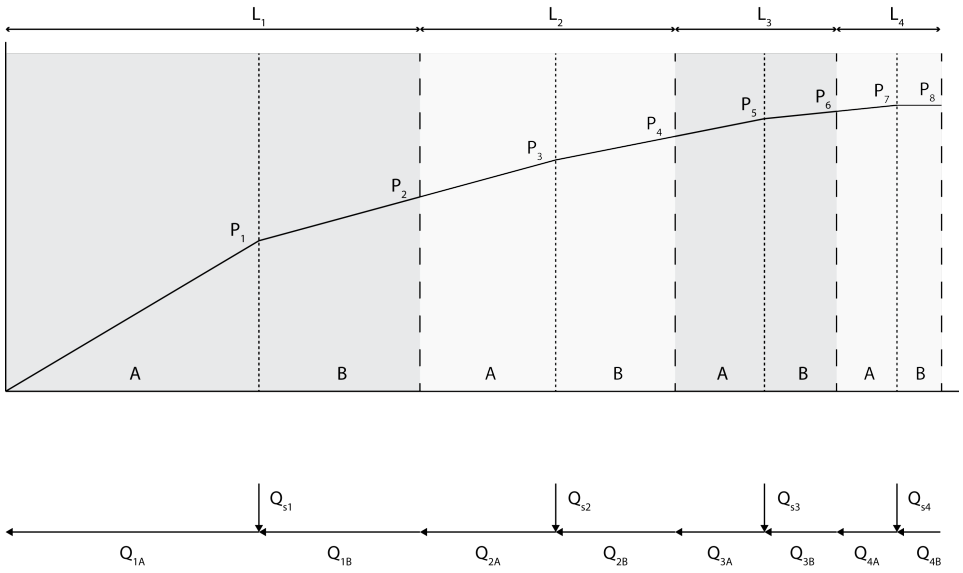

Figure 5.2: In the top, the left side of a linear pressure profile for an asymmetric slipper configuration is given. In the bottom, the corresponding flow chart is given. The tips of the arrows represent nodes, the dotted lines represent the inlets of the slippers, the dashed lines show the edges of the slippers and the left and right sections of the slippers are indicated with an A (left) or B (Right).

where q_x is the volumetric flux given by the Reynolds equation defined by:

$$q_x = -\frac{h^3}{12\eta} P_{,x} \tag{5.2}$$

where h is the film height, $P_{,x}$ is the gradient in x-direction of the pressure distribution and η is the fluids dynamic viscosity. If an incompressible fluid is used, the volumetric flow rate in any point of the lubricant film must remain constant. Thus, the flow under two adjacent slippers must be equal defined by:

$$Q_n = Q_{n+1} \tag{5.3}$$

where Q_n is the flow of the first slipper and Q_{n+1} is the flow of the second slipper. Furthermore, the total flow after the inlet must remain the same as the flow before the inlet and the flow of the inlet combined defined by:

$$Q_\mathrm{A} = Q_\mathrm{s} + Q_\mathrm{B} \tag{5.4}$$

where Q_A is the flow under the slipper after the inlet, Q_B is the flow under the slipper before the inlet and Q_s is the flow of the corresponding inlet. The flow rate of the inlet is determined by a restrictor and is defined by:

$$Q_\mathrm{s} = G_\mathrm{s}(P_\mathrm{s} - P_\mathrm{p}) \tag{5.5}$$

where G_s is the hydraulic resistance of the restrictor, P_s the supply pressure and P_p the pressure under the bearing at the inlet. For this model, a linear capillary restrictor is used defined by:

$$G_\mathrm{s} = \frac{\pi d_\mathrm{r}^4}{128\eta l_\mathrm{r}} \tag{5.6}$$

where d_r is the restrictor diameter, η the dynamic viscosity of the fluid and l_r the restrictor length. Substituting Eqn. (5.2) in Eqn. (5.3), Eqn. (5.2) and (5.5) in Eqn. (5.4) and solving them for each node gives the total pressure profile. The load capacity per unit length W length is now defined by:

$$W = \int P dx \tag{5.7}$$

where P is the pressure profile. For a linear pressure profile, the load capacity per unit length between two nodes under the slipper is defined by:

$$W = \frac{1}{2}(P_{i+1} + P_i)L \tag{5.8}$$

where P_{i+1} and P_i are respectively the pressures at each node and L is the length between the nodes. To assure equal load capacity on the slippers, the following equation must hold for each slipper:

$$W_{s(n)} = W_{s(n+1)} \tag{5.9}$$

where W_s is the load capacity of the slipper. To find the momentary rotation point of a slipper, the moment acting on each side of the rotation point must be equal defined by:

$$M_A = M_B \tag{5.10}$$

where M_A is the moment acting on the left side of the slipper and M_B is the moment acting on the right side of the slipper. Both moments are defined by:

$$M = \int xPdx \tag{5.11}$$

5.2. Example

Description	Parameter	Value	Unit
Supply Pressure	P_s	0.5E5	Pa
Ambient Pressure	P_0	0	Pa
Restrictor Diameter	d_r	1E-3	m
Restrictor Length	l_r	h_j	m
Dynamic Viscosity	η	8.9E-4	Pa s
Wavelength	λ	1	m
Amplitude	A	0.1	m
Film Height	h	1E-4	m
Bearing Length	L_b	0.25	m

Table 5.1: Parametric values used to obtain the pressure profile of coupled multi-slipper whiffletree configurations configurations.

To provide an example of the design method described in section 5.1 a use case is made. The parametric values used are shown in table 5.1. The joint height is chosen as half the shortest slipper length and is increased by a factor two for each ascending layer. The obtained slipper lengths, bottom layer joint height and load capacity on each slipper per unit length are given in table 5.2 for a single layer whiffletree configuration, in table 5.3 for a double layer whiffletree configuration and in table 5.4 for a triple layer whiffletree configuration. With the obtained joint height and slipper lengths for the three different configurations, the joint pivot angles are given as shown in figure 5.3a. Finally, figure 5.3b shows a comparison for the triple layer whiffletree configuration between the joint pivot angles of the non-coupled bearing configuration as given in the paper and the coupled bearing configuration obtained with this example. Note that equal initial values are used for both configurations.

Description	Parameter	Value	Unit
Length Slipper 1	L_{1A}	0.0732	m
	L_{1B}	0.0518	m
Joint Height	h_j	0.0250	m
Load Capacity	W	1025	N/m

Table 5.2: Slipper lengths, joint height and load capacity of a coupled multi-slipper single layer whiffletree configuration, where the slipper length left of the momentary rotation point is noted with an A and the slipper length right of the momentary rotation point is noted with a B.

Description	Parameter	Value	Unit
Length Slipper 1	L_{1A}	0.0472	m
	L_{1B}	0.0320	m
Length Slipper 2	L_{2A}	0.0232	m
	L_{2B}	0.0226	m
Joint Height	h_j	0.0092	m
Load Capacity	W	985	N/m

Table 5.3: Slipper lengths, joint height and load capacity of a coupled multi-slipper double layer whiffletree configuration, where the slipper length left of the momentary rotation point is noted with an A and the slipper length right of the momentary rotation point is noted with a B.

Description	Parameter	Value	Unit
Length Slipper 1	L_{1A}	0.0284	m
	L_{1B}	0.0192	m
Length Slipper 2	L_{2A}	0.0138	m
	L_{2B}	0.0134	m
Length Slipper 3	L_{3A}	0.0127	m
	L_{3B}	0.0126	m
Length Slipper 4	L_{4A}	0.0124	m
	L_{4B}	0.0124	m
Joint Height	h_j	0.0050	m
Load Capacity	W	615	N/m

Table 5.4: Slipper lengths, joint height and load capacity of a coupled multi-slipper triple layer whiffletree configuration, where the slipper length left of the momentary rotation point is noted with an A and the slipper length right of the momentary rotation point is noted with a B.

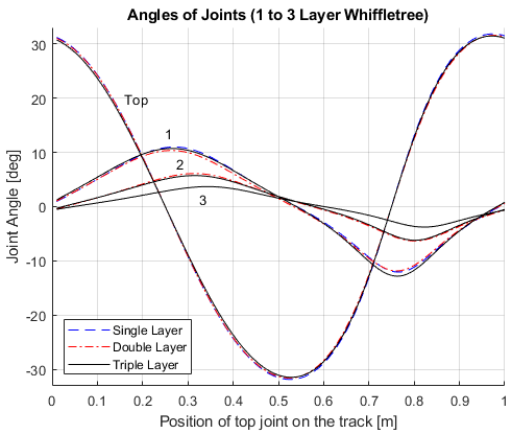

(a) Joint pivot angles for a single, double and triple layer whiffletree compared.

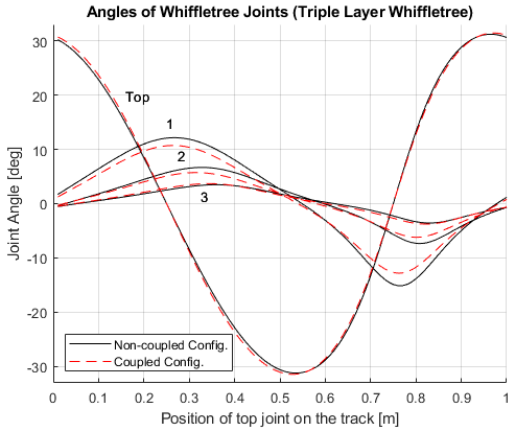

(b) Joint pivot angles for the non-coupled multi-slipper bearing and coupled multi-slipper bearing for a triple layer whiffletree configuration.

Figure 5.3: Joint pivot angles of the case study. The leftmost joint pivot angle is shown for each layer which is denoted by the layer number.

5.3. Film Thickness

The influence of the film height on the pressure profile, and thus load capacity, of the coupled multi-slipper bearing differs from the non-coupled multi-slipper bearing as presented in the paper in section 2 and chapter 4 of this thesis. As explained in section 5.1, the pressure profile of the bearing is directly related to the flow rate under the bearing. If an incompressible fluid is used, an equal flow rate under each part of the bearing must be maintained. So, the flow after each inlet should be equal to the flow before the inlet and the flow of the inlet combined. Since the slippers are attached to each other in the coupled multi-slipper hydrostatic bearing, the flow under each segment should also remain the same. To maintain an equal flow under each slipper segment, the pressure drop should change if a change in film height occurs. As seen in figure 5.2 the pressure drop of each segment is dependent on the pressure drop of its adjacent segments. This means that a change in film height in one segment could lead to a change in pressure drop in each other segments changing the total pressure profile. In other words, the pressure drop under a specific segment of the bearing is dependent on the flight height of each individual segment of the bearing. This means that the matrix showing the relation between the film height and load capacity of each slipper is non-diagonal. So, the difference in load capacity on each slipper to rotate each joint in the system can not be easily obtained by changing the flight height of the corresponding slipper. Instead, the total change in film height under the whole bearing should be taken into account for each configuration of the system on the track. This can introduce new problems since the slippers lengths obtained in section 5.1 could require a larger change in film height of the slippers to generate a large enough moment to rotate each joint in the system.

6

Finite Element Model

In order to validate the kinematics of the whiffletree obtained in section 2.2 of the paper, a finite element analysis using COMSOL Multiphysics has been done. To analyze rigid- and flexible-body assemblies, the multibody dynamics module is used. The multibody dynamics module allows to create a combination of rigid and flexible rigid bodies, where the bodies can be subjected to large rotational and transnational displacements. A library of predefined joints is used to define the relation between different bodies or components in the system. A joint connects two bodies with attachments. This way, one component is constraint to follow a particular motion while the other component can move independently in space. The multibody dynamics module allows to combine flexible and rigid bodies in the system, allowing for an integration between compliant and rigid structures. Furthermore, the multibody dynamics module can be combined with the nonlinear structural materials module or the geomechanics module, to implement nonlinear material properties.

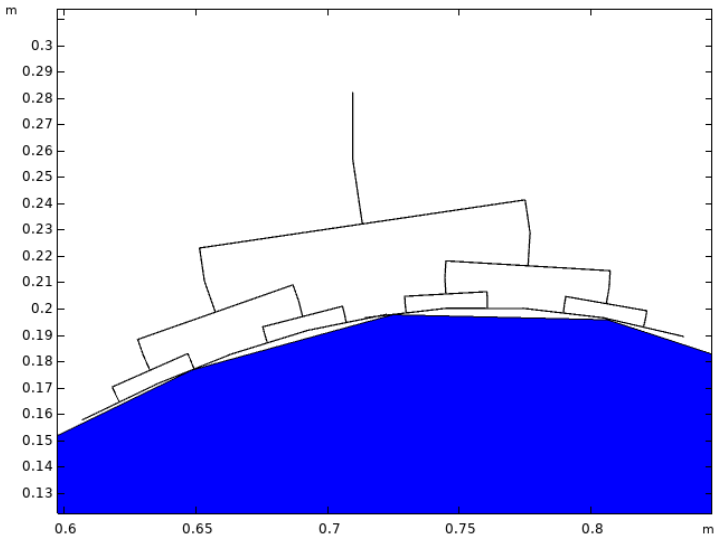

Figure 6.1: Rigid body model obtained using COMSOL Multiphysics.

For the validation of the kinematics obtained in the paper, the multibody dynamics module is used in combination with a time dependent study. The time dependent study is used to iterate over the time to move the bearing over the counter surface and obtain the angles of each steady state configuration. To model the whiffletree, a rigid body model is used as shown if figure 6.1. The system is build up out of a number of slippers which is defined by:

$$\#\text{Slippers} = 2^{\#\text{Layers}} \tag{6.1}$$

The slippers are connected to the linkage cells as explained in the paper, by hinge joints. Each component in the system is then made rigid using the rigid domain function. The density and center of rotation are then

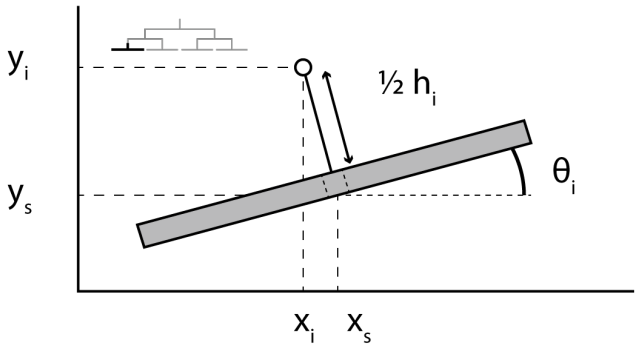

Figure 6.2: Single slipper with its corresponding parameters.

defined where the density of structured steel is used. The density will not influence the final results of the FEM validation but is required for the system to run. The slipper center of rotation is placed at position x_s and y_s as shown in figure 6.2. In the FEM analysis, the y_s position is prescribed and dependent on its x_s position as defined by:

$$y_s = A\sin(2\pi x_s) \tag{6.2}$$

where A is the amplitude of the track. To maintain a parallel position between the slipper and the gradient of the track at position x_s, a prescribed rotation θ_m to the slipper is given by:

$$\theta_m = \arctan\left(2\pi A\cos(2\pi x_s)\right) \tag{6.3}$$

To define the position of the total system on the track, the top joint is connected to a rigid vertical beam which has a prescribed x_{top} position, a variable y_{top} position and is constrained in rotation. The x_{top} position of this beam is placed on each discrete x position in the domain of the counter surface defined by:

$$0 < x_{top} < \lambda \tag{6.4}$$

where λ is the wavelength of the counter surface and the step size between each discrete x_{top} position is 0.01. Hinge joints are used to model the joints in the system since they allow a free rotation while restricting the movement in the x and y direction for a two dimensional system. The center of the joint is placed at the center of the connection between the two rigid parts. If desired, stiffness and damping can be added to the system and the moments and forces acting on each joint can be obtained using weak constraints or the penalty method.

Figure 6.3: Finite element model with a representation of the counter surface given.

The system is placed in its undeformed configuration on a flat counter surface as initial position as shown in figure 6.3. This reduces the computational times and possible errors that can occur by finding the correct initial configuration of the system. The system is then moved over one and a half sine wave. To obtain the

Description	Parameter	Value	Unit
wavelength	λ	1	m
amplitude	A	0.1	m
bearing length	L_b	0.25	m
joint height factor	u	0.4	-
slipper length	L_s	0.3125	m

Table 6.1: Parametric values used in the case study.

corresponding angles of the counter surface used in the paper, only the angles in the domain between x_{start} and x_{end} should be considered where x_{start} and x_{end} are defined by:

$$x_{start} = \frac{1}{4}\lambda + x_{offset} \tag{6.5}$$

$$x_{end} = 1\frac{1}{4}\lambda + x_{offset} \tag{6.6}$$

where λ is the wavelength used in the paper and x_{offset} is the flat surface used to place the system in its undeformed configuration as initial position. The resulting pivot angles of the FEM analysis and analytical model, where the same parametric values are used as in the case study of the paper shown in table 6.1, are shown in figure 6.4. It can be noted that no noticeable difference is shown between the FEM and analytical model.

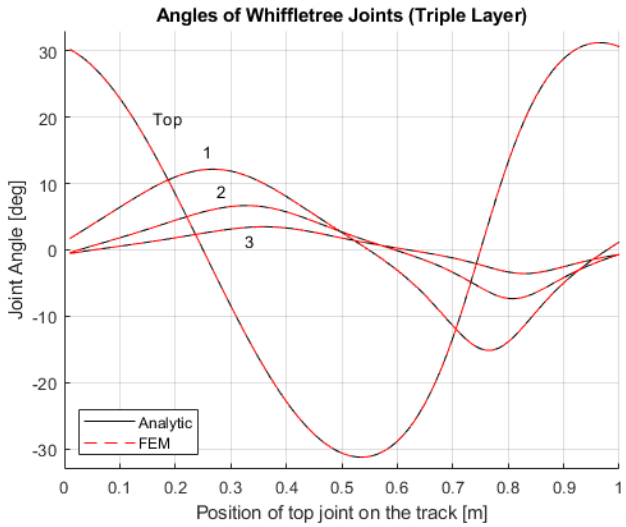

Figure 6.4: Joint pivot angles for a triple layer whiffletree obtained by the analytical and finite element model.

7

Discussion

The objective of this study is to improve the deformability of hydrostatic bearings by introducing a support system which allows for rotations of each slipper. This chapter will discuss the main results of this study. First, the results obtained in the background are evaluated. Then, the design and modelling of a 2D whiffletree based large deforming hydrostatic bearing is discussed. Following, the coupled multi-pad bearing is discussed. Finally, the FEM model used in this work is discussed.

7.1. Background

In chapter 1 and 2, the relevant literature and background on deformable hydrostatic bearings is provided. The literature found shows the use of an elastic support on the bearing [6, 8–10]. This support is used to allow for small rotations or tilting of the bearing to maintain a more parallel position between the bearing and counter surface. It is shown that these types of supports are limited to small deformations in the order of its film height. This shows that little to no research is done on the subject of large deforming hydrostatic bearings. The only result found on this topic shows a design method to design compliant hydrostatic slippers to follow large deformable non-constant counter surfaces. This research also provided the definition of large deforming non-constant counter surfaces as given in section 2.1. The results shown in section 2.1.2 shows that the required deformation, measured in its compression, of a tilted slipper is reduced compared to a slipper that remains parallel with the horizontal.

7.2. Paper

In chapter 3, a paper is provided that gives a design model to obtain the kinematics and kinetostatics of a 2D whiffletree support system used to connect multiple slippers to create a large deformable hydrostatic bearing. The design model is obtained using a two dimensional rigid body model where the joints are modelled as hinge joints. To make a more realistic model, elasticity of the parts should be taken into account. With elasticity implemented in the model, the dimensions of and stresses acting on the linkages can be obtained. Furthermore, contact joints should not be used into the elastic model since this would re-introduce the negative properties of wear, friction and backlash into the system. A solution to this would be the use of compliant joints as stated in the paper. However, the influence of compliance joints should be thoroughly evaluated. Critical parts would be the stresses in the joint and the displacement of the center of rotation during operation. To validate the assumption that the slippers remain parallel with the track, deformable slipper are required. The effect of these slippers, in terms of stresses, deformability and change in load capacity to rotate each joint, should also be thoroughly evaluated since this is one of the critical parts in the system. In [11] a design method is presented for such slippers. To enlarge the number of useful applications, the design model should be expanded to a three dimensional model. In appendix B and C a quick insight is given in the geometric layout of the slippers for a three dimensional whiffletree supported hydrostatic bearing. Finally, the design model is obtained by looking at each whiffletree configuration in its static equilibrium. In reality, the bearing will dynamically move over its counter surface. The dynamic behavior of the bearing is not evaluated and should therefore be further researched.

7.3. Coupled Multi-Slipper Hydrostatic Bearing

Chapter 5 provides a new insight in the coupling of the slippers to create a coupled multi-slipper hydrostatic bearing. The coupling of the slippers is required to reduce the fluid losses of the system. The advantage found was an increase in pressure profile area and thus an increase in load capacity of the bearing. The resulting slipper lengths and load capacities, obtained in the case study in section 5.2, show an increase in total load capacity if the number of whiffletree layers increases. This is due to the increased number of inlets which allows the pressure profile to be more of a parabolic shape. Looking at the joint pivot angles for a single, double and triple layer whiffletree in figure 5.3a only a negligible small change in pivot angles is noted. A more interesting result are the joint pivot angles of a triple layer whiffletree for the non-coupled, as shown in the paper, and coupled configuration compared as shown in figure 5.3b. This shows a decrease in the joint pivot angles for the coupled configuration. The decrease in pivot angles is most likely related to the decrease in total bearing height.

7.4. Finite Element Model

In chapter 6, the finite element model (FEM) analysis is described. The FEM analysis is used to validate the analytical model described in section 2 of the paper. The multibody dynamics module is used to model the whiffletree as a rigid body. To validate the analytical model, a difference in method or design approach is needed. The main difference between both methods is the position of each individual joint in the system. In the analytical model,the position and angle of each joint and slipper is obtained by a pre-defined set of equations and is dependent on the x position of the top joint. In the FEM analysis, the joints and slippers are allowed to move free where only the top joint has a prescribed x position. Furthermore, only the slipper y position and angle are pre-defined by a set of equations which are dependent on the slipper x position which is not pre-described. So the main difference is the method to otbain the position, and thus angle, of each individual joint. For the analytical model, everything is pre-defined and related to the top joint x position while the FEM analysis only has a pre-defined top joint x position where the remaining positions are obtained by the FEM program itself.

8

Conclusion

The main focus of this research was to increase deformability of hydrostatic bearings such that they can follow large deforming non-constant curvature counter surfaces. This goal is successfully accomplished by using the whiffletree support system to increase deformability of the total system while maintaining a low required deformation of the slippers. To design such systems, a design model is presented in the paper in chapter 3 where it is shown that a hydrostatic bearing to follow large deforming non-constant curvatures, as defined by [11], can indeed be obtained. Following, the most important conclusions of this work are summarized.

- A decrease in slipper length results in an approximate quadratic decrease in required slipper compression.
- The increase of whiffletree layers has a negligible small influence of the joint pivot angles of the higher layers.
- An increase in whiffletree layers is desired if the total bearing length increases in order to reduce the total bearing height.
- The ratio between slipper tilt stiffness and bottom joint rotational stiffness should be at least three orders of magnitude in order to maintain a close to parallel film under each slipper.
- The load carrying capacity of the coupled multi-slipper bearing is larger than the uncoupled multi-slipper bearing of the same dimensions.
- In the coupled multi slipper bearing, the flight height of each slipper is dependent on the flight height of each other slipper in the system.

9

Recommendations

This chapter provides several recommendations for further research. The use of a whiffletree support to increase the deformability of a large deformable hydrostatic bearing shows great potential. To continue the research in the design of large deformable hydrostatic bearings, a list of recommendations is given.

1. *Elastic model:* Analyze the effect of elasticity in the rigid body model.
2. *Compliant joints:* Add compliant joints in the system to remove the drawbacks from contact joints.
3. *Elastic slipper:* Add elastic slippers in the system, where the design model given in [11] could prove useful, and look at the behavior of the film layer under these new conditions.
4. *Coupled multi-slipper bearing:* Design, model and analyze the coupled multi-slipper bearing pad.
5. *Experimental setup:* Design an experimental setup to further validate the work in this and further research.
6. *3D model:* Expand the research to a 3D model.
7. *Dynamic behavior:* Research the performance of the bearing under dynamic behavior.

A

Analytical Model

This appendix gives an elaboration of the Matlab files used to obtain the analytical models. Each file used in this work is presented with a brief explanation so it can be ran, used and altered for further research.

A.1. Tilting Pad Effect

The results shown in figure 2.3 are obtained using the following script. In the script, three lines are plotted and simple mathematics are used to obtain the shortest length from the horizontal and tilted line to the sine wave. The maximum and average obtained values are given as a result in the model.

```
clear all
close all
clc

%% Parameters
alpha = 75; %Angle between pad and horizontal [deg]
b = 2.25; %Starting heigth reference line [m]
a = tand(alpha)*1; %Gradient of reference line [-]
n = 101; %Numbet of data points

x = linspace(0,0.5,n); %Array that represents all x data points

q = sin(x*2*pi+0.5*pi)+1; %Half of a sinewave shifted by pi/2 in the x direction and ...
    1 in the y direction
p = -a*x+b;             %First reference line under angle alpha
g = ones(1,n)*b;        %Second reference line parallel to the horizontal

h = p-q;
difference_tilted = cosd(alpha)*h;
difference_horizontal = g-q;

Maximum_distance_tilted = max(difference_tilted)
Maximum_distance_horizontal = max(difference_horizontal)
Average_distance_tilted = mean(difference_tilted)
Average_distance_horizontal = mean(difference_horizontal)

%% Figures
figure(1)
hold on
plot(x,q)
plot(x,p)
plot(x,g)
legend('Sine wave', 'Tilted line', 'Horizontal line')
xlabel('X-axis [m]')
ylabel('Y-axis [m]')
```

A.2. Required Slipper Compression

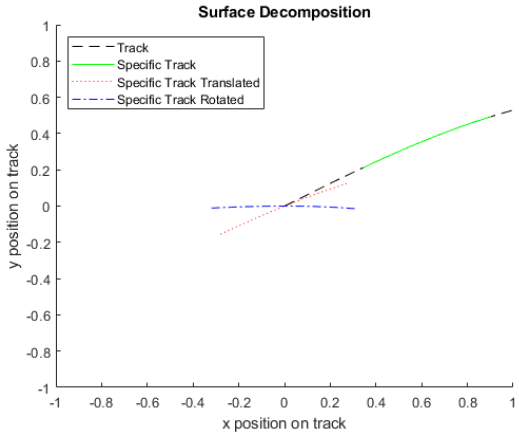

Figure A.1: Representation of the specific track during each step of obtaining the required slipper compression.

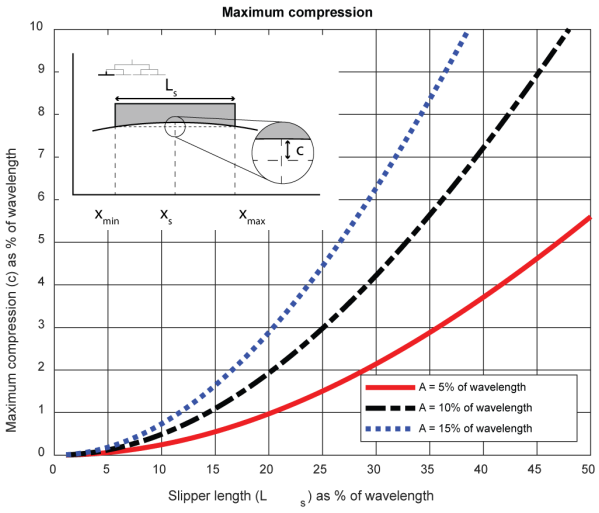

Figure A.2: Compression required of a single slipper, as function of the slipper length for a counter track with an amplitude of 5%, 10% and 15% of the wavelength respectively.

The required slipper compression, explained in section 2.1.1 of the paper, is obtained using the following script. In the script, a for loop is used to obtain the results for a single, double and triple layer configuration where the slipper compression is evaluated between a slipper length of 1% to 50% of the wavelength of 1m. The loop calls the function $Relative\_compression\_function$ which has as inputs the amplitude of the wave A, the scale factor of the length of the slipper r, the number of data points n and the starting length of the slipper $Slipper\_length$. The function follows the steps explained in section 2.1.1 of the paper where first the specific track is located. Then the specific track is translated an rotated to be placed at the origin as shown in figure A.1. Finally, the minimum and maximum y values are obtained to determine the compression. This is then repeated for each x_s position of the slipper to obtain the maximum compression for that specific slipper length. The results are shown in figure A.2.

```
clear all
close all
clc

%% Parameters
Amplitude = 0.05;        % Amplitude as percentage of the wave
Wavelength = 1;
n = 1000;                % Number of data points
N = 490;                 % Final scaling factor will be 1 + N/10
Slipper_length = 0.01;   % Length of slipper [m]

%% Loop
for q = 1:3
    A = Amplitude*q*Wavelength;
    for o = 1:N
        r = 1 + o / 10;
        [factor Mean_value] = Relative_compression_function(A,r,n, Slipper_length);
        Mean_value_array(o) = Mean_value;
        Compression(q,o) = factor(2,4);
        R_array(q,o) = r;
    end
end

%%
R_array_scaled = R_array;
R_array_scaled_percentage = R_array*0.01;
Mean_value_array_scaled = Mean_value_array;

```

```
%% Figures
figure(1)
hold on
q1 = plot(R_array_scaled_percentage(1,:)*100,Compression(1,:)*100, 'r-','LineWidth',3);
q2 = plot(R_array_scaled_percentage(2,:)*100,Compression(2,:)*100, 'k-.','LineWidth',3);
q3 = plot(R_array_scaled_percentage(3,:)*100,Compression(3,:)*100, 'b:','LineWidth',3);
title('Maximum compression')
xlabel('Bearing length (L_s) as % of wavelength')
ylabel('Maximum compression (c) as % of wavelength')
grid on
axis([0,50,0,10])
legend([q1 q2 q3], ('A = 5% of wavelength'), ('A = 10% of wavelength'), ('A = 15% of ...
    wavelength'),  'location', 'southeast')
```

```
function [factor, Mean_scaling_factor] = Relative_compression_function(Amplitude, r, ...
    n, Slipper_Length)

t = linspace(0, 1, n);           % Array of t values from 0 to 2 pi
A = Amplitude;
p = 1;
v = 0;
factor = ones(4,p);
Master_file = zeros(2*length(t),n);
y_diff = zeros(1,length(t));
y_diff_max = zeros(1,length(t));
t_decomposed = zeros(4,length(t));

    while v ≤ 1
        Length_slipper = Slipper_Length*r^(p-1);      % Length of the slipper can ...
            range between 0 and 1 [m]
        L = Length_slipper;

        for i = 1:length(t)
            angle = atan(A*cos(t(i)*2*pi)*2*pi);
            t_tot = cos(angle) * L;
            t_decomposed(1,i) = t(i);
            t_decomposed(2,i) = t(i) - t_tot / 2;
            t_decomposed(3,i) = t(i) + t_tot / 2;
            t_decomposed(4,i) = angle;
        end


        for j = 1:length(t_decomposed(1,:))
            t_new = linspace(t_decomposed(2,j), t_decomposed(3,j), n);
            P = [t_new; A*sin(t_new*2*pi)]; ...
                                                                                ...
                % X and Y coordinates of sine wave corresponding to slipper
            T = [t_decomposed(1,j); A*sin(t_decomposed(1,j)*2*pi)]; ...
                                                                    % ...
                Translation Matrix to get to the origin
            R = [cos(t_decomposed(4,j)) sin(t_decomposed(4,j)); ...
                -sin(t_decomposed(4,j)) cos(t_decomposed(4,j))];        % Rotation ...
                matrix clockwise around z axis
            P_final = R*(P-T); ...
                                                                        ..
                % Translate and Rotate array P
            Master_file((j-1)*2+1,:) = P_final(1,:);
            Master_file(j*2,:) = P_final(2,:);
        end

        for k = 1:length(t)
            x_values = Master_file((k*2)-1,:);
            y_values = Master_file((k*2),:);
            y_diff_max(k) = abs(max(y_values)-min(y_values));
        end


        y_diff_max_max(p) = max(y_diff_max);

```

```
46          if p ≤1
47              factor(p,1) = 0;
48              factor(p,2) = r;
49              factor(p,3) = 0.05*r^(p-1);
50              factor(p,4) = y_diff_max_max(p);
51          else
52              factor(p,1) = y_diff_max_max(p)/y_diff_max_max(p-1);
53              factor(p,2) = r;
54              factor(p,3) = 0.05*r^(p-1);
55              factor(p,4) = y_diff_max_max(p);
56          end
57
58          v = factor(p,3);
59
60          p = p + 1;
61      end
62
63      Mean_scaling_factor = mean(factor(2:(end-1),1));
64  end
```

A.3. Bearing Footprint

The bearing footprint, as explained in section 2.1.2 of the paper, is used to find the maximum dimensions of a single, double and triple layer whiffletree configuration with equal slipper length. The script to obtain the total height of the bearing as function of its length is given in this section. The total height is obtained using the equations found in the paper in section 2.1.2. The script is written such that it is valid for multiple layer configurations and thus is not limited to a single, double and triple whiffletree configuration. The height is obtained by finding the compression required of the slipper following using the function $compression\_function$ which is almost the same as the script of appendix A.2. The total slipper height is obtained by dividing the compression by the maximum allowable strain. The joint height is obtained by finding the joint length in each layer and multiplying it with the corresponding joint height factor. Figure A.3 shows the results obtained from the script for a single, double and triple layer whiffletree configuration.

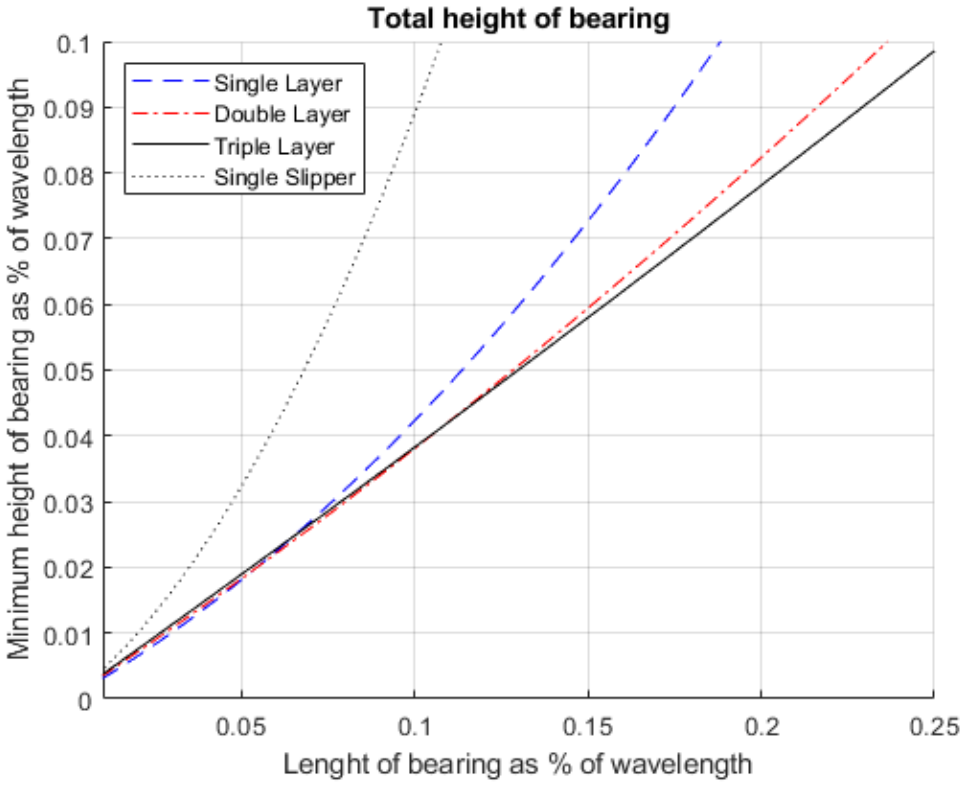

Figure A.3: Total bearing height as function of the bearing length for a single, double and triple layer whiffletree and a single slipper bearing. The corresponding track amplitude is 10% of the wavelength.

```
clear all
close all
clc

%% Parameters
max_strain = 0.1;                       % Maximum strain to assume linear behaviour ...
    in rubber (%)
Amplitude = 0.1;                        % Amplitude of the surface [m]
Wavelength = 1;                         % Wavelength of the surface [m]
n = 4;                                  % Total number of layers to evaluate
Total_layers = n;
Hscale = 2/5;                           % Ratio between the height and the length of ...
    the joint
Lscale = 1;                             % Scale factor of the joint length depending ...
    on the slipper length (0 to 1)
nscale = 2;                             % Scale factor of which the length of the ...
    joint increases for each ascending layer (bottom to top)

data_size_slipper = 500;                % Number of iteratations to obtain slipper ...
    length, max slipper length is determined by data_size_slipper/(2*data_size_slipper)
data_size = 1000;                       % Number of datapoints to obtain the ...
    compression for each slipper

%% Initial Matrices
Ls = zeros(1,data_size_slipper);
c = zeros(Total_layers, data_size_slipper);
hj = zeros(Total_layers+2, data_size_slipper);
hb = zeros(Total_layers, data_size_slipper);

Length_slipper_joint = zeros(1,data_size_slipper);
c_joint = zeros(1,data_size_slipper);
h_joint = zeros(1,data_size_slipper);

Length_slipper_no_joint = zeros(1,data_size_slipper);
c_no_joint = zeros(1,data_size_slipper);
h_no_joint = zeros(1,data_size_slipper);

%% Loop
for p = 1:n
    for q = 1:data_size_slipper
        Ls(q) = q/(2*data_size_slipper*2^p);
        for k = 1:p+1
            hj(k+1,q) = hj(k,q)+nscale^(k-1)*Ls(q)*Lscale*Hscale/2;
        end
        c(p,q) = Compression_function(Ls(q), Amplitude, data_size, Wavelength);
        hb(p,q) = c(p,q)/max_strain+hj(p+2,q);
        hj = zeros(p+3,data_size_slipper);
        k = 0;
    end
end

for o = 1:data_size_slipper
    Length_slipper_joint(o) = o/(2 * data_size_slipper);
    c_joint(o) = Compression_function(Length_slipper_joint(o), Amplitude, data_size, ...
        Wavelength);
    h_joint(o) = c_joint(o) / max_strain + Length_slipper_joint(o)*Hscale*Lscale;
    time = (o + Total_layers * data_size_slipper) / (data_size_slipper * ...
        (Total_layers + 2))
end

%% Figures
figure(5)
grid on
hold on

q1 = plot(Length_slipper_joint*100, h_joint*100, 'k:');
q3 = plot(Length_slipper_joint*100, hb(1,:)*100, 'b--');
q4 = plot(Length_slipper_joint*100, hb(2,:)*100, 'r-.');
q5 = plot(Length_slipper_joint*100, hb(3,:)*100, 'k-');
q6 = plot(Length_slipper_joint*100, hb(4,:)*100, 'g-');
```

```

legend([q3 q4 q5 q6 q1], 'Single Layer', 'Double Layer', 'Triple Layer', 'Quadro ...
    Layer', 'Single Slipper', 'Location','northwest')
title(['Total height of bearing'])
xlabel('Lenght of bearing as % of wavelength')
ylabel('Minimum height of bearing as % of wavelength')
axis([0,25,0,10])
```

```
function [y_diff_max] = Compression_function(Length_slipper, Amplitude, n, wavelength)
% Parameter
x = linspace(0, wavelength, n);              % Array of t values from 0 to 2 pi
x_decomposed = zeros(4,n);                   % Array of decomposed t values
Master_file = zeros(2*n,n);                  % Array of all final x and y components
L = Length_slipper*wavelength;
A = Amplitude;
y_diff = zeros(1,n);

% Loop to calculate begin and end points of slipper with corresponding angle
for i = 1:n
    angle = atan(A*cos(x(i)*2*pi)*2*pi);
    x_tot = cos(angle) * L;
    x_decomposed(1,i) = x(i);
    x_decomposed(2,i) = x(i) - x_tot / 2;
    x_decomposed(3,i) = x(i) + x_tot / 2;
    x_decomposed(4,i) = angle;
end

for j = 1:n
    x_new = linspace(x_decomposed(2,j), x_decomposed(3,j), n);
    P = [x_new; A*sin(x_new*2*pi)]; ...
                                                                                ...
        % X and Y coordinates of sine wave corresponding to slipper
    T = [x_decomposed(1,j); A*sin(x_decomposed(1,j)*2*pi)]; ...
                                                        % Translation Matrix to ...
        get to the origin
    R = [cos(x_decomposed(4,j)) sin(x_decomposed(4,j)); -sin(x_decomposed(4,j)) ...
        cos(x_decomposed(4,j))];         % Rotation matrix clockwise around z axis
    P_final = R*(P-T); ...
                                                                                ...
        % Translate and Rotate array P
    Master_file((j-1)*2+1,:) = P_final(1,:);
    Master_file(j*2,:) = P_final(2,:);
end

for k = 1:n
    y_values = Master_file((k*2),:);
    y_diff(k) = abs(max(y_values)-min(y_values));
end

y_diff_max = max(y_diff);
end
```

A.4. Bearing Kinematics

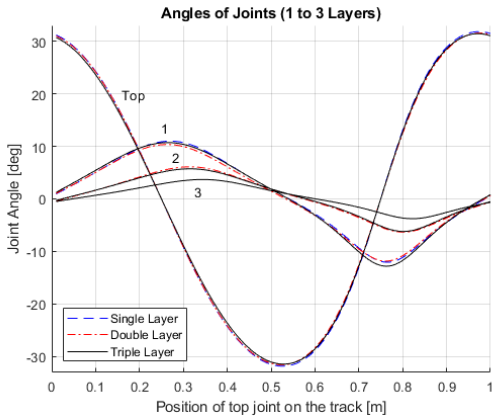

(a) Joint pivot angles of a single, double and triple layer whiffletree compared using the parametric values of the asymmetric whiffletree configuration.

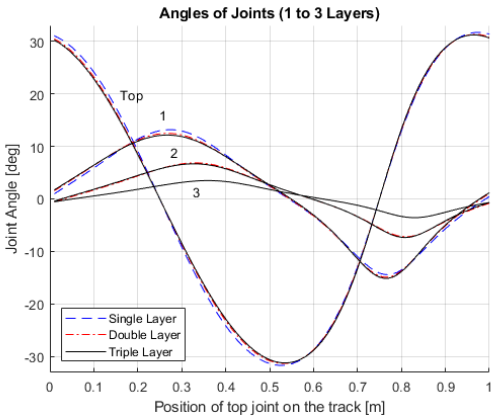

(b) Joint pivot angles of a single, double and triple layer whiffletree compared using the parametric values of the symmetric whiffletree configuration.

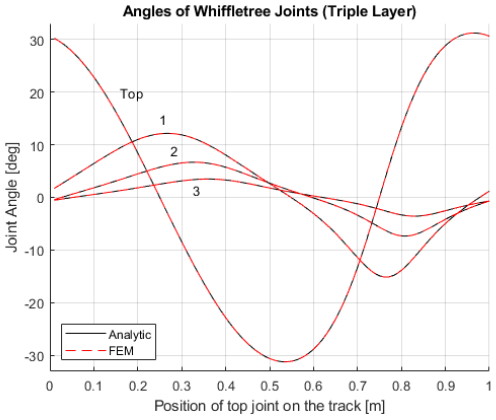

(c) Joint pivot angles of the FEM and analytical model compared for a triple layer whiffletree.

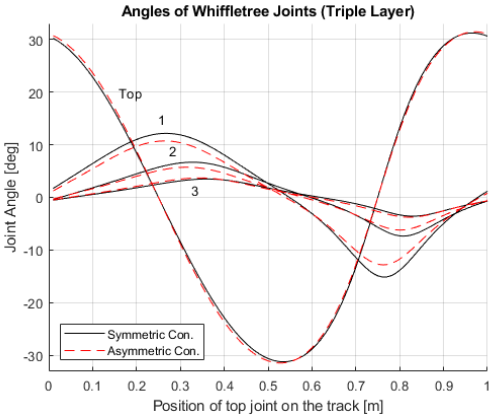

(d) Joint pivot angles of a symmetric and asymmetric triple layer whiffletree configuration.

Figure A.4: Leftmost joint pivot angles of a whiffletree. The line with the highest amplitude corresponds to the top joint noted with Top. Each subsequent line in descending maximum amplitude order, corresponds to the joint one layer below noted with 1, 2 or 3 respectively.

The joint angles in the bearing are obtained using the bearing kinematics described in section 2.2 of the paper. The scrips used to obtain the angles are given in this section. First the main script is given that uses the 3 functions $Layer1\_angles$, $Layer2\_angles$ and $Layer3\_angles$ to obtain the angles of each joint with the horizontal. Then, the pivot angles of each joint is determined. Following, the data obtained from the FEM analysis using Comsol Multiphysics is imported to create 7 different figures. The first figure shows the behavior of the leftmost angle of each layer for a single, double and triple layer whiffletree. The results are obtained for the symmetric slipper configuration, shown in figure A.4b, and the asymmetric slipper configuration, shown in figure A.4a. The next three figures show the comparison between the angles obtained for a single, double and triple layer whiffletree respectively using the analytical model and the finite element model where the comparison of the triple layer whiffletree is shown in figure A.4c. The fifth figure shows the comparison of the joint angles between a triple layer symmetric and asymmetric slipper configuration shown in figure A.4d. The final two plots show the slipper angle using the three different stiffness ratios explained in section 2.3 of the paper. To remake the model, only the script till line 126 is required. The plots obtained from line 196 to 220 and 285 to 308 can be obtained using only the analytical model. For the remaining plots, the results of the finite element model are required.

```
clear all
close all
clc

options=optimset('MaxFunEvals',10000, 'MaxIter', 10000);
%% Variables
data_size = 100;
wavelength_factor = 3/4; %bearing length as function of wavelength
Wavelength = 1;
A = 0.1*Wavelength;

%% 1 Layer
% Initial values
theta10 = [0,0,0,0];
L10 = [1,1]*wavelength_factor*Wavelength/(4);
%L10 = [0.073223304703362   0.051776695296638];
J01 = (L10(1)+L10(2))*1/5;
J10 = [J01, 2*J01];

% Solver
for i = 1:data_size
    x(i) = i/data_size;
        fun = @(theta10)Layer1_angles(x(i), theta10, L10, J10, A);
    psi1(i,:) = fsolve(fun,theta10,options);
end

% Top Joint y position
y1 = psi1(:,4);
y1_translated = y1-(max(y1)-min(y1))/2-min(y1);

% Joint Angles
theta1(:,3) = psi1(:,3);
theta1(:,2) = psi1(:,2)-psi1(:,3);
theta1(:,1) = psi1(:,1)-psi1(:,3);
theta_rotated1 = theta1'*180/pi;

%% 2 Layers
% Initial values
theta20 = [0,0,0,0,0,0,0,0];
L20 = [1,1,1,1]*wavelength_factor*Wavelength/(8);
%L20 = [0.047219468937932   0.031984928889458   0.023189480593374   0.022606121579236];
J02 = (L20(3)+L20(4))*1/5;
J20 = [J02, 2*J02, 4*J02];

% Solver
for i = 1:data_size
    x(i) = i/data_size;
    fun = @(theta20)Layer2_angles(x(i), theta20, L20, J20, A);
    psi2(i,:) = fsolve(fun,theta20,options);
end
% Top Joint y position
y2 = psi2(:,8);
y2_translated = y2-(max(y2)-min(y2))/2-min(y2);

% Joint Angles
theta2(:,7) = psi2(:,7);
theta2(:,6) = psi2(:,6)-psi2(:,7);
theta2(:,5) = psi2(:,5)-psi2(:,7);
theta2(:,4) = psi2(:,4)-psi2(:,6);
theta2(:,3) = psi2(:,3)-psi2(:,6);
theta2(:,2) = psi2(:,2)-psi2(:,5);
theta2(:,1) = psi2(:,1)-psi2(:,5);
theta_rotated2 = theta2'*180/pi;

%% 3 Layers
% Initial values
theta30 = [0,0,0,0,0,0,0,0,0,0,0,0,0,0,0,0];
%L30 = [0.028399775767225   0.019210925665594   0.013818521584328   0.013364669060691 ...
      0.012720668426789   0.012610317072069   0.012449198010836   0.012425924412468];
L30 = [1,1,1,1,1,1,1,1]*wavelength_factor*Wavelength/(16);
```

```
J03 = (L30(7)+L30(8))*1/5;
J30 = [J03, 2*J03, 4*J03, 8*J03];

% Solver
for i = 1:data_size
    x(i) = i/data_size;
    fun = @(theta30)Layer3_angles(x(i), theta30, L30, J30, A);
    psi3(i,:) = fsolve(fun,theta30);
end

% Top Joint y position
y3 = psi3(:,16);
y3_translated = y3-(max(y3)-min(y3))/2-min(y3);

% Joint Angles
theta3(:,15) = psi3(:,15);
theta3(:,14) = psi3(:,14)-psi3(:,15);
theta3(:,13) = psi3(:,13)-psi3(:,15);
theta3(:,12) = psi3(:,12)-psi3(:,14);
theta3(:,11) = psi3(:,11)-psi3(:,14);
theta3(:,10) = psi3(:,10)-psi3(:,13);
theta3(:,9) = psi3(:,9)-psi3(:,13);
theta3(:,8) = psi3(:,8)-psi3(:,12);
theta3(:,7) = psi3(:,7)-psi3(:,12);
theta3(:,6) = psi3(:,6)-psi3(:,11);
theta3(:,5) = psi3(:,5)-psi3(:,11);
theta3(:,4) = psi3(:,4)-psi3(:,10);
theta3(:,3) = psi3(:,3)-psi3(:,10);
theta3(:,2) = psi3(:,2)-psi3(:,9);
theta3(:,1) = psi3(:,1)-psi3(:,9);
theta_rotated3 = theta3'*180/pi;

%% 3 Layers assymetric slipper length
% Initial values
theta31 = [0,0,0,0,0,0,0,0,0,0,0,0,0,0,0,0];
L31 = [0.028399775767225   0.019210925665594   0.013818521584328   0.013364669060691 ...
       0.012720668426789   0.012610317072069   0.012449198010836   0.012425924412468];
J031 = (L31(7)+L31(8))*1/5;
J31 = [J031, 2*J031, 4*J031, 8*J031];

% Solver
for i = 1:data_size
    x(i) = i/data_size;
    fun = @(theta31)Layer3_angles(x(i), theta31, L31, J31, A);
    psi31(i,:) = fsolve(fun,theta31);
end

% Data
theta311(:,15) = psi31(:,15);
theta311(:,14) = psi31(:,14)-psi31(:,15);
theta311(:,13) = psi31(:,13)-psi31(:,15);
theta311(:,12) = psi31(:,12)-psi31(:,14);
theta311(:,11) = psi31(:,11)-psi31(:,14);
theta311(:,10) = psi31(:,10)-psi31(:,13);
theta311(:,9) = psi31(:,9)-psi31(:,13);
theta311(:,8) = psi31(:,8)-psi31(:,12);
theta311(:,7) = psi31(:,7)-psi31(:,12);
theta311(:,6) = psi31(:,6)-psi31(:,11);
theta311(:,5) = psi31(:,5)-psi31(:,11);
theta311(:,4) = psi31(:,4)-psi31(:,10);
theta311(:,3) = psi31(:,3)-psi31(:,10);
theta311(:,2) = psi31(:,2)-psi31(:,9);
theta311(:,1) = psi31(:,1)-psi31(:,9);
theta_rotated31 = theta311'*180/pi;


%% Array of x values
x_values = x;
%% Comsol Data
% Comsol Data 3 layer stiffness slipper
M_3_layer_s_1_10_slip = dlmread('Slip_1_3_layer_s_Comsol_10.txt')';
```

```
Comsol_Slip_3_layer_s_1_10_slip = M_3_layer_s_1_10_slip(2,:)*-1;
M_3_layer_s_1_100_slip = dlmread('Slip_1_3_layer_s_Comsol_100.txt')';
Comsol_Slip_3_layer_s_1_100_slip = M_3_layer_s_1_100_slip(2,:)*-1;
M_3_layer_s_1_1000_slip = dlmread('Slip_1_3_layer_s_Comsol_1000.txt')';
Comsol_Slip_3_layer_s_1_1000_slip = M_3_layer_s_1_1000_slip(2,:)*-1;

% Comsol Data 3 layer stiffness slipper
M_3_layer_s_1_10_slips = dlmread('Slip_1_3_layer_s_Comsol_10_sym.txt')';
Comsol_Slip_3_layer_s_1_10_slips = M_3_layer_s_1_10_slips(2,:)*-1;
M_3_layer_s_1_100_slips = dlmread('Slip_1_3_layer_s_Comsol_100_sym.txt')';
Comsol_Slip_3_layer_s_1_100_slips = M_3_layer_s_1_100_slips(2,:)*-1;
M_3_layer_s_1_1000_slips = dlmread('Slip_1_3_layer_s_Comsol_1000_sym.txt')';
Comsol_Slip_3_layer_s_1_1000_slips = M_3_layer_s_1_1000_slips(2,:)*-1;

% Comsol Data 3 layer stiffness
M_3_layer_j_1_15 = dlmread('Joint_1_3_layer_s_Comsol_15.txt')';
Comsol_joint_3_layer_s_1_15 = M_3_layer_j_1_15(2,:)*-1;
M_3_layer_j_11_15 = dlmread('Joint_11_3_layer_s_Comsol_15.txt')';
Comsol_joint_3_layer_s_11_15 = M_3_layer_j_11_15(2,:)*-1;
M_3_layer_j_21_15 = dlmread('Joint_21_3_layer_s_Comsol_15.txt')';
Comsol_joint_3_layer_s_21_15 = M_3_layer_j_21_15(2,:)*-1;
M_3_layer_j_31_15 = dlmread('Joint_31_3_layer_s_Comsol_15.txt')';
Comsol_joint_3_layer_s_31_15 = M_3_layer_j_31_15(2,:)*-1;

M_3_layer_j_1_100 = dlmread('Joint_1_3_layer_s_Comsol_100.txt')';
Comsol_joint_3_layer_s_1_100 = M_3_layer_j_1_100(2,:)*-1;
M_3_layer_j_11_100 = dlmread('Joint_11_3_layer_s_Comsol_100.txt')';
Comsol_joint_3_layer_s_11_100 = M_3_layer_j_11_100(2,:)*-1;
M_3_layer_j_21_100 = dlmread('Joint_21_3_layer_s_Comsol_100.txt')';
Comsol_joint_3_layer_s_21_100 = M_3_layer_j_21_100(2,:)*-1;
M_3_layer_j_31_100 = dlmread('Joint_31_3_layer_s_Comsol_100.txt')';
Comsol_joint_3_layer_s_31_100 = M_3_layer_j_31_100(2,:)*-1;

M_3_layer_j_1_1000 = dlmread('Joint_1_3_layer_s_Comsol_1000.txt')';
Comsol_joint_3_layer_s_1_1000 = M_3_layer_j_1_1000(2,:)*-1;
M_3_layer_j_11_1000 = dlmread('Joint_11_3_layer_s_Comsol_1000.txt')';
Comsol_joint_3_layer_s_11_1000 = M_3_layer_j_11_1000(2,:)*-1;
M_3_layer_j_21_1000 = dlmread('Joint_21_3_layer_s_Comsol_1000.txt')';
Comsol_joint_3_layer_s_21_1000 = M_3_layer_j_21_1000(2,:)*-1;
M_3_layer_j_31_1000 = dlmread('Joint_31_3_layer_s_Comsol_1000.txt')';
Comsol_joint_3_layer_s_31_1000 = M_3_layer_j_31_1000(2,:)*-1;

% Comsol Data 3 layer
M_3_layer_1 = dlmread('Joint_1_3_layer_Comsol.txt')';
Comsol_Joint_3_layer_1 = M_3_layer_1(2,:)*-1;
M_3_layer_11 = dlmread('Joint_11_3_layer_Comsol.txt')';
Comsol_Joint_3_layer_11 = M_3_layer_11(2,:)*-1;
M_3_layer_21 = dlmread('Joint_21_3_layer_Comsol.txt')';
Comsol_Joint_3_layer_21 = M_3_layer_21(2,:)*-1;
M_3_layer_31 = dlmread('Joint_31_3_layer_Comsol.txt')';
Comsol_Joint_3_layer_31 = M_3_layer_31(2,:)*-1;

% Comsol Data 2 layer
M_2_layer_1 = dlmread('Joint_1_2_layer_Comsol.txt')';
Comsol_Joint_2_layer_1 = M_2_layer_1(2,:)*-1;
M_2_layer_11 = dlmread('Joint_11_2_layer_Comsol.txt')';
Comsol_Joint_2_layer_11 = M_2_layer_11(2,:)*-1;
M_2_layer_21 = dlmread('Joint_21_2_layer_Comsol.txt')';
Comsol_Joint_2_layer_21 = M_2_layer_21(2,:)*-1;

% Comsol Data 1 layer
M_1_layer_1 = dlmread('Joint_1_1_layer_Comsol.txt')';
Comsol_Joint_1_layer_1 = M_1_layer_1(2,:)*-1;
M_1_layer_11 = dlmread('Joint_11_1_layer_Comsol.txt')';
Comsol_Joint_1_layer_11 = M_1_layer_11(2,:)*-1;

%% Plot Matlab all layers
figure(1)
hold on
grid on
p11 = plot(x_values,theta_rotated1(3,:),'b--','LineWidth',3);
```

```
p13 = plot(x_values,theta_rotated1(1,:),'b--','LineWidth',3);

p21 = plot(x_values,theta_rotated2(7,:),'r-.','LineWidth',3);
p23 = plot(x_values,theta_rotated2(5,:),'r-.','LineWidth',3);
p27 = plot(x_values,theta_rotated2(1,:),'r-.','LineWidth',3);

p31 = plot(x_values,theta_rotated3(15,:),'k-','LineWidth',3);
p33 = plot(x_values,theta_rotated3(13,:),'k-','LineWidth',3);
p37 = plot(x_values,theta_rotated3(9,:),'k-','LineWidth',3);
p38 = plot(x_values,theta_rotated3(1,:),'k-','LineWidth',3);

legend([p11 p21 p31],'Single Layer', 'Double Layer', 'Triple Layer', 'Location', ...
    'southwest')
title(['Angles of Joints (1 to 3 Layer Whiffletree)'])
xlabel('Position of top joint on the track [m]')
ylabel('Joint Angle [deg]')
axis([0,1,-33,33])
text(0.16,20,'Top')
text(0.25,13.5,'1')
text(0.275,8,'2')
text(0.325,1.5,'3')

%% Plot Comsol vs Matlab 1 Layer
figure(2)
hold on
grid on
q11 = plot(x_values,theta_rotated1(3,:),'k-');
q13 = plot(x_values,theta_rotated1(1,:),'k-');

q111 = plot(x_values,Comsol_Joint_1_layer_11,'r--');
q113 = plot(x_values,Comsol_Joint_1_layer_1,'r--');

title(['Angles of Whiffletree Joints (Single Layer Whiffletree)'])
xlabel('Position of top joint on the track [m]')
ylabel('Joint Angle [deg]')
axis([0,1,-33,33])
legend([q11 q111],'Analytic', 'FEM', 'Location', 'southwest')
text(0.16,20,'Top')
text(0.25,16,'1')

%% Plot Comsol vs Matlab 2 Layer
figure(3)
hold on
grid on
q21 = plot(x_values,theta_rotated2(7,:),'k-');
q23 = plot(x_values,theta_rotated2(5,:),'k-');
q27 = plot(x_values,theta_rotated2(1,:),'k-');

q211 = plot(x_values,Comsol_Joint_2_layer_21,'r--');
q213 = plot(x_values,Comsol_Joint_2_layer_11,'r--');
q217 = plot(x_values,Comsol_Joint_2_layer_1,'r--');

title(['Angles of Whiffletree Joints (Double Layer Whiffletree)'])
xlabel('Position of top joint on the track [m]')
ylabel('Joint Angle [deg]')
axis([0,1,-33,33])
legend([q21 q211],'Analytic', 'FEM', 'Location', 'southwest')
text(0.16,20,'Top')
text(0.25,15,'1')
text(0.275,9,'2')

%% Plot Comsol vs Matlab 3 Layer
figure(4)
hold on
grid on
q31 = plot(x_values,theta_rotated3(15,:),'k-');
q33 = plot(x_values,theta_rotated3(13,:),'k-');
q37 = plot(x_values,theta_rotated3(9,:),'k-');
q315 = plot(x_values,theta_rotated3(1,:),'k-');

q321 = plot(x_values,Comsol_Joint_3_layer_31,'r--');
```

```
q323 = plot(x_values,Comsol_Joint_3_layer_21,'r--');
q327 = plot(x_values,Comsol_Joint_3_layer_11,'r--');
q3215 = plot(x_values,Comsol_Joint_3_layer_1,'r--');

title(['Angles of Whiffletree Joints (Triple Layer Whiffletree)'])
xlabel('Position of top joint on the track [m]')
ylabel('Joint Angle [deg]')
axis([0,1,-33,33])
legend([q31 q321],'Analytic', 'FEM', 'Location', 'southwest')
text(0.16,20,'Top')
text(0.25,15,'1')
text(0.275,9,'2')
text(0.325,1.5,'3')

%% Plot 3 layer symmetric and asymmetric slipper length
figure(5)
hold on
grid on
q41 = plot(x_values,theta_rotated3(15,:),'k-');
q42 = plot(x_values,theta_rotated3(13,:),'k-');
q43 = plot(x_values,theta_rotated3(9,:),'k-');
q44 = plot(x_values,theta_rotated3(1,:),'k-');

q51 = plot(x_values,theta_rotated31(15,:),'r--');
q52 = plot(x_values,theta_rotated31(13,:),'r--');
q53 = plot(x_values,theta_rotated31(9,:),'r--');
q54 = plot(x_values,theta_rotated31(1,:),'r--');

title(['Angles of Whiffletree Joints (Triple Layer Whiffletree)'])
xlabel('Position of top joint on the track [m]')
ylabel('Joint Angle [deg]')
axis([0,1,-33,33])
legend([q41 q51],'Non-coupled Config.', 'Coupled Config.', 'Location', 'southwest')
text(0.16,20,'Top')
text(0.25,15,'1')
text(0.275,9,'2')
text(0.325,1.5,'3')

%% Plot 3 layer whiffletree with stiffness slippers symmetric
figure(6)
hold on
grid on
q81 = plot(x_values,Comsol_Slip_3_layer_s_1_10_slip,'k-');
q82 = plot(x_values,Comsol_Slip_3_layer_s_1_100_slip,'r--');
q83 = plot(x_values,Comsol_Slip_3_layer_s_1_1000_slip,'b-.');

title(['Angle of Slipper (Triple Layer Whiffletree)'])
xlabel('Position of top joint on the track [m]')
ylabel('Slipper Angle [deg]')
axis([0,1,-0.5,0.5])
legend([q81 q82 q83],'k_s = 10k_j', 'k_s = 100k_j', 'k_s = 1000k_j', 'Location', ...
    'northeast')

%% Plot 3 layer whiffletree with stiffness slippers asymmetric
figure(7)
hold on
grid on
q101 = plot(x_values,Comsol_Slip_3_layer_s_1_10_slips,'k-');
q102 = plot(x_values,Comsol_Slip_3_layer_s_1_100_slips,'r--');
q103 = plot(x_values,Comsol_Slip_3_layer_s_1_1000_slips,'b-.');

title(['Angle of Slipper (Asymmetric Slipper Conf.)'])
xlabel('Position of top joint on the track [m]')
ylabel('Slipper Angle [deg]')
axis([0,1,-0.5,0.5])
legend([q101 q102 q103],'k_s = 10k_j', 'k_s = 100k_j', 'k_s = 1000k_j', 'Location', ...
    'northeast')

%% Plot 3 layer all anggles
figure(8)
hold on
```

```
grid on
f1 = plot(x_values,theta_rotated31(1,:),'k-');
f2 = plot(x_values,theta_rotated31(2,:),'k--');
f3 = plot(x_values,theta_rotated31(3,:),'k-');
f4 = plot(x_values,theta_rotated31(4,:),'k--');
f5 = plot(x_values,theta_rotated31(5,:),'k-');
f6 = plot(x_values,theta_rotated31(6,:),'k--');
f7 = plot(x_values,theta_rotated31(7,:),'k-');
f8 = plot(x_values,theta_rotated31(8,:),'k--');
f9 = plot(x_values,theta_rotated31(9,:),'b-');
f10 = plot(x_values,theta_rotated31(10,:),'b--');
f11 = plot(x_values,theta_rotated31(11,:),'b-');
f12 = plot(x_values,theta_rotated31(12,:),'b--');
f13 = plot(x_values,theta_rotated31(13,:),'r-');
f14 = plot(x_values,theta_rotated31(14,:),'r--');
f15 = plot(x_values,theta_rotated31(15,:),'g-');




legend([f1, f9, f13, f15],'Layer 1', 'Layer 2', 'Layer 3', 'Layer Top', 'Location', ...
    'southwest')
title(['Angles of Joints (Triple Layer Whiffletree)'])
xlabel('Position of top joint on the track [m]')
ylabel('Joint Angle [deg]')
axis([0,1,-33,33])

%% Plot 3 layer Path top joint
figure(9)
hold on
grid on
top1 = plot(x_values,y1_translated, 'b--');
top2 = plot(x_values,y2_translated, 'r-.');
top3 = plot(x_values,y3_translated, 'k-');
top4 = plot(x_values,A*sin(x_values*2*pi), 'g-');

legend([top1 top2 top3 top4], 'Single Layer', 'Double Layer', 'Tripple Layer', ...
    'Track', 'Location', 'southwest')
title(['Top Joint Position'])
xlabel('x-position of top joint [m]')
ylabel('y-position of top joint [m]')
axis([0,1,-0.18,0.18])

%% Plot 3 layer Path top joint 2
figure(10)
hold on
grid on
top1 = plot(x_values,y1-y1(1)+A*sin(0.01*2*pi), 'b--');
top2 = plot(x_values,y2-y2(1)+A*sin(0.01*2*pi), 'r-.');
top3 = plot(x_values,y3-y3(1)+A*sin(0.01*2*pi), 'k-');
top4 = plot(x_values,A*sin(x_values*2*pi), 'g-');

legend([top1 top2 top3 top4], 'Single Layer', 'Double Layer', 'Tripple Layer', ...
    'Track', 'Location', 'southwest')
title(['Top Joint Position'])
xlabel('x-position of top joint [m]')
ylabel('y-position of top joint [m]')
axis([0,1,-0.18,0.18])

%% Plot 3 layer Path top joint 3
figure(11)
hold on
grid on
top1 = plot(x_values,y1, 'b--');
top2 = plot(x_values,y2, 'r-.');
top3 = plot(x_values,y3, 'k-');
top4 = plot(x_values,A*sin(x_values*2*pi), 'g-');

legend([top1 top2 top3 top4], 'Single Layer', 'Double Layer', 'Tripple Layer', ...
    'Track', 'Location', 'southwest')
title(['Top Joint Position'])
```

```
xlabel('x-position of top joint [m]')
ylabel('y-position of top joint [m]')
axis([0,1,-0.18,0.18])
```

The functional scrips $Layer1\_angles$, $Layer2\_angles$ and $Layer3\_angles$ are, respectively, given by:

```
function F = Layer1_angles(x_start, theta, L, J, A)
% Slipper Lengths (L) and Joint Heights (J)
L1A = L(1);
L1B = L(2);
L2A = L(2);
L2B = L(1);

J1 = J(1)/2;
J2 = J(2)/2;

% Linkage lengths (d)
d1 = L1B + L2A;

%% Geometry

x11 = x_start;
y11 = theta(4);

x1 = x11+(J2+J1)*sin(theta(3))-1/2*d1*cos(theta(3));
y1 = y11-(J2+J1)*cos(theta(3))-1/2*d1*sin(theta(3));
x2 = x11+(J2+J1)*sin(theta(3))+1/2*d1*cos(theta(3));
y2 = y11-(J2+J1)*cos(theta(3))+1/2*d1*sin(theta(3));

xp1 = x1+J1*sin(theta(1));
yp1 = y1-J1*cos(theta(1));

xp2 = x2+J1*sin(theta(2));
yp2 = y2-J1*cos(theta(2));

%% Functions
F(1) = A*sin(2*pi*xp1)-yp1;
F(2) = atan(A*2*pi*cos(2*pi*xp1))-theta(1);
F(3) = A*sin(2*pi*xp2)-yp2;
F(4) = atan(A*2*pi*cos(2*pi*xp2))-theta(2);
```

```
function F = Layer2_angles(x_start,theta, L, J, A)
% Slipper Lengths (L) and Joint Heights (J)
L1A = L(1);
L1B = L(2);
L2A = L(3);
L2B = L(4);
L3A = L(4);
L3B = L(3);
L4A = L(2);
L4B = L(1);

J1 = J(1)/2;
J2 = J(2)/2;
J3 = J(3)/2;

% Linkage lengths (d)
d11 = L1B + L2A;
d12 = L3B + L4A;
d2 = L2B+L3A+(d11+d12)/2;

%% Geometry
x21 = x_start;

x11 = x21-1/2*d2*cos(theta(7))+(J2+J3)*sin(theta(7));
x12 = x21+1/2*d2*cos(theta(7))+(J2+J3)*sin(theta(7));

x1 = x11-1/2*d11*cos(theta(5))+(J2+J1)*sin(theta(5));
```

```
x2 = x11+1/2*d11*cos(theta(5))+(J2+J1)*sin(theta(5));
x3 = x12-1/2*d12*cos(theta(6))+(J2+J1)*sin(theta(6));
x4 = x12+1/2*d12*cos(theta(6))+(J2+J1)*sin(theta(6));

xp1 = x1+J1*sin(theta(1));
xp2 = x2+J1*sin(theta(2));
xp3 = x3+J1*sin(theta(3));
xp4 = x4+J1*sin(theta(4));


y21 = theta(8);

y11 = y21-1/2*d2*sin(theta(7))-(J2+J3)*cos(theta(7));
y12 = y21+1/2*d2*sin(theta(7))-(J2+J3)*cos(theta(7));

y1 = y11-1/2*d11*sin(theta(5))-(J2+J1)*cos(theta(5));
y2 = y11+1/2*d11*sin(theta(5))-(J2+J1)*cos(theta(5));
y3 = y12-1/2*d12*sin(theta(6))-(J2+J1)*cos(theta(6));
y4 = y12+1/2*d12*sin(theta(6))-(J2+J1)*cos(theta(6));

yp1 = y1-J1*cos(theta(1));
yp2 = y2-J1*cos(theta(2));
yp3 = y3-J1*cos(theta(3));
yp4 = y4-J1*cos(theta(4));

%% Functions
F(1) = A*sin(xp1*2*pi)-yp1;
F(2) = atan(A*2*pi*cos(2*pi*xp1))-theta(1);
F(3) = A*sin(xp2*2*pi)-yp2;
F(4) = atan(A*2*pi*cos(2*pi*xp2))-theta(2);
F(5) = A*sin(xp3*2*pi)-yp3;
F(6) = atan(A*2*pi*cos(2*pi*xp3))-theta(3);
F(7) = A*sin(xp4*2*pi)-yp4;
F(8) = atan(A*2*pi*cos(2*pi*xp4))-theta(4);

end
```

```
function F = Layer3_angles(x_start,theta, L, J, A)
% Slipper Lengths (L) and Joint Heights (J)
L1A = L(1);
L1B = L(2);
L2A = L(3);
L2B = L(4);
L3A = L(5);
L3B = L(6);
L4A = L(7);
L4B = L(8);
L5A = L(8);
L5B = L(7);
L6A = L(6);
L6B = L(5);
L7A = L(4);
L7B = L(3);
L8A = L(2);
L8B = L(1);

J1 = J(1)/2;
J2 = J(2)/2;
J3 = J(3)/2;
J4 = J(4)/2;

% Linkage lengths (d)
d11 = L1B + L2A;
d12 = L3B + L4A;
d13 = L5B + L6A;
d14 = L7B + L8A;
d21 = L2B+L3A+(d11+d12)/2;
d22 = L2B+L3A+(d11+d12)/2;
d3 = (L4B+d12/2+d21/2)*2;
```

```
33
34
35 %% Geometry
36 x31 = x_start;
37
38 x21 = x31-1/2*d3*cos(theta(15))+(J3+J4)*sin(theta(15));
39 x22 = x31+1/2*d3*cos(theta(15))+(J3+J4)*sin(theta(15));
40
41 x11 = x21-1/2*d21*cos(theta(13))+(J2+J3)*sin(theta(13));
42 x12 = x21+1/2*d21*cos(theta(13))+(J2+J3)*sin(theta(13));
43 x13 = x22-1/2*d22*cos(theta(14))+(J2+J3)*sin(theta(14));
44 x14 = x22+1/2*d22*cos(theta(14))+(J2+J3)*sin(theta(14));
45
46 x1 = x11-1/2*d11*cos(theta(9))+(J2+J1)*sin(theta(9));
47 x2 = x11+1/2*d11*cos(theta(9))+(J2+J1)*sin(theta(9));
48 x3 = x12-1/2*d12*cos(theta(10))+(J2+J1)*sin(theta(10));
49 x4 = x12+1/2*d12*cos(theta(10))+(J2+J1)*sin(theta(10));
50 x5 = x13-1/2*d13*cos(theta(11))+(J2+J1)*sin(theta(11));
51 x6 = x13+1/2*d13*cos(theta(11))+(J2+J1)*sin(theta(11));
52 x7 = x14-1/2*d14*cos(theta(12))+(J2+J1)*sin(theta(12));
53 x8 = x14+1/2*d14*cos(theta(12))+(J2+J1)*sin(theta(12));
54
55 xp1 = x1+J1*sin(theta(1));
56 xp2 = x2+J1*sin(theta(2));
57 xp3 = x3+J1*sin(theta(3));
58 xp4 = x4+J1*sin(theta(4));
59 xp5 = x5+J1*sin(theta(5));
60 xp6 = x6+J1*sin(theta(6));
61 xp7 = x7+J1*sin(theta(7));
62 xp8 = x8+J1*sin(theta(8));
63
64 y31 = theta(16);
65
66 y21 = y31-1/2*d3*sin(theta(15))-(J3+J4)*cos(theta(15));
67 y22 = y31+1/2*d3*sin(theta(15))-(J3+J4)*cos(theta(15));
68
69 y11 = y21-1/2*d21*sin(theta(13))-(J2+J3)*cos(theta(13));
70 y12 = y21+1/2*d21*sin(theta(13))-(J2+J3)*cos(theta(13));
71 y13 = y22-1/2*d22*sin(theta(14))-(J2+J3)*cos(theta(14));
72 y14 = y22+1/2*d22*sin(theta(14))-(J2+J3)*cos(theta(14));
73
74 y1 = y11-1/2*d11*sin(theta(9))-(J2+J1)*cos(theta(9));
75 y2 = y11+1/2*d11*sin(theta(9))-(J2+J1)*cos(theta(9));
76 y3 = y12-1/2*d12*sin(theta(10))-(J2+J1)*cos(theta(10));
77 y4 = y12+1/2*d12*sin(theta(10))-(J2+J1)*cos(theta(10));
78 y5 = y13-1/2*d13*sin(theta(11))-(J2+J1)*cos(theta(11));
79 y6 = y13+1/2*d13*sin(theta(11))-(J2+J1)*cos(theta(11));
80 y7 = y14-1/2*d14*sin(theta(12))-(J2+J1)*cos(theta(12));
81 y8 = y14+1/2*d14*sin(theta(12))-(J2+J1)*cos(theta(12));
82
83 yp1 = y1-J1*cos(theta(1));
84 yp2 = y2-J1*cos(theta(2));
85 yp3 = y3-J1*cos(theta(3));
86 yp4 = y4-J1*cos(theta(4));
87 yp5 = y5-J1*cos(theta(5));
88 yp6 = y6-J1*cos(theta(6));
89 yp7 = y7-J1*cos(theta(7));
90 yp8 = y8-J1*cos(theta(8));
91
92 %% Functions
93 F(1) = A*sin(2*pi*xp1)-yp1;
94 F(2) = atan(A*2*pi*cos(2*pi*xp1))-theta(1);
95 F(3) = A*sin(2*pi*xp2)-yp2;
96 F(4) = atan(A*2*pi*cos(2*pi*xp2))-theta(2);
97 F(5) = A*sin(2*pi*xp3)-yp3;
98 F(6) = atan(A*2*pi*cos(2*pi*xp3))-theta(3);
99 F(7) = A*sin(2*pi*xp4)-yp4;
100 F(8) = atan(A*2*pi*cos(2*pi*xp4))-theta(4);
101 F(9) = A*sin(2*pi*xp5)-yp5;
102 F(10) = atan(A*2*pi*cos(2*pi*xp5))-theta(5);
103 F(11) = A*sin(2*pi*xp6)-yp6;
```

```
104 F(12) = atan(A*2*pi*cos(2*pi*xp6))-theta(6);
105 F(13) = A*sin(2*pi*xp7)-yp7;
106 F(14) = atan(A*2*pi*cos(2*pi*xp7))-theta(7);
107 F(15) = A*sin(2*pi*xp8)-yp8;
108 F(16) = atan(A*2*pi*cos(2*pi*xp8))-theta(8);
109 end
```

A.5. Load Capacity

The load capacity is obtained following the equations of section 2.3.1 from the paper. To obtain the pressure profile, load capacity and momentary rotation points 2 scripts are provided. The first script is used to obtain the slipper lengths while the second script can be used to evaluate perturbations in the film height. To solve the system of equations, a numerical solver is used to prevent long calculation times compared to an analytical solving approach.
The first script to obtain the slipper lengths is given by:

```
clear all
close all
clc

options=optimset('MaxFunEvals',1000000, 'MaxIter', 1000000, 'TolFun', 1e-8);
%% Parameters
Ps = 0.5*10^5;
P0 = 0*10^5;
hfactor = 2/5;
dr = 1*10^(-3);
eta = 8.9*10^(-4);
Wavelength = 1;
Ltot = Wavelength/8;

h = [1,1,1,1]*100*10^(-6);

%% 3 Layers
x = ...
    [10^5,10^5,10^5,10^5,10^5,10^5,10^5,0.0156,0.0156,0.0156,0.0156,0.0156,0.0156,0.0156,0.0156];

fun = @(x)Layer3_pressure_profile_numeric(Ps, P0, dr, eta, h, x, Ltot, hfactor);
Results3 = fsolve(fun,x,options);

% Results Solver
P3 = Results3(1:7);
Lslip3 = Results3(8:15);
Lcum = [sum(Results3(8)), sum(Results3(8:9)), sum(Results3(8:10)), ...
    sum(Results3(8:11)), sum(Results3(8:12)), sum(Results3(8:13)), ...
    sum(Results3(8:14)), sum(Results3(8:15))];

% Load capacity
LC3(1) = 1/2*(P3(1)+P0)*Lslip3(1);
LC3(2) = 1/2*(P3(2)+P3(1))*Lslip3(2);
LC3(3) = 1/2*(P3(3)+P3(2))*Lslip3(3);
LC3(4) = 1/2*(P3(4)+P3(3))*Lslip3(4);
LC3(5) = 1/2*(P3(5)+P3(4))*Lslip3(5);
LC3(6) = 1/2*(P3(6)+P3(5))*Lslip3(6);
LC3(7) = 1/2*(P3(7)+P3(6))*Lslip3(7);
LC3(8) = 1/2*(P3(7)+P3(7))*Lslip3(8);

M3(1) = LC3(1)*Lslip3(1);
M3(2) = LC3(2)*Lslip3(2);
M3(3) = LC3(3)*Lslip3(3);
M3(4) = LC3(4)*Lslip3(4);
M3(5) = LC3(5)*Lslip3(5);
M3(6) = LC3(6)*Lslip3(6);
M3(7) = LC3(7)*Lslip3(7);
M3(8) = LC3(8)*Lslip3(8);

%% 2 Layers
x = [10^5,10^5,10^5,0.0156,0.0156,0.0156,0.0156];

fun = @(x)Layer2_pressure_profile_numeric(Ps, P0, dr, eta, h, x, Ltot, hfactor);
Results2 = fsolve(fun,x,options);

% Results Solver
P2 = Results2(1:3);
Lslip2 = Results2(4:7);

% Load capacity
```

```
LC2(1) = 1/2*(P2(1)+P0)*Lslip2(1);
LC2(2) = 1/2*(P2(2)+P2(1))*Lslip2(2);
LC2(3) = 1/2*(P2(3)+P2(2))*Lslip2(3);
LC2(4) = 1/2*(P2(3)+P2(3))*Lslip2(4);

M2(1) = LC2(1)*Lslip2(1);
M2(2) = LC2(2)*Lslip2(2);
M2(3) = LC2(3)*Lslip2(3);
M2(4) = LC2(4)*Lslip2(4);

%% 1 Layer
x = [10^5,0.0156,0.0156];

fun = @(x)Layer1_pressure_profile_numeric(Ps, P0, dr, eta, h, x, Ltot, hfactor);
Results1 = fsolve(fun,x,options);

% Results Solver
P1 = Results1(1);
Lslip1 = Results1(2:3);

% Load capacity
LC1(1) = 1/2*(P1(1)+P0)*Lslip1(1);
LC1(2) = 1/2*(P1(1)+P1(1))*Lslip1(2);

M1(1) = LC1(1)*Lslip1(1);
M1(2) = LC1(2)*Lslip1(2);

%% Figures
figure(1)
hold on
grid on
q31 = plot([0, Lslip3(1)], [P0,P3(1)],'k-');
q32 = plot([Lcum(1), Lcum(2)], [P3(1),P3(2)],'k-');
q33 = plot([Lcum(2), Lcum(3)], [P3(2),P3(3)],'k-');
q34 = plot([Lcum(3), Lcum(4)], [P3(3),P3(4)],'k-');
q35 = plot([Lcum(4), Lcum(5)], [P3(4),P3(5)],'k-');
q36 = plot([Lcum(5), Lcum(6)], [P3(5),P3(6)],'k-');
q37 = plot([Lcum(6), Lcum(7)], [P3(6),P3(7)],'k-');
q38 = plot([Lcum(7), Lcum(8)], [P3(7),P3(7)],'k-');

title(['Pressure Profile of 3 Layer Whiffletree'])
xlabel('Position on bearing [m]')
ylabel('Pressure [Pa]')
axis([0,Lcum(end)+0.005,P0,P3(end)+0.5*10^4])
legend([q31],'Analytic', 'Location', 'southeast')
```

With the function *Layer*3*_pressure_profile_numeric*, *Layer*2*_pressure_profile_numeric* and *Layer*1*_pressure_profile_numeric* given as, respectively:

```
function F = Layer3_pressure_profile_numeric(Ps, P0, dr, eta, h, x, Ltot, hfactor)

P(1) = x(1);
P(2) = x(2);
P(3) = x(3);
P(4) = x(4);
P(5) = x(5);
P(6) = x(6);
P(7) = x(7);

L(1) = x(8);
L(2) = x(9);
L(3) = x(10);
L(4) = x(11);
L(5) = x(12);
L(6) = x(13);
L(7) = x(14);
L(8) = x(15);

Lr = (L(7)+L(8))*hfactor*0.5;
```

```
21
22 Gs = pi*dr^4/(Lr*128*eta);
23
24 Q(1) = h(1)^3/(12*eta)*(P(1)-P0)/(L(1));
25 Q(2) = h(1)^3/(12*eta)*(P(2)-P(1))/(L(2));
26 Q(3) = h(2)^3/(12*eta)*(P(3)-P(2))/(L(3));
27 Q(4) = h(2)^3/(12*eta)*(P(4)-P(3))/(L(4));
28 Q(5) = h(3)^3/(12*eta)*(P(5)-P(4))/(L(5));
29 Q(6) = h(3)^3/(12*eta)*(P(6)-P(5))/(L(6));
30 Q(7) = h(4)^3/(12*eta)*(P(7)-P(6))/(L(7));
31
32 Q_inlet(1) = Gs*(Ps-P(1));
33 Q_inlet(2) = Gs*(Ps-P(3));
34 Q_inlet(3) = Gs*(Ps-P(5));
35 Q_inlet(4) = Gs*(Ps-P(7));
36
37 LC(1) = 1/2*(P(1)+P0)*L(1);
38 LC(2) = 1/2*(P(2)+P(1))*L(2);
39 LC(3) = 1/2*(P(3)+P(2))*L(3);
40 LC(4) = 1/2*(P(4)+P(3))*L(4);
41 LC(5) = 1/2*(P(5)+P(4))*L(5);
42 LC(6) = 1/2*(P(6)+P(5))*L(6);
43 LC(7) = 1/2*(P(7)+P(6))*L(7);
44 LC(8) = 1/2*(P(7)+P(7))*L(8);
45
46
47 M(1) = LC(1)*L(1)/2;
48 M(2) = LC(2)*L(2)/2;
49 M(3) = LC(3)*L(3)/2;
50 M(4) = LC(4)*L(4)/2;
51 M(5) = LC(5)*L(5)/2;
52 M(6) = LC(6)*L(6)/2;
53 M(7) = LC(7)*L(7)/2;
54 M(8) = LC(8)*L(8)/2;
55
56 F(1) = Q(7)-Q_inlet(4);
57 F(2) = Q(5)-Q(6)-Q_inlet(3);
58 F(3) = Q(3)-Q(4)-Q_inlet(2);
59 F(4) = Q(1)-Q(2)-Q_inlet(1);
60 F(5) = Q(3)-Q(2);
61 F(6) = Q(5)-Q(4);
62 F(7) = Q(7)-Q(6);
63 F(8) = M(1)-M(2);
64 F(9) = M(3)-M(4);
65 F(10) = M(5)-M(6);
66 F(11) = M(7)-M(8);
67 F(12) = LC(1)+LC(2)-LC(3)-LC(4);
68 F(13) = LC(3)+LC(4)-LC(5)-LC(6);
69 F(14) = LC(5)+LC(6)-LC(7)-LC(8);
70 F(15) = L(1)+L(2)+L(3)+L(4)+L(5)+L(6)+L(7)+L(8)-Ltot;
71 end
```

```
1  function F = Layer2_pressure_profile_numeric(Ps, P0, dr, eta, h, x, Ltot, hfactor)
2
3  P(1) = x(1);
4  P(2) = x(2);
5  P(3) = x(3);
6
7  L(1) = x(4);
8  L(2) = x(5);
9  L(3) = x(6);
10 L(4) = x(7);
11
12
13 Lr = (L(3)+L(4))*hfactor*0.5;
14
15 Gs = pi*dr^4/(Lr*128*eta);
16
17 Q(1) = h(1)^3/(12*eta)*(P(1)-P0)/(L(1));
```

```
Q(2) = h(1)^3/(12*eta)*(P(2)-P(1))/(L(2));
Q(3) = h(2)^3/(12*eta)*(P(3)-P(2))/(L(3));



Q_inlet(1) = Gs*(Ps-P(1));
Q_inlet(2) = Gs*(Ps-P(3));


LC(1) = 1/2*(P(1)+P0)*L(1);
LC(2) = 1/2*(P(2)+P(1))*L(2);
LC(3) = 1/2*(P(3)+P(2))*L(3);
LC(4) = 1/2*(P(3)+P(3))*L(4);


M(1) = LC(1)*L(1)/2;
M(2) = LC(2)*L(2)/2;
M(3) = LC(3)*L(3)/2;
M(4) = LC(4)*L(4)/2;


F(1) = Q(3)-Q_inlet(2);
F(2) = Q(1)-Q(2)-Q_inlet(1);
F(3) = Q(3)-Q(2);
F(4) = M(1)-M(2);
F(5) = M(3)-M(4);
F(6) = LC(1)+LC(2)-LC(3)-LC(4);
F(7) = L(1)+L(2)+L(3)+L(4)-Ltot;
end
```

```
function F = Layer1_pressure_profile_numeric(Ps, P0, dr, eta, h, x, Ltot, hfactor)

P(1) = x(1);
L(1) = x(2);
L(2) = x(3);

Lr = (L(1)+L(2))*hfactor*0.5;

Gs = pi*dr^4/(Lr*128*eta);

Q(1) = h(1)^3/(12*eta)*(P(1)-P0)/(L(1));

Q_inlet(1) = Gs*(Ps-P(1));

LC(1) = 1/2*(P(1)+P0)*L(1);
LC(2) = 1/2*(P(1)+P(1))*L(2);

M(1) = LC(1)*L(1)/2;
M(2) = LC(2)*L(2)/2;

F(1) = Q(1)-Q_inlet(1);
F(2) = M(1)-M(2);
F(3) = L(1)+L(2)-Ltot;
end
```

The second script is given by:

```
clear all
close all
clc

options=optimset('MaxFunEvals',1000000, 'MaxIter', 1000000, 'TolFun', 1e-20);


%% Variables
Ps = 0.5*10^5;
P0 = 0;
dr = 0.5*10^(-3);
hfactor = 2/5;
eta = 8.9*10^(-4);

%% Triple Layer
P_initial = [0.5,1,0.5,1,0.5,1,1]*10^5;
Lslip = [0.028399775767225   0.019210925665594   0.013818521584328   ...
    0.013364669060691   0.012720668426789   0.012610317072069   0.012449198010836   ...
    0.012425924412468];
h = [0.5,1,1,0.5,1,0.5,0.5,1]*100*10^(-6);

fun = @(P_initial)Layer3_pressure_profile(Ps, P0, h, dr, eta, Lslip, P_initial, hfactor);
P = fsolve(fun,P_initial,options);


LC(1) = 1/2*(P(1)+P0)*Lslip(1);
LC(2) = 1/2*(P(2)+P(1))*Lslip(2);
LC(3) = 1/2*(P(3)+P(2))*Lslip(3);
LC(4) = 1/2*(P(4)+P(3))*Lslip(4);
LC(5) = 1/2*(P(5)+P(4))*Lslip(5);
LC(6) = 1/2*(P(6)+P(5))*Lslip(6);
LC(7) = 1/2*(P(7)+P(6))*Lslip(7);
LC(8) = 1/2*(P(7)+P(7))*Lslip(8);

Load_Capacity(1) = LC(1)+LC(2);
Load_Capacity(2) = LC(3)+LC(4);
Load_Capacity(3) = LC(5)+LC(6);
Load_Capacity(4) = LC(7)+LC(8);


M(1) = LC(1)*Lslip(1)-LC(2)*Lslip(2);
M(2) = LC(3)*Lslip(3)-LC(4)*Lslip(4);
M(3) = LC(5)*Lslip(5)-LC(6)*Lslip(6);
M(4) = LC(7)*Lslip(7)-LC(8)*Lslip(8);


L(1) = Lslip(1) + Lslip(2);
L(2) = Lslip(3) + Lslip(4);
L(3) = Lslip(5) + Lslip(6);
L(4) = Lslip(7) + Lslip(8);

%% Double Layer

%% Results
P
LC
M
L
Ltot= sum(L)
J = L(4)*2/5*0.5
%% End effector stiffness
```

With the function $Layer3\_pressure\_profile$ given as:

```
function F = Layer3_pressure_profile(Ps, P0, h, dr, eta, L, P, hfactor)
Q(1) = h(1)^3/(12*eta)*(P(1)-P0)/(L(1));
Q(2) = h(2)^3/(12*eta)*(P(2)-P(1))/(L(2));
```

```
Q(3) = h(3)^3/(12*eta)*(P(3)-P(2))/(L(3));
Q(4) = h(4)^3/(12*eta)*(P(4)-P(3))/(L(4));
Q(5) = h(5)^3/(12*eta)*(P(5)-P(4))/(L(5));
Q(6) = h(6)^3/(12*eta)*(P(6)-P(5))/(L(6));
Q(7) = h(7)^3/(12*eta)*(P(7)-P(6))/(L(7));

Lr = (L(7)+L(8))*hfactor*0.5;

Gs = pi*dr^4/(Lr*128*eta);

Q_inlet(1) = Gs*(Ps-P(1));
Q_inlet(2) = Gs*(Ps-P(3));
Q_inlet(3) = Gs*(Ps-P(5));
Q_inlet(4) = Gs*(Ps-P(7));

F(1) = Q(7)-Q_inlet(4);
F(2) = Q(5)-Q(6)-Q_inlet(3);
F(3) = Q(3)-Q(4)-Q_inlet(2);
F(4) = Q(1)-Q(2)-Q_inlet(1);
F(5) = Q(3)-Q(2);
F(6) = Q(5)-Q(4);
F(7) = Q(7)-Q(6);
end
```

A.6. Joint Stiffness

The joint stiffness is obtained by following the equations of section 2.3.2 from the paper. First, the joint angles are obtained using the same function as described in appendix A.4. Following, the total film height under the left and right side of each slipper is determined regarding the joint angles that correspond to each specific slipper. Then, the dimensions of each linkage and joint are obtained which are later used to obtain the moment acting on each individual joint. Next, the load capacity acting on each slipper is decomposed into the fixed x and y frame. For each joint in each layer the total force in x and y direction is obtained by adding the corresponding forces of the connecting joints one layer below. These forces are then decomposed into the normal and tangential orientation of the joint to obtain the normal and shear force acting on that specific joint. The moment acting on each joint is obtained using equation 39 of the paper and is finally used to obtain the rotational stiffness of each joint. The script to obtain the joint stiffness is given as:

```
close all
clear all
clc

%% Variables
data_size = 100;
Load_Capacity = 100;     %acting on each side of the slipper
ct = 0.2;                %percentage of film height used to rotate the top joint
c1 = 0.1;                %percentage of film height used to rotate the first layer joint
c2 = 0.05;               %percentage of film height used to rotate the second layer joint
c3 = 0.025;              %percentage of film height used to rotate the third layer joint
L = ones(8,1)/32;

%% Initial arrays
LC = ones(16,data_size);
h = ones(data_size,16);
A = 0.1;

%% Angles
% Initial values
theta0 = [0,0,0,0,0,0,0,0,0,0,0,0,0,0,0,0];
J0 = (L(7)+L(8))*1/10;
J = [J0, 2*J0, 4*J0, 8*J0];

% Solver
for i = 1:data_size
    x(i) = i/data_size;
    fun = @(theta0)Layer3_angles_stiffness(x(i), theta0, L, J, A);
    theta(i,:) = fsolve(fun,theta0);
```

```
end

% Data
psi(:,15) = theta(:,15);
psi(:,14) = theta(:,14)-theta(:,15);
psi(:,13) = theta(:,13)-theta(:,15);
psi(:,12) = theta(:,12)-theta(:,14);
psi(:,11) = theta(:,11)-theta(:,14);
psi(:,10) = theta(:,10)-theta(:,13);
psi(:,9) = theta(:,9)-theta(:,13);
psi(:,8) = theta(:,8)-theta(:,12);
psi(:,7) = theta(:,7)-theta(:,12);
psi(:,6) = theta(:,6)-theta(:,11);
psi(:,5) = theta(:,5)-theta(:,11);
psi(:,4) = theta(:,4)-theta(:,10);
psi(:,3) = theta(:,3)-theta(:,10);
psi(:,2) = theta(:,2)-theta(:,9);
psi(:,1) = theta(:,1)-theta(:,9);
psi_rotated = psi'*180/pi;

%% Film Height
for n = 1:data_size
    for p = 1:8
        if psi(n,p) > 0
            h(n,p*2) = h(n,p*2) + c3;
        else
            h(n,p*2-1) = h(n,p*2-1) + c3;
        end
    end

    for q = 1:4
        if psi(n,q+8) > 0
            h(n,q*4-1) = h(n,q*4-1) + c2;
            h(n,q*4) = h(n,q*4) + c2;
        else
            h(n,q*4-3) = h(n,q*4-3) + c2;
            h(n,q*4-2) = h(n,q*4-2) + c2;
        end
    end
%
    for r = 1:2
        if psi(n,r+12) > 0
            h(n,r*8-3) = h(n,r*8-3) + c1;
            h(n,r*8-2) = h(n,r*8-2) + c1;
            h(n,r*8-1) = h(n,r*8-1) + c1;
            h(n,r*8) = h(n,r*8) + c1;
        else
            h(n,r*8-7) = h(n,r*8-7) + c1;
            h(n,r*8-6) = h(n,r*8-6) + c1;
            h(n,r*8-5) = h(n,r*8-5) + c1;
            h(n,r*8-4) = h(n,r*8-4) + c1;
        end
    end
    if psi(n,15) > 0
        h(n,9) = h(n,9) + ct;
        h(n,10) = h(n,10) + ct;
        h(n,11) = h(n,11) + ct;
        h(n,12) = h(n,12) + ct;
        h(n,13) = h(n,13) + ct;
        h(n,14) = h(n,14) + ct;
        h(n,15) = h(n,15) + ct;
        h(n,16) = h(n,16) + ct;
    else
        h(n,1) = h(n,1) + ct;
        h(n,2) = h(n,2) + ct;
        h(n,3) = h(n,3) + ct;
        h(n,4) = h(n,4) + ct;
        h(n,5) = h(n,5) + ct;
        h(n,6) = h(n,6) + ct;
        h(n,7) = h(n,7) + ct;
        h(n,8) = h(n,8) + ct;
```

```
    end
end
h = h';
factor = h.^3;
%% Load Capacity
for i = 1:data_size
    LC(1,i) = Load_Capacity*factor(1,i);
    LC(2,i) = Load_Capacity*factor(2,i);
    LC(3,i) = Load_Capacity*factor(3,i);
    LC(4,i) = Load_Capacity*factor(4,i);
    LC(5,i) = Load_Capacity*factor(5,i);
    LC(6,i) = Load_Capacity*factor(6,i);
    LC(7,i) = Load_Capacity*factor(7,i);
    LC(8,i) = Load_Capacity*factor(8,i);
    LC(9,i) = Load_Capacity*factor(9,i);
    LC(10,i) = Load_Capacity*factor(10,i);
    LC(11,i) = Load_Capacity*factor(11,i);
    LC(12,i) = Load_Capacity*factor(12,i);
    LC(13,i) = Load_Capacity*factor(13,i);
    LC(14,i) = Load_Capacity*factor(14,i);
    LC(15,i) = Load_Capacity*factor(15,i);
    LC(16,i) = Load_Capacity*factor(16,i);
end

%% Distance between joints
J3 = J(1)/2;
J2 = (J(2)+J(1))/2;
J1 = (J(3)+J(2))/2;
Jt = (J(4)+J(3))/2;

L2(1) = (L(2)+L(3))/4;
L2(2) = (L(2)+L(3))/4;
L2(3) = (L(6)+L(7))/4;
L2(4) = (L(6)+L(7))/4;
L2(5) = (L(6)+L(7))/4;
L2(6) = (L(6)+L(7))/4;
L2(7) = (L(2)+L(3))/4;
L2(8) = (L(2)+L(3))/4;

L1(1) = (L(2)+L(3)+L(4)+L(5)+L(6)+L(7)-L2(1)-L2(4))/4;
L1(2) = (L(2)+L(3)+L(4)+L(5)+L(6)+L(7)-L2(1)-L2(4))/4;
L1(3) = (L(2)+L(3)+L(4)+L(5)+L(6)+L(7)-L2(1)-L2(4))/4;
L1(4) = (L(2)+L(3)+L(4)+L(5)+L(6)+L(7)-L2(1)-L2(4))/4;

Lt(1) = (sum(L)-L(1)-L2(1)-L1(1))/2;
Lt(2) = (sum(L)-L(1)-L2(1)-L1(1))/2;

%% Forces and Moments slippers
Fxs(1,:) = -(LC(1,:)+LC(2,:)).*sin(theta(:,1)');
Fxs(2,:) = -(LC(3,:)+LC(4,:)).*sin(theta(:,2)');
Fxs(3,:) = -(LC(5,:)+LC(6,:)).*sin(theta(:,3)');
Fxs(4,:) = -(LC(7,:)+LC(8,:)).*sin(theta(:,4)');
Fxs(5,:) = -(LC(9,:)+LC(10,:)).*sin(theta(:,5)');
Fxs(6,:) = -(LC(11,:)+LC(12,:)).*sin(theta(:,6)');
Fxs(7,:) = -(LC(13,:)+LC(14,:)).*sin(theta(:,7)');
Fxs(8,:) = -(LC(15,:)+LC(16,:)).*sin(theta(:,8)');

Fys(1,:) = (LC(1,:)+LC(2,:)).*cos(theta(:,1)');
Fys(2,:) = (LC(3,:)+LC(4,:)).*cos(theta(:,2)');
Fys(3,:) = (LC(5,:)+LC(6,:)).*cos(theta(:,3)');
Fys(4,:) = (LC(7,:)+LC(8,:)).*cos(theta(:,4)');
Fys(5,:) = (LC(9,:)+LC(10,:)).*cos(theta(:,5)');
Fys(6,:) = (LC(11,:)+LC(12,:)).*cos(theta(:,6)');
Fys(7,:) = (LC(13,:)+LC(14,:)).*cos(theta(:,7)');
Fys(8,:) = (LC(15,:)+LC(16,:)).*cos(theta(:,8)');

Fns(1,:) = LC(1,:)+LC(2,:);
Fns(2,:) = LC(3,:)+LC(4,:);
Fns(3,:) = LC(5,:)+LC(6,:);
Fns(4,:) = LC(7,:)+LC(8,:);
Fns(5,:) = LC(9,:)+LC(10,:);
```

```
Fns(6,:) = LC(11,:)+LC(12,:);
Fns(7,:) = LC(13,:)+LC(14,:);
Fns(8,:) = LC(15,:)+LC(16,:);

Ms(1,:) = (LC(2,:)*L(2)-LC(1,:)*L(1))/2;
Ms(2,:) = (LC(4,:)*L(4)-LC(3,:)*L(3))/2;
Ms(3,:) = (LC(6,:)*L(6)-LC(5,:)*L(5))/2;
Ms(4,:) = (LC(8,:)*L(8)-LC(7,:)*L(7))/2;
Ms(5,:) = (LC(10,:)*L(7)-LC(9,:)*L(8))/2;
Ms(6,:) = (LC(12,:)*L(5)-LC(11,:)*L(6))/2;
Ms(7,:) = (LC(14,:)*L(3)-LC(13,:)*L(4))/2;
Ms(8,:) = (LC(16,:)*L(1)-LC(15,:)*L(2))/2;

ks(1,:) = Ms(1,:)./psi(:,1)';
ks(2,:) = Ms(2,:)./psi(:,2)';
ks(3,:) = Ms(3,:)./psi(:,3)';
ks(4,:) = Ms(4,:)./psi(:,4)';
ks(5,:) = Ms(5,:)./psi(:,5)';
ks(6,:) = Ms(6,:)./psi(:,6)';
ks(7,:) = Ms(7,:)./psi(:,7)';
ks(8,:) = Ms(8,:)./psi(:,8)';

%% Force and Moment Joint Layer 3
Fx3 = Fxs;
Fy3 = Fys;
Fn3 = Fns;
M3 = Ms;

%% Force and Moment Joint Layer 2
Fx2(1,:) = Fx3(1,:)+Fx3(2,:);
Fx2(2,:) = Fx3(3,:)+Fx3(4,:);
Fx2(3,:) = Fx3(5,:)+Fx3(6,:);
Fx2(4,:) = Fx3(7,:)+Fx3(8,:);

Fy2(1,:) = Fy3(1,:)+Fy3(2,:);
Fy2(2,:) = Fy3(3,:)+Fy3(4,:);
Fy2(3,:) = Fy3(5,:)+Fy3(6,:);
Fy2(4,:) = Fy3(7,:)+Fy3(8,:);

Fn2(1,:) = -Fx2(1,:).*sin(theta(:,9)')+Fy2(1,:).*cos(theta(:,9)');
Fn2(2,:) = -Fx2(2,:).*sin(theta(:,10)')+Fy2(2,:).*cos(theta(:,10)');
Fn2(3,:) = -Fx2(3,:).*sin(theta(:,11)')+Fy2(3,:).*cos(theta(:,11)');
Fn2(4,:) = -Fx2(4,:).*sin(theta(:,12)')+Fy2(4,:).*cos(theta(:,12)');

Fs2(1,:) = Fx2(1,:).*cos(theta(:,9)')+Fy2(1,:).*sin(theta(:,9)');
Fs2(2,:) = Fx2(2,:).*cos(theta(:,10)')+Fy2(2,:).*sin(theta(:,10)');
Fs2(3,:) = Fx2(3,:).*cos(theta(:,11)')+Fy2(3,:).*sin(theta(:,11)');
Fs2(4,:) = Fx2(4,:).*cos(theta(:,12)')+Fy2(4,:).*sin(theta(:,12)');

M2(1,:) = (-Fx3(2,:).*sin(theta(:,9)')+Fy3(2,:).*cos(theta(:,9)'))*L2(2) - ...
     (-Fx3(1,:).*sin(theta(:,9)')+Fy3(1,:).*cos(theta(:,9)'))*L2(1) + ...
     (Fx3(2,:).*cos(theta(:,9)')+Fy3(2,:).*sin(theta(:,9)'))*J2 + ...
     (Fx3(1,:).*cos(theta(:,9)')+Fy3(1,:).*sin(theta(:,9)'))*J2 + M3(1,:);% + M3(2,:);
M2(2,:) = (-Fx3(4,:).*sin(theta(:,10)')+Fy3(4,:).*cos(theta(:,10)'))*L2(4) - ...
     (-Fx3(3,:).*sin(theta(:,10)')+Fy3(3,:).*cos(theta(:,10)'))*L2(3) + ...
     (Fx3(4,:).*cos(theta(:,10)')+Fy3(4,:).*sin(theta(:,10)'))*J2 + ...
     (Fx3(3,:).*cos(theta(:,10)')+Fy3(3,:).*sin(theta(:,10)'))*J2;% + M3(3,:) + M3(4,:);
M2(3,:) = (-Fx3(6,:).*sin(theta(:,11)')+Fy3(6,:).*cos(theta(:,11)'))*L2(6) - ...
     (-Fx3(5,:).*sin(theta(:,11)')+Fy3(5,:).*cos(theta(:,11)'))*L2(5) + ...
     (Fx3(6,:).*cos(theta(:,11)')+Fy3(6,:).*sin(theta(:,11)'))*J2 + ...
     (Fx3(5,:).*cos(theta(:,11)')+Fy3(5,:).*sin(theta(:,11)'))*J2;% + M3(5,:) + M3(6,:);
M2(4,:) = (-Fx3(8,:).*sin(theta(:,12)')+Fy3(8,:).*cos(theta(:,12)'))*L2(8) - ...
     (-Fx3(7,:).*sin(theta(:,12)')+Fy3(7,:).*cos(theta(:,12)'))*L2(7) + ...
     (Fx3(8,:).*cos(theta(:,12)')+Fy3(8,:).*sin(theta(:,12)'))*J2 + ...
     (Fx3(7,:).*cos(theta(:,12)')+Fy3(7,:).*sin(theta(:,12)'))*J2;% + M3(7,:) + M3(8,:);

k2(1,:) = M2(1,:)./psi(:,9)';
k2(2,:) = M2(2,:)./psi(:,10)';
k2(3,:) = M2(3,:)./psi(:,11)';
k2(4,:) = M2(4,:)./psi(:,12)';

```

```
%% Force and Moment Joint Layer 1
Fx1(1,:) = Fx2(1,:)+Fx2(2,:);
Fx1(2,:) = Fx2(3,:)+Fx2(4,:);

Fy1(1,:) = Fy2(1,:)+Fy2(2,:);
Fy1(2,:) = Fy2(3,:)+Fy2(4,:);

Fn1(1,:) = -Fx1(1,:).*sin(theta(:,13)')+Fy1(1,:).*cos(theta(:,13)');
Fn1(2,:) = -Fx1(2,:).*sin(theta(:,14)')+Fy1(2,:).*cos(theta(:,14)');

Fs1(1,:) = Fx1(1,:).*cos(theta(:,13)')+Fy1(1,:).*sin(theta(:,13)');
Fs1(2,:) = Fx1(2,:).*cos(theta(:,14)')+Fy1(2,:).*sin(theta(:,14)');

M1(1,:) = (-Fx2(2,:).*sin(theta(:,13)')+Fy2(2,:).*cos(theta(:,13)'))*L1(2) - ...
     (-Fx2(1,:).*sin(theta(:,13)')+Fy2(1,:).*cos(theta(:,13)'))*L1(1) + ...
     (Fx2(2,:).*cos(theta(:,13)')+Fy2(2,:).*sin(theta(:,13)'))*J1 + ...
     (Fx2(1,:).*cos(theta(:,13)')+Fy2(1,:).*sin(theta(:,13)'))*J1;% + M2(1,:) + M2(2,:);
M1(2,:) = (-Fx2(4,:).*sin(theta(:,14)')+Fy2(4,:).*cos(theta(:,14)'))*L1(4) - ...
     (-Fx2(3,:).*sin(theta(:,14)')+Fy2(3,:).*cos(theta(:,14)'))*L1(3) + ...
     (Fx2(4,:).*cos(theta(:,14)')+Fy2(4,:).*sin(theta(:,14)'))*J1 + ...
     (Fx2(3,:).*cos(theta(:,14)')+Fy2(3,:).*sin(theta(:,14)'))*J1;% + M2(3,:) + M2(4,:);

k1(1,:) = M1(1,:)./psi(:,13)';
k1(2,:) = M1(2,:)./psi(:,14)';

%% Force and Moment Top Joint
Fxt(1,:) = Fx1(1,:)+Fx1(2,:);

Fyt(1,:) = Fy1(1,:)+Fy1(2,:);

Fnt(1,:) = Fxt(1,:).*sin(theta(:,15)')+Fyt(1,:).*cos(theta(:,15)');

Fst(1,:) = Fxt(1,:).*cos(theta(:,15)')+Fyt(1,:).*sin(theta(:,15)');

Mt(1,:) = (-Fx1(2,:).*sin(theta(:,15)')+Fy1(2,:).*cos(theta(:,15)'))*Lt(2) - ...
     (-Fx1(1,:).*sin(theta(:,15)')+Fy1(1,:).*cos(theta(:,15)'))*Lt(1) + ...
     (Fx1(2,:).*cos(theta(:,15)')+Fy1(2,:).*sin(theta(:,15)'))*Jt + ...
     (Fx1(1,:).*cos(theta(:,15)')+Fy1(1,:).*sin(theta(:,15)'))*Jt;% +  + M1(1,:) + ...
     M1(2,:);

kt(1,:) = Mt(1,:)./psi(:,15)';

%% Results
min_kt = min(min(kt))
min_k1 = min(min(k1))
min_k2 = min(min(k2))
min_k3 = min(min(ks))

max_Fn = [max(max(Fnt)) max(max(Fn1)) max(max(Fn2)) max(max(Fn3))]
max_Fs = [max(max(abs(Fst))) max(max(abs(Fs1))) max(max(abs(Fs2))) 0]
```

Where the function $Layer3\_angles\_stiffness$ is given as:

```
function F = Layer3_angles_stiffness(x_start,theta, L, J, A)
% Slipper Lengths (L) and Joint Heights (J)
L1A = L(1)/2;
L1B = L(1)/2;
L2A = L(2)/2;
L2B = L(2)/2;
L3A = L(3)/2;
L3B = L(3)/2;
L4A = L(4)/2;
L4B = L(4)/2;
L5A = L(5)/2;
L5B = L(5)/2;
L6A = L(6)/2;
L6B = L(6)/2;
L7A = L(7)/2;
L7B = L(7)/2;
L8A = L(8)/2;
```

```
L8B = L(8)/2;

J1 = J(1)/2;
J2 = J(2)/2;
J3 = J(3)/2;
J4 = J(4)/2;

% Linkage lengths (d)
d11 = L1B + L2A;
d12 = L3B + L4A;
d13 = L5B + L6A;
d14 = L7B + L8A;
d21 = L2B+L3A+(d11+d12)/2;
d22 = L2B+L3A+(d11+d12)/2;
d3 = (L4B+d12/2+d21/2)*2;


%% Geometry
x31 = x_start;

x21 = x31-1/2*d3*cos(theta(15))+(J3+J4)*sin(theta(15));
x22 = x31+1/2*d3*cos(theta(15))+(J3+J4)*sin(theta(15));

x11 = x21-1/2*d21*cos(theta(13))+(J2+J3)*sin(theta(13));
x12 = x21+1/2*d21*cos(theta(13))+(J2+J3)*sin(theta(13));
x13 = x22-1/2*d22*cos(theta(14))+(J2+J3)*sin(theta(14));
x14 = x22+1/2*d22*cos(theta(14))+(J2+J3)*sin(theta(14));

x1 = x11-1/2*d11*cos(theta(9))+(J2+J1)*sin(theta(9));
x2 = x11+1/2*d11*cos(theta(9))+(J2+J1)*sin(theta(9));
x3 = x12-1/2*d12*cos(theta(10))+(J2+J1)*sin(theta(10));
x4 = x12+1/2*d12*cos(theta(10))+(J2+J1)*sin(theta(10));
x5 = x13-1/2*d13*cos(theta(11))+(J2+J1)*sin(theta(11));
x6 = x13+1/2*d13*cos(theta(11))+(J2+J1)*sin(theta(11));
x7 = x14-1/2*d14*cos(theta(12))+(J2+J1)*sin(theta(12));
x8 = x14+1/2*d14*cos(theta(12))+(J2+J1)*sin(theta(12));

xp1 = x1+J1*sin(theta(1));
xp2 = x2+J1*sin(theta(2));
xp3 = x3+J1*sin(theta(3));
xp4 = x4+J1*sin(theta(4));
xp5 = x5+J1*sin(theta(5));
xp6 = x6+J1*sin(theta(6));
xp7 = x7+J1*sin(theta(7));
xp8 = x8+J1*sin(theta(8));

y31 = theta(16);

y21 = y31-1/2*d3*sin(theta(15))-(J3+J4)*cos(theta(15));
y22 = y31+1/2*d3*sin(theta(15))-(J3+J4)*cos(theta(15));

y11 = y21-1/2*d21*sin(theta(13))-(J2+J3)*cos(theta(13));
y12 = y21+1/2*d21*sin(theta(13))-(J2+J3)*cos(theta(13));
y13 = y22-1/2*d22*sin(theta(14))-(J2+J3)*cos(theta(14));
y14 = y22+1/2*d22*sin(theta(14))-(J2+J3)*cos(theta(14));

y1 = y11-1/2*d11*sin(theta(9))-(J2+J1)*cos(theta(9));
y2 = y11+1/2*d11*sin(theta(9))-(J2+J1)*cos(theta(9));
y3 = y12-1/2*d12*sin(theta(10))-(J2+J1)*cos(theta(10));
y4 = y12+1/2*d12*sin(theta(10))-(J2+J1)*cos(theta(10));
y5 = y13-1/2*d13*sin(theta(11))-(J2+J1)*cos(theta(11));
y6 = y13+1/2*d13*sin(theta(11))-(J2+J1)*cos(theta(11));
y7 = y14-1/2*d14*sin(theta(12))-(J2+J1)*cos(theta(12));
y8 = y14+1/2*d14*sin(theta(12))-(J2+J1)*cos(theta(12));

yp1 = y1-J1*cos(theta(1));
yp2 = y2-J1*cos(theta(2));
yp3 = y3-J1*cos(theta(3));
yp4 = y4-J1*cos(theta(4));
yp5 = y5-J1*cos(theta(5));
yp6 = y6-J1*cos(theta(6));
```

```
yp7 = y7-J1*cos(theta(7));
yp8 = y8-J1*cos(theta(8));

%% Functions
F(1) = A*sin(2*pi*xp1)-yp1;
F(2) = atan(A*2*pi*cos(2*pi*xp1))-theta(1);
F(3) = A*sin(2*pi*xp2)-yp2;
F(4) = atan(A*2*pi*cos(2*pi*xp2))-theta(2);
F(5) = A*sin(2*pi*xp3)-yp3;
F(6) = atan(A*2*pi*cos(2*pi*xp3))-theta(3);
F(7) = A*sin(2*pi*xp4)-yp4;
F(8) = atan(A*2*pi*cos(2*pi*xp4))-theta(4);
F(9) = A*sin(2*pi*xp5)-yp5;
F(10) = atan(A*2*pi*cos(2*pi*xp5))-theta(5);
F(11) = A*sin(2*pi*xp6)-yp6;
F(12) = atan(A*2*pi*cos(2*pi*xp6))-theta(6);
F(13) = A*sin(2*pi*xp7)-yp7;
F(14) = atan(A*2*pi*cos(2*pi*xp7))-theta(7);
F(15) = A*sin(2*pi*xp8)-yp8;
F(16) = atan(A*2*pi*cos(2*pi*xp8))-theta(8);
end
```

A.7. Top Joint Peak to Peak Ratio

The ratio between the top joint vertical peak to peak value and the counter surface peak to peak value is obtained by finding the minimum and maximum values of the top joint y position and the amplitude of the track. Following, the script is displayed to obtain these values where the functions $Layer1\_angles$, $Layer2\_angles$ and $Layer3\_angles$ are given in appendix A.4.

```
clear all
close all
clc

options=optimset('MaxFunEvals',10000, 'MaxIter', 10000);
%% Variables
data_size = 100;
wavelength_factor = 3/4; %bearing length as function of wavelength
Wavelength = 1;
A = 0.1*Wavelength;
max_bearing_length = 1; %maximum bearing length as a percentage of the wavelength
data_size_bearing_length = 100;

%% Starting matrices
max_range_y1 = zeros(data_size_bearing_length,1);
max_range_y2 = zeros(data_size_bearing_length,1);
max_range_y3 = zeros(data_size_bearing_length,1);
bearing_length = zeros(data_size_bearing_length,1);

%% 1 Layer
for j = 1:data_size_bearing_length
    wavelength_factor = max_bearing_length*j/(data_size_bearing_length);
    theta10 = [0,0,0,0];
    L10 = [1,1]*wavelength_factor*Wavelength/(4);
    J01 = (L10(1)+L10(2))*1/5;
    J10 = [J01, 2*J01];

    % Solver
    for i = 1:data_size
        x(i) = i/data_size;
            fun = @(theta10)Layer1_angles(x(i), theta10, L10, J10, A);
        psi1(i,:) = fsolve(fun,theta10,options);
    end

    max_range_y1(j) = max(psi1(:,4))-min(psi1(:,4));
    bearing_length(j) = wavelength_factor;
end

```

```
%% 2 Layers
for j = 1:data_size_bearing_length
    wavelength_factor = max_bearing_length*j/(data_size_bearing_length);
    theta20 = [0,0,0,0,0,0,0,0];
    L20 = [1,1,1,1]*wavelength_factor/(8);
    J02 = (L20(3)+L20(4))*1/5;
    J20 = [J02, 2*J02, 4*J02];

    % Solver
    for i = 1:data_size
        x(i) = i/data_size;
        fun = @(theta20)Layer2_angles(x(i), theta20, L20, J20, A);
        psi2(i,:) = fsolve(fun,theta20,options);
    end

    max_range_y2(j) = max(psi2(:,8))-min(psi2(:,8));
end

%% 3 Layers
for j = 1:data_size_bearing_length
    wavelength_factor = max_bearing_length*j/(data_size_bearing_length);
    theta30 = [0,0,0,0,0,0,0,0,0,0,0,0,0,0,0,0];
    L30 = [1,1,1,1,1,1,1,1]*wavelength_factor/(16);
    J03 = (L30(7)+L30(8))*1/5;
    J30 = [J03, 2*J03, 4*J03, 8*J03];

    % Solver
    for i = 1:data_size
        x(i) = i/data_size;
        fun = @(theta30)Layer3_angles(x(i), theta30, L30, J30, A);
        psi3(i,:) = fsolve(fun,theta30);
    end

    max_range_y3(j) = max(psi3(:,16))-min(psi3(:,16));
end

%% Amplitude Ratio
ratio_1_layer = max_range_y1/(2*A);
ratio_2_layer = max_range_y2/(2*A);
ratio_3_layer = max_range_y3/(2*A);

%% Plots
figure (1)
hold on
grid on
top1 = plot(bearing_length*100,ratio_1_layer, 'b--');
top2 = plot(bearing_length*100,ratio_2_layer, 'r-.');
top3 = plot(bearing_length*100,ratio_3_layer, 'k-');

legend([top1 top2 top3], 'Single Layer', 'Double Layer', 'Tripple Layer', 'Location', ...
    'northeast')
title(['Vertical Translation Ratio of Top Joint'])
xlabel('Bearing lenght as % of the wavelength')
ylabel('Peak to peak ratio')
axis([0,100,0,1])
```

B

Bearing Pad Geometry

The geometry of the slipper has an effect on the load capacity of the bearing, and the ability to deform into a concave convex or saddle point orientation. For hydrostatic bearings, the optimum shape for the highest load capacity is a circle due to its large surface to perimeter value. However, when connecting the slippers, a circular shape would provide problems. Therefore, a shape that could easily be connected to each other while still having a large surface to perimeter value is needed. Furthermore, a shape that can be repeated to fill a surface would ease the design process. Therefore, a look into tiling is made. Tiling is a method to fill a flat surface with repeating smaller shapes. Some of the basic tiling shapes are a triangle, square or hexagonal shown in figure B.1.

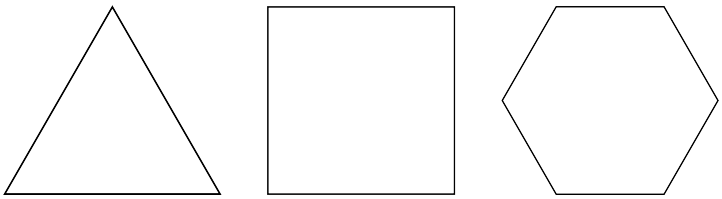

Figure B.1: Common tiling shapes.

A search in literature is made to determine if these shapes could fill a spherical surface instead of a flat surface. One of the results is the design of a large reflector with flat facets [31]. This design was made to provide a spherical reflector for a satellite that consisted out of flat facets. It shows that each of the 3 basic geometries could form a spherical shape with a certain RMS error with respect to the real sphere. This means that each of the shapes geometries could be chosen to follow the provided surface. Now that it is shown that each shape could be used to fill a sphere, a look into the highest area vs perimeter value is made. Table B.1 shows for each shape the area, perimeter and area to perimeter value. Since a comparison is done, each shape is made to have the same area of 1 m^2. It can be seen that a hexagon has the highest area to perimeter value and is therefore the best option to choose as slipper geometry.

	Triangle	Square	Hexagon	Circle
Area [m^2]	1.00	1.00	1.00	1.00
Perimeter [m]	4.56	4.00	3.72	3.55
Area/Perimeter [m]	0.22	0.25	0.27	0.28

Table B.1: Area to perimeter value of a triangle, square, hexagon and circle

To design the elasto-hydrostatic bearing, a total of 9 hexagonal pads is needed to obtain each Gaussian curvature. When combining 3 hexagonal pads, a concave and configuration can be obtained which provides a positive Gaussian curvature. When connecting a convex and concave configuration to each other, a negative Gaussian curvature is formed. Finally due to the attachment of 9 hexagonal pads to each other, a Gaussian curvature of 0 can be obtained. This means that all Gaussian curvatures are covered when connecting 9 hexagonal pads.

C

Rapid Demonstrator

A rapid demonstrator is made to give an insight if a 3D hydrostatic bearing consisting of 9 hexagonal pads can indeed deform in the used configuration, as shown in figure C.1. The demonstrator is completely 3D printed using ball bearings as joints. The stiff hexagonal pads are enclosed by a silicon layer connecting all the pads together creating one large pad. The top of a spherical structure is printed on which the bearing is pressed to show the deforming behavior of the bearing. Figure C.2 gives an example of the demonstrator pressed on the spherical surface showing small deformations of the bearing. This shows that the system can deform into a concave configuration. Figure C.3 shows the bearing pressed on the side of the spherical surface creating a saddle point. It is shown that the bearing follows the counter surface meaning that the system can indeed deform over saddle points. To check if the bearing can deform in a convex configuration, the bearing is pushed into a bowl, as shown in figure C.4. It is shown that the bearing deforms towards the convex configuration validating that the system can form into convex configurations.

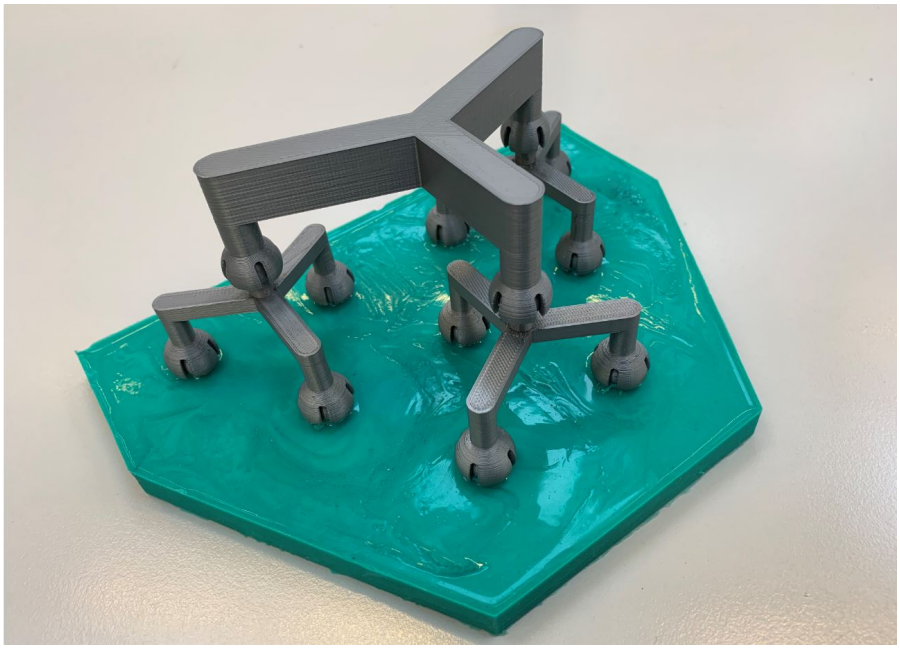

Figure C.1: Rapid demonstrator consisting of 9 hexagonal pads enclosed by a silicon layer and connected by linkages using ball joints.

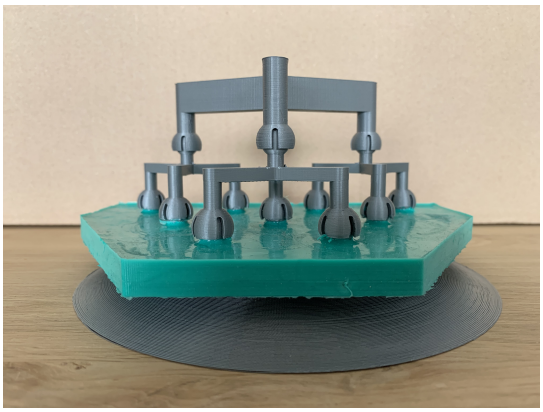

(a) Rapid demonstrator with no load applied on a concave surface.

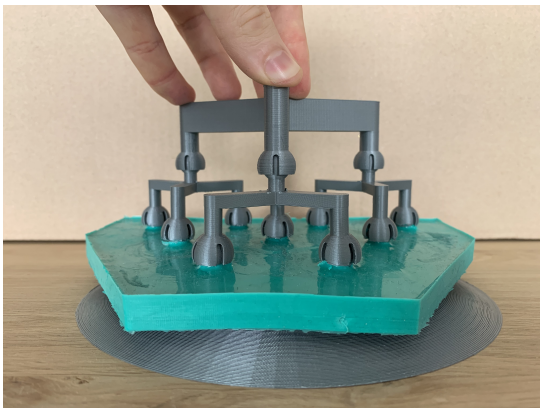

(b) Rapid demonstrator with load applied on a concave surface.

Figure C.2: Rapid demonstrator on a concave surface.

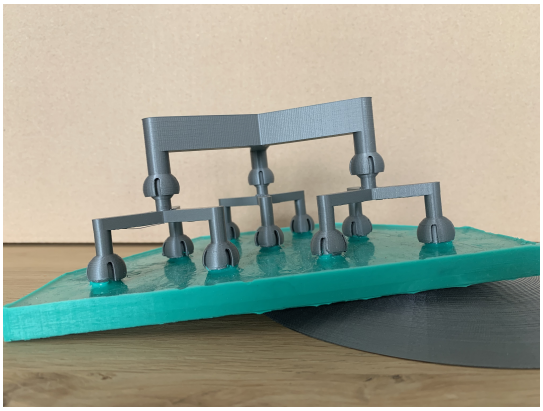

(a) Rapid demonstrator with no load applied on a saddle point surface.

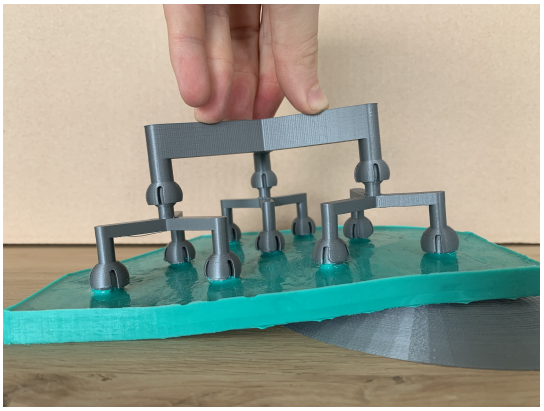

(b) Rapid demonstrator with load applied on a saddle point surface.

Figure C.3: Rapid demonstrator on a saddle point surface.

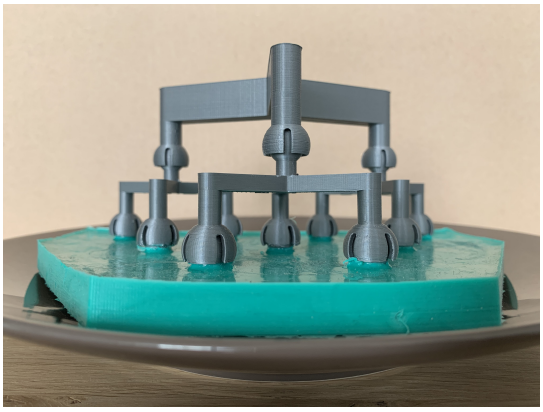

(a) Rapid demonstrator with no load applied on a convex surface.

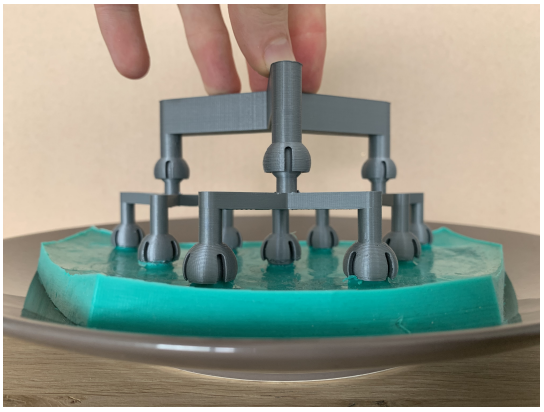

(b) Rapid demonstrator with load applied on a convex surface.

Figure C.4: Rapid demonstrator on a convex surface.

Bibliography

[1] R. F. P. Gomez, J. P. A. Nijssen, and R. A. J. van Ostayen. Design of a Compliant Hinge based on Closed Form Pressure Balancing. pages 1–12, 2010.

[2] Paul Cooper. Nemi ships: How caligula's floating pleasure palaces were found and lost again, May 2019.

[3] Jonathan Ridley Head of Engineering Warsash School of Maritime Science and Engineering. Leonardo da vinci's helicopter: 15th-century flight of fancy led to modern aeronautics, May 2019.

[4] I. A. Lyashenko. Tribological properties of dry, fluid, and boundary friction. *Technical Physics*, 56(5):701–707, 2011.

[5] J. P. A. Nijssen, A. Kempenaar, and N. Diepeveen. Development of an interface between a plunger and an eccentric running track for a low-speed seawater pump. (January 2019), 2018.

[6] R. A. J. van Ostayen. *The Hydro–Support: An Elasto–Hydrostatic Thrust Bearing with Mixed Lubrication*. 2014.

[7] A. Belyi, G. Osadchy, D. Efanov, and D. Shestovitskiy. Implementation of the Continuous Monitoring System for Technical Condition of the St. Petersburg Arena Stadium Sliding Roof. *Proceedings of 2018 IEEE East-West Design and Test Symposium, EWDTS 2018*, 2018.

[8] Ron A J van Ostayen, Anton van Beek, and Mink Ros. A mathematical model of the hydro-support: An elasto-hydrostatic thrust bearing with mixed lubrication. *Tribology International*, 37(8):607–616, 2004.

[9] A. van Beek and L. Lepic. Rubber supported hydrostatic thrust bearings with elastic bearing surfaces of infinite length. 201:45–50, 1996.

[10] A. van Beek and A. Segal. Rubber supported hydrostatic thrust bearings with rigid bearing surfaces. *Tribology International*, 30(1):47–52, 1997.

[11] J. P. A. Nijssen and R. A. J. van Ostayen. Compliant Hydrostatic Bearing utilizing Functionally Graded Materials. (1), 2020.

[12] V. A. Yastrebov, G. Anciaux, and J. F. Molinari. The contact of elastic regular wavy surfaces revisited. *Tribology Letters*, 56(1):171–183, 2014.

[13] Y. F. Gao, A. F. Bower, K. S. Kim, L. Lev, and Y. T. Cheng. The behavior of an elastic-perfectly plastic sinusoidal surface under contact loading. *Wear*, 261(2):145–154, 2006.

[14] J. Dundurs, K. C. Tsai, and L. M. Keer. Contact between elastic bodies with wavy surfaces. *Journal of Elasticity*, 3(2):109–115, 1973.

[15] Y. Jia. Gaussian and Mean Curvatures. 2(1):1–7, 2018.

[16] G.W. Stachowiak and A.W. Batchelor. *Engineering Tribology*. 1993.

[17] Donald B. Bickler. Articulated Suspension System. (19), 1989.

[18] David P. Miller and Tze Liang Lee. High-speed traversal of rough terrain using a Rocker-Bogie mobility system. *Space 2002 and Robotics 2002*, pages 428–434, 2002.

[19] Brian D. Harrington and Chris Voorhees. The Challenges of Designing the Rocker-Bogie Suspension for the Mars Exploration Rover. *Biblioteca Ayacucho*, (68):cii, 599 p., 1980.

[20] Dongmok Kim, Heeseung Hong, Hwa Soo Kim, and Jongwon Kim. Optimal design and kinetic analysis of a stair-climbing mobile robot with rocker-bogie mechanism. *Mechanism and Machine Theory*, 50:90–108, 2012.

[21] Nitin Yadav, Balram Bhardwaj, and Suresh Bhardwaj. Design analysis of Rocker Bogie Suspension System and Access the possibility to implement in Front Loading Vehicles. *IOSR Journal of Mechanical and Civil Engineering Ver. III*, 12(3):2278–1684, 2015.

[22] M. Schenk, S. D. Guest, and J. L. Herder. Zero stiffness tensegrity structures. *International Journal of Solids and Structures*, 44(20):6569–6583, 2007.

[23] T. Tarnai. Zero stiffness elastic structures. *International Journal of Mechanical Sciences*, 45(3):425–431, 2003.

[24] Hui Cheng, Yiu Kuen Yiu, and Zexiang Li. Dynamics and Control of Redundantly Actuated Parallel Manipulators. *IEEE/ASME Transactions on Mechatronics*, 8(4):483–491, 2003.

[25] Xin Jun Liu, Jinsong Wang, Chao Wu, and Jongwon Kim. A new family of spatial 3-DOF parallel manipulators with two translational and one rotational DOFs. *Robotica*, 27(2):241–247, 2009.

[26] Bum Seok Kim and Hong Hee Yoo. Body guidance syntheses of four-bar linkage systems employing a spring-connected block model. *Mechanism and Machine Theory*, 85:147–160, 2015.

[27] S. C. Yeniceli. Design Optimization of Whiffletree Systems for Wind Turbine. (January):123, 2014.

[28] C. Baffes, T. Mast, J. Nelson, E. Ponslet, V. Stephens, L. Stepp, and E. C. Williams. Primary mirror segmentation studies for the Thirty Meter Telescope. *Advanced Optical and Mechanical Technologies in Telescopes and Instrumentation*, 7018(70180):70180S, 2008.

[29] P. Dierickx. The European extremely large telescope (E-ELT). *Highlights of Spanish Astrophysics IV - Proceedings of the 7th Scientific Meeting of the Spanish Astronomical Society, SEA 2006*, (March):15–28, 2007.

[30] J. Nijenhuis, R. Hamelinck, B. Braam, and M. Cayrel. Meeting highest performance requirements for lowest price and mass for the M1 segment support unit for E-ELT. *Ground-based and Airborne Telescopes III*, 7733(August 2010):77332H, 2010.

[31] P.K. Agrawal, M.S. Anderson, and M.F. Card. Preliminary Design of Large Reflectors with Flat Facets. (July):1–33, 2000.